UNIVERSITY OF MANITOBA

Development of a Low Voltage and Large Stroke MEMS-based Lorentz Force Continuous Deformable Polymer Mirror System

by

Byoungyoul Park

A Thesis submitted to the Faculty of Graduate Studies of

The University of Manitoba

in partial fulfillment of the requirements of the degree of

DOCTOR OF PHILOSOPHY

Department of Electrical and Computer Engineering
University of Manitoba
Winnipeg, MB

Development of a Low Voltage and Large Stroke MEMS-based Lorentz Force Continuous Deformable Polymer Mirror System

Byoungyoul Park

2018

Abstract

The image resolution of modern optical systems is restricted by wavefront aberrations due to turbulence and diffraction in optical media and instruments. Adaptive optics (AO) is a technology that improves image resolution by compensating distorted wavefronts by using deformable mirror system (DMs). In this research, the design and fabrication of miniaturized Lorentz DM for AO applications is studied. The Lorentz actuator arrays and the continuous polymer deformable mirror are manufactured using bulk micromachining techniques developed for the fabrication of Microelectromechanical Systems (MEMS).

In many AO applications, a massive array of actuators (100s – 5000s) and flexible mirrors are required to control the topology of the mirror surface. Sometimes, DMs with a large vertical stroke (over 5 μm) are required depending on the application. The stroke of conventional and MEMS electrostatic, piezoelectric, and electrostrictive actuated DMs is limited. This is because the stroke is proportional to the actuation voltage that can rise to dangerously high level (over 100V), which can cause problems with integrating the DM with on-chip driving circuits. The high voltage DM requires multiple wire connections to external high voltage amplifiers. This, in turn, results in significant space occupancy, high power consumption, and increased complexity of the system. Therefore, the development of a flexible continuous mirror and actuator array with high stroke and low driving voltage is highly desirable. In this study, a flexible polymer-based continuous deformable mirror is developed. The mirror uses the epoxy-based SU-8 as a structural material. The actuator arrays that drive the mirror are constructed as flexible serpentine springs on either side of a central thick and rigid crossbar above permanent magnets.

There were several challenges in the development of the new Lorentz force actuated DMs. One of the significant challenges in designing the DMs was to determine the correlation between the spring constant of the mirror and actuator, and the inter-actuator coupling of the DM. The inter-actuator coupling represents the range of allowable tolerances for mirror deformation to correction of wavefront aberrations

which may vary depending on the applications. In this research, we were able to predict the correlation between the spring constant of the mirror and actuator, and the inter-actuator coupling of the DMs simultaneously using COMSOL Multiphysics software. As a result of this work, we have developed a technique for varying the inter-actuator coupling of the DMs by changing the dimensions of the actuator. One problem encountered during the course of the research was the random local deformation of the DM after releasing the mirror. This problem was caused by localized stress and strain. The double side coating technique allowed us to build a sufficiently flat continuous mirror membrane. Lastly, KOH bulk micromachining, which was necessary for fabrication the actuator, provided a rugged etch profile. We were able to etch the substrate uniformly by the regular rotation of the substrate during the KOH etch.

Using the technologies developed in this research, we demonstrate a 12 mm × 12 mm Al/SU-8/Al mirror with a 5 × 5 serpentine spring Lorentz actuator array. The mirror substrate was bonded with an actuator substrate, tested, and observed a significant ± 17 μm deformation at ± 3 mA actuation current, requiring an operational voltage of less than 1 V. This Lorentz DM would operate at a frequency over 1 kHz with a 40 μm large stroke at operation current of 9 mA. Such parameters can be suitable for large deformation adaptive optics applications. Furthermore, the Lorentz DM can potentially be applicable in correcting high order wavefront distortion once the development of a suitable bonding technique is realized.

Acknowledgments

First, I would like to thank Dr. Cyrus Shafai for accepting me at the Nano Systems Fabrication Laboratory (NSFL) and guiding me through the exciting and relevant topic that constitutes this thesis. I appreciate for sharing not only for vast amounts of knowledge and wisdom during our meeting and conversations but also for his intelligent approaches to problem-solving. I feel fortunate that I have the privilege of becoming his student. Thank you.

I appreciate particularly to Dwayne Chrusch who taught me a lot of hands-on skills and knowledge of the cleanroom and vacuum equipment throughout these five years. He also delighted to discuss with me regarding device design and fabrication process. I would like to thank you Cory Smit and Daryl Hamelin and everyone in the tech-shop in E3-550 for teaching me many practical skills in the engineering trades. I am also grateful to Dr. Arkady Major and Dr. Jason Fiege for sharing some valuable optical and physical engineering knowledge with me. I thank graduate advisor Amy Dario for her support and friendship. Special thanks to Dr. David Andersen and Dr. Gregory Burley for supporting this project and various technical advice. Without their support, I would not have been able to carry out this research project.

My Ph.D. life was mostly fun and exciting, but sometimes it was tedious, confusing or even frustrating. I was able to enjoy this process happily since I have had many good friends and their help in the Department of ECE. I am particularly grateful to all my colleagues at NSFL including Ehsan Tahmasebian, Elnaz Afsharipour, Janaranjana Sampath Hiniduma Liyanage, Meiting Li, Mojtaba Safari, Pawel Glowacki, Tao Chen, Ramin Soltanzadeh, Yu Zhou, and many more. Their friendship and much precious advice have always encouraged me during the Ph.D. program. I markedly thank Tao, Mojtaba, Elnaz, Ramin, Pawel, and Sampath for providing me with a significant amount of technical help and sharing their experiences. I would also like to thank for the friendship and support during my Ph.D.

program from Ankit Gupta, Sharmistha Bhadra, Anton Vykhodtsev, Md. Obaej Tareq and more during my Ph.D. program.

I would appreciate the AKCSE Manitoba members who have supported me to acquire a local engineering culture and shared their experience. In particular, the advice and help from Dr. Cheolho Jung, Dr. Jungsoo Park, Prof. Miyoung Seo and Prof. Wooil Moon gave me great strength. They have also inspired me with good examples of how to contribute to the Korean-Canadian science and engineering society. It will be a good indicator of my future life as an engineer.

I would also like to thank my former advisor Kyoungwan Park, faculty member WanSik Hong, JungHyun Sok, and ex-colleague EunKyum Kim and others in the Department of Nanoscience and Technology at the University of Seoul. Even after finish the master program long ago, their continued support has been an excellent foundation to progress through my doctoral program successfully.

I am grateful to my friends and colleagues in many companies and government research institute who helped and supported me to get started my doctoral program. They trained me and gave me much experience in research and teamwork. This experience has truly benefited me in many ways. Thank you Bumsoo Lee and Taemin Kim from E&D Solution Inc., Gunho Kim, Sangwon Lee, Namchul Park from LG Innotek, Banghyun Kim and Jaeho Cho from Seoulsemiconductor Ltd., and Kyoungho Kim, Ilhyung Lee, Hoshin Lee, Juwhan Seo from KISTI.

I would like to thank all my friends in Canada who helped me for being settled in a new city and country. I enjoyed every single day of my stay in Winnipeg among them, and their company was warm enough that I barely notice the cold winters of Winnipeg.

Lastly, I would also like to express my most profound appreciation to my loving family. No matter how far we were, I always felt their endless support and care, and they were always close to my heart. I am so glad to have the most amazing and supportive mother, Youngsoon Lee, in the world. I have truly the most wonderful sisters; their manner always lets me feel proud of my family and was the best courage for me. My sincere gratitude goes to my beloved wife, Eunna Oh, for being always understanding

and caring during my studies. I appreciate her patience for five years and always being amazingly supportive and loving during my studies. I also appreciate and love my sons, Siyoung and Siwon.

January 9, 2017

This thesis is dedicated to my wife, Eunna Oh, who has been a constant source of support and encouragement during the challenges of graduate school and life. I am truly thankful for having you in my life. This work is also dedicated to my dear Grandparents, parents Juil Park and Youngsoon Lee, beautiful sisters, my sweet sons Siyoung and Siwon, and all relatives.

Contents

List of Tables

List of Figures

Notations and Abbreviations

The following notations and abbreviations are used in the thesis:

List	Description
AC	Alternating Current
Al	Aluminum
AO	Adaptive Optics
Ar	Argon
BOE	Buffered Oxide Etchant
CMP	Chemical Mechanical Polishing
Cr	Chromium
c-Si	Crystalline Silicon
CTE	Coefficient of Thermal Expansion
Cu	Copper
EDP	An aqueous solution of ethylene diamine and pyrocatechol
DC	Direct Current
DI Water	De-Ionized Water
DM	Deformable Mirror
DRIE	Deep reactive-ion etching (a highly anisotropic etch process)
DSP	Double-side Polished
f	Frequency (Unit: *Hz*)
F	Force (Unit: N)
FWHM	Full Width at Half Maximum
HMDS	Hexamethyldisilazane
HF	Hydrofluoric acid
i	Current (Unit: A)
ICP	Inductively Coupled Plasma

List	Description
j	Current Density (Unit: A/cm^3)
KOH	Potassium Hydroxide
l	Length
MEMS	Micro-Electro-Mechanical System
N_2	Nitrogen
NSFL	Nano System Fabrication Laboratory
p	Pressure (Unit: Torr)
Poisson's Ratio (ν)	The ratio of lateral strain and axial strain. ν = lateral strain / axial strain (Unitless)
PMN	lead magnesium niobate
PR	Photoresist
RIE	Reactive Ion Etching
Si	Silicon
SiO_2	Silicon Dioxide
Sn	Tin
S_R	Strehl ratio (S_R)
t	Thickness (Unit: μm)
T	Temperature (Unit: K)
Thermal Conductivity	The amount of heat per unit time per unit area that can be conducted through a plate of unit thickness of a given material. (unit = W/m·K)
Ti	Titanium
TMAH	Tetramethylammonium hydroxide
w	Width
XeF_2	Xenon Difluoride
Yield Strength	Maximum stress that can be developed in a material without causing plastic deformation (unit = Pa)
Young's modulus (E)	The ratio of stress and strain in the linear range of the stress and strain curve of the material. E = stress / strain (unit = Pa)

1

Background

Contents

1.1 Adaptive Optics

The resolution of optical observation systems is restricted by aberrations of optical beams in the propagation medium. Aberrations caused by atmospheric turbulence, optical fabrication errors, and thermally induced distortion, reduce the peak intensity and smear the image. Generally, with a larger aperture size, the image sharpens, and the diffraction angle is decreased. However, the image quality is more dependent on the propagation medium than the aperture size for many optical systems. Adaptive Optics (AO) can compensate this distorted image in real time.

The first conceptual AO system was introduced by H. W. Babcock in 1953 [1]. The principle of the AO system has not changed despite different hardware used today. The deformation shape of the

adaptive mirror (Eidophor in the paper) is controlled by a wavefront sensor (knife-edge device in the paper). Edipohor consists of a thin layer of oil covered by a reflective mirror. The electrostatic force between an electrically charged layer on the oil surface and the bottom electrode changes the shape of the mirror surface. Since then, the first operational AO system was installed on a surveillance telescope at Haleakala Observatory in Maui, Hawaii in the 1980's, where it imaged satellites launched by the Soviet Union [2].

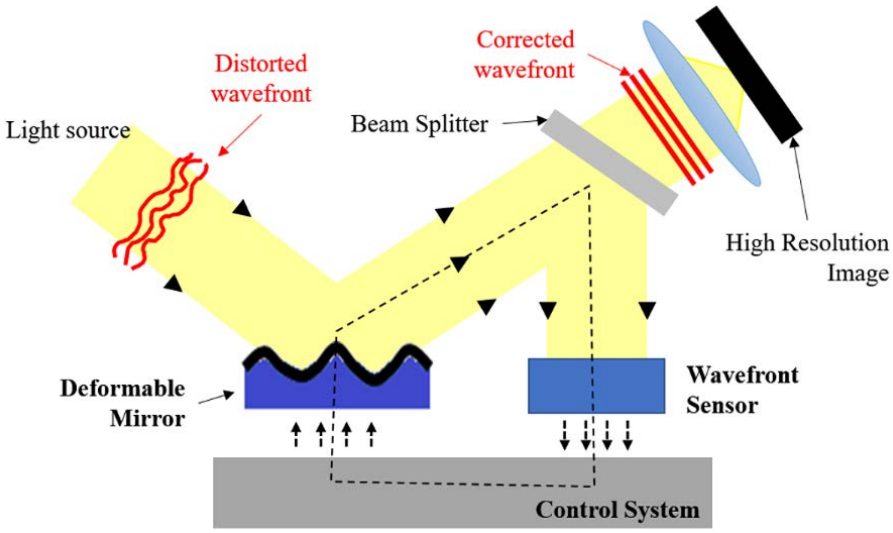

Figure 1.1: Basic Component of Adaptive Optic System

Figure 1.1 shows a typical adaptive optic system in an Earth-based telescope that consists of three main parts including a deformable mirror (DM), a wavefront sensor, and a control system. Perturbed wavefronts from atmospheric turbulence fall incident on the wavefront sensor. The wavefront sensor measures the amount of distortion by measuring the electromagnetic radiation from an artificial laser guide star placed high above the telescope. A control system interprets the measurement results from the wavefront sensor and transfers a signal to a DM system to drive the actuators. Once the wavefront sensor and control system determines the distortion value and translates it into a control signal, the mirror deforms by moving an actuator corresponding to the amount of wavefront distortion. Through this

process, adaptive optics can enhance image quality in optical and infrared astronomical telescopes and track rapidly moving objects in space.

The purpose of the wavefront sensor is to acquire the maximum wavefront distortion information from a minimal number of photons. For that reason, charge-coupled devices (CCDs) with quantum efficiencies of 80 to 90 % are widely used as distortion detectors. The Shark-Hartmann wavefront sensor consists of many small lenses, and is commonly used as position detector for high order wavefront distortion. Other types of the wavefront sensors, such as shearing interferometer and curvatures sensors can be useful for low order aberrations.

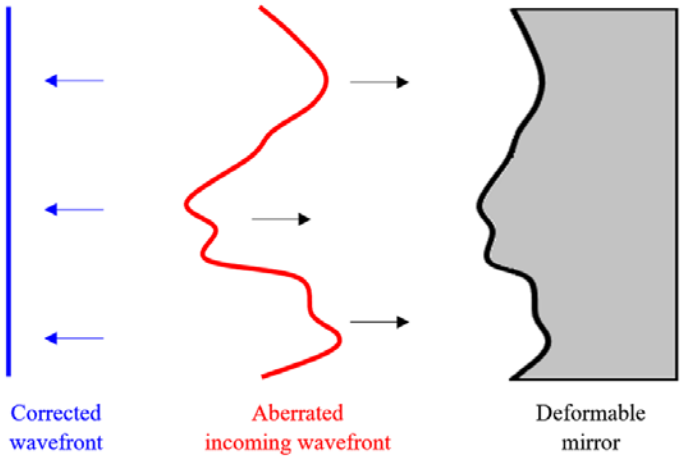

Figure 1.2: Schematic illustration of wavefront compensation using a deformable mirror.

The concept of wavefront correction by DM is shown in Figure 1.2. The DM needs to be deformed by half of the distortion in the incoming wavefront. The control system shown in Figure 1.1 controls the mirror deformation according to the real-time aberration measurements from a wavefront sensor.

AO systems can compensate for image wavefront aberrations and are being explored for various applications, such as Earth-based telescopes [3-8], microscopy [9-11], retinal imaging [2,12-15], optical communication [16], and high energy lasers [17]. Figure 1.3 shows some examples with enhanced image resolution after applying AO technology.

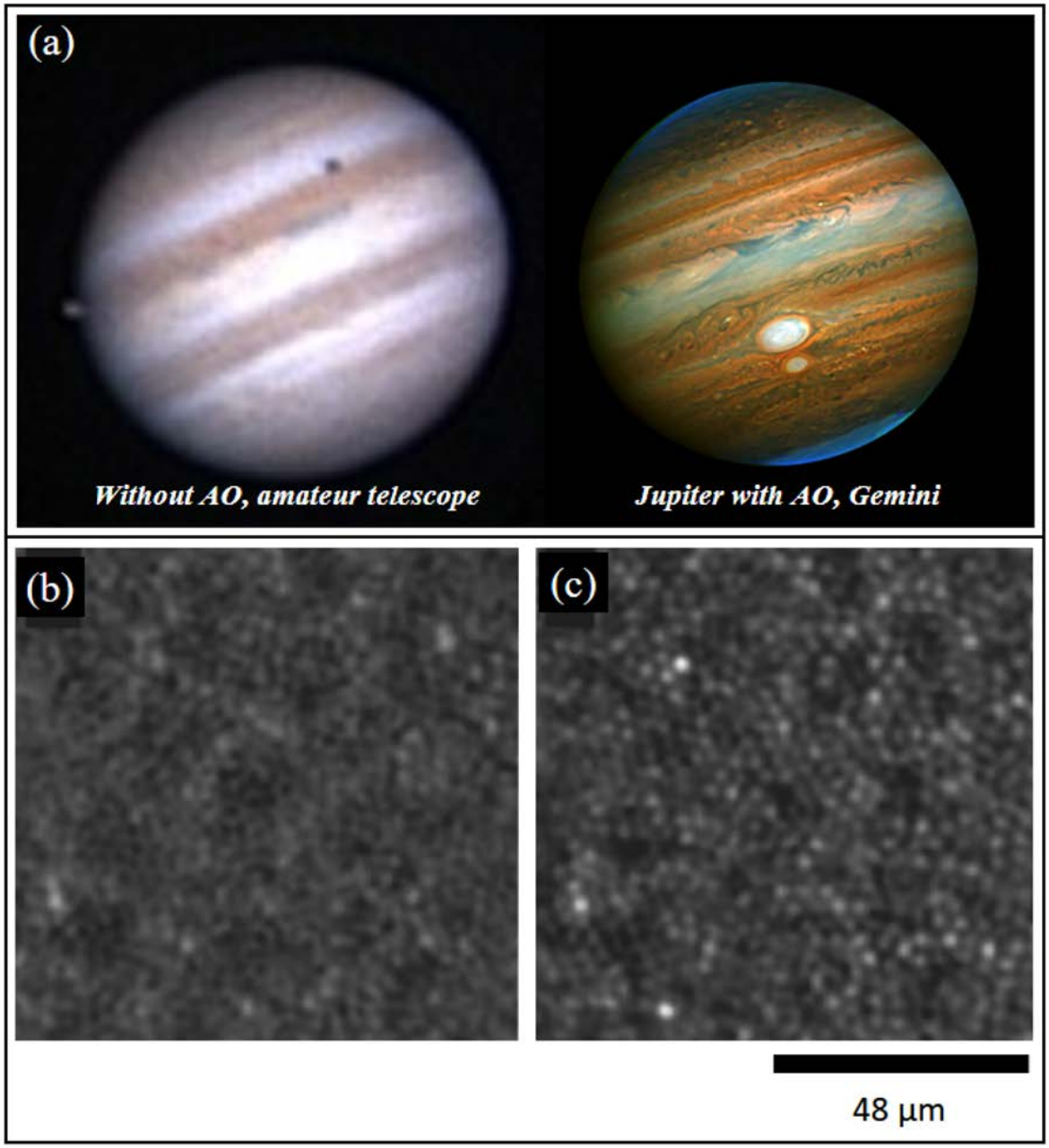

(a) Reproduced from [Gemini Captures Close Encounter of Jupiter's Red Spots. (2006, July 20). Retrieved February 20, 2018, from https://www.gemini.edu/node/196], with the permission of the GEMINI Observatory
(b) and (C): Reproduced from [Liang, J., Williams, D. R., & Miller, D. T., Supernormal vision and high-resolution retinal imaging through adaptive optics. *Journal of the Optical Society of America A*, 14(11), 2884–2892. 1997.], with the permission of the Optical Society

Figure 1.3: Improved image resolution after AO system (a) Comparison between seeing limited and AO-assisted imaging of the Jupiter (Gemini) [18]. Retinal image after bandpass-filter without (b) and with (c) AO compensation [15].

1.2 Motivation

One of the significant research challenges in AO technology is the ability to achieve sufficient mirror deformation stroke with low voltage operation. In the case of commercialized MEMS-based electrostatically actuated mirrors, whose electrostatic force can be controlled based on capacitance between two surfaces, stroke can be limited since the gap between the electrode and mirror is proportional to the actuation voltage. Additionally, the required high voltage driver occupies a large area, requires high power consumption, and increases the overall complexity of the system.

In contrast to electrostatic DM, many advantages can be found in MEMS Lorentz force controlled DM. In addition to low voltage operation, they offer bi-directional motion, with no magnetic hysteresis effect, enabling out-of-plane pushing and pulling motion. These benefits allow for the correction of surface flatness issues, such as gravity-induced deformation on mirror membranes. These advantages, combined with a simple actuator design, fast response, and reasonable power consumption, make them ideal for various DM applications.

The goal of this thesis is to design and fabricate a low voltage and large stroke MEMS-based Lorentz force continuous deformable polymer mirror (Lorentz DM) for AO applications. MEMS microfabrication has enabled the miniaturization of deformable mirrors, reducing power consumption and significant space occupancy. It has also enabled batch fabrication of numerous actuator elements together. This fabrication technique has produced a high level of reliability in the manufacturing process compared to classical macroscopic DMs.

The Lorentz actuator and 5 × 5 array actuator substrate and attached DM resulting from this research are shown in Figure 1.4(a), (b), and (c) respectively. As shown in Figure 1.4(d), the mirror surface can be deformed into various shapes by the force from the actuator array formed on the silicon substrate. The demonstrated Lorentz actuator design and working principle is shown in Figure 1.5. The actuator design is based on flexible supporting serpentine springs on either side of a central thick crossbar

above a permanent magnet. The z-directional Lorentz force on the crossbar is generated by the cross product of a current flow normal to a magnetic field.

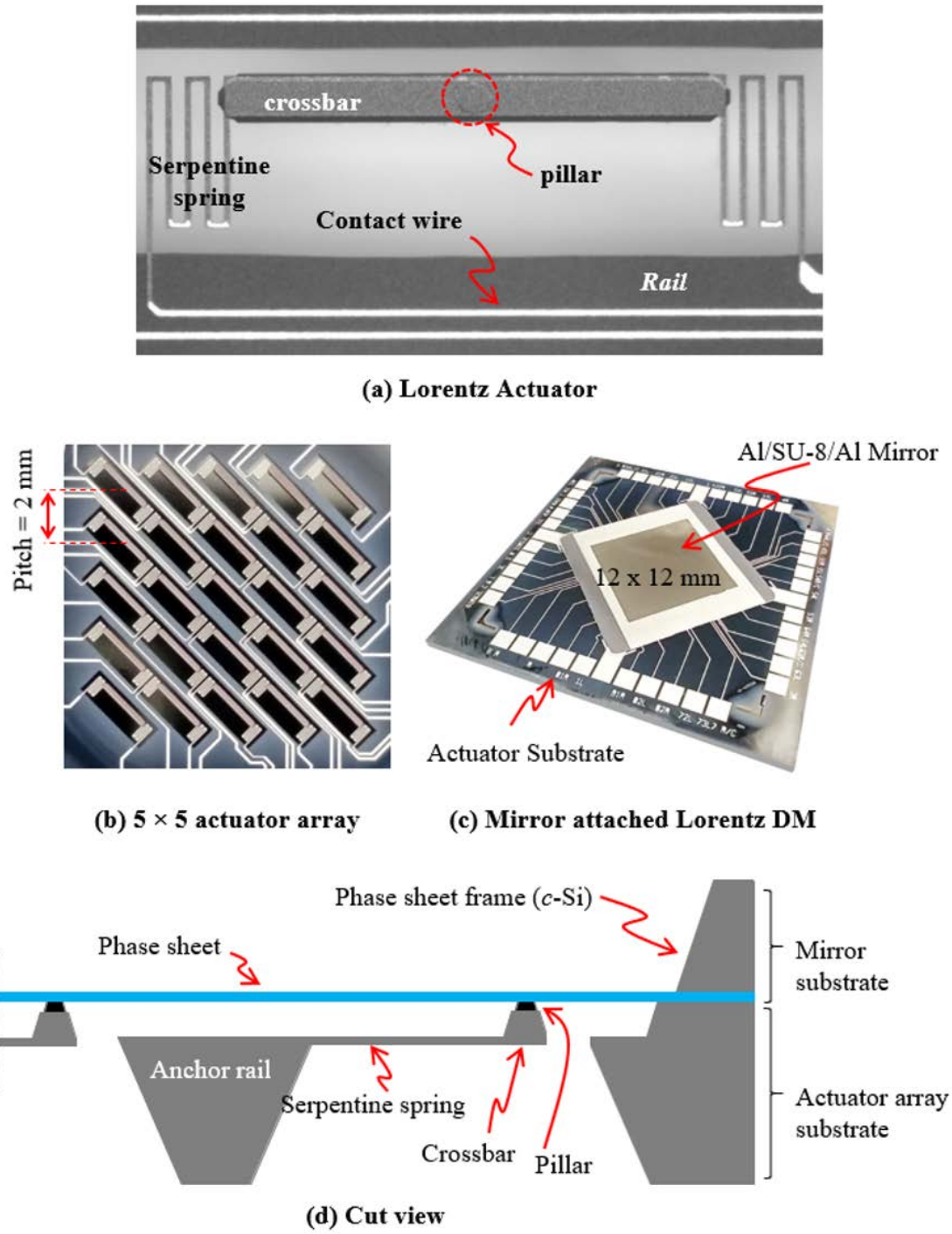

Figure 1.4: (a) Microscope image of a fabricated Lorentz actuator. (b) Photograph of 5 × 5 Lorentz actuator array. (c) Mirror attached DM structure. (d) Side view of assembled DM.

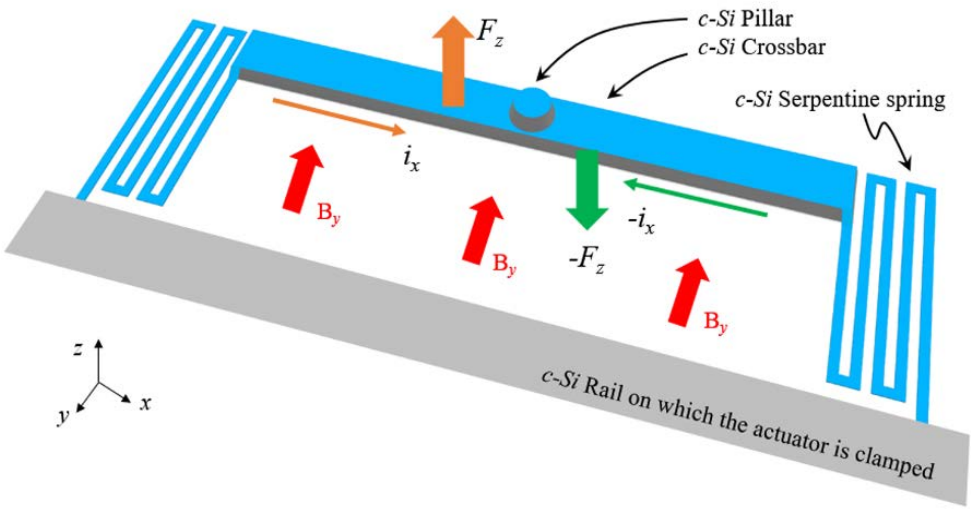

Figure 1.5: Illustration of the serpentine spring Lorentz actuator design and working principle.

1.3 Research Contributions

The contributions reported in this thesis include the novel design of a large out-of-plane Lorentz actuator, the development of its array and fabrication process, as well as the development of continuous deformable polymer mirror and its bonding technology to an actuator substrate. Analysis, modeling, and simulation of a Lorentz actuator for application to DM form a part of the reported achievements. The evaluation of the microfabricated device in experimental studies results in a demonstration of the advantages of applying the Lorentz actuator to various AO systems. A list of summarized research contributions is as follows:

- Design and fabrication of a 12 × 12 mm size continuous deformable polymer mirror with very flat and smooth surface topology. The flat mirror surface was achieved by coating both sides of the polymer membrane to compensate for the stress. The smooth topology of the mirror surface is achieved by transferring the surface of the chemical mechanical polished (CMP) silicon wafer to the mirror using the process developed from this research.
- Design, fabrication and feasibility evaluation of a cantilever arm Lorentz actuator by surface micromachining and bulk micromachining.

- Design and fabrication of a 5 × 5 array of serpentine spring actuators using a crystalline silicon substrate and bulk-micromachining techniques. Each actuator is connected to a rigid anchor rail which offers scalability of the array size. The rails also dissipate heat and provide space for an electrical wire connected to an external circuit.
- Demonstration of a DM design method through investigation of the correlation between the inter-actuator coupling of DM and mirror and actuator stiffness.
- Demonstration of a ± 17 μm deformation for the serpentine spring actuator attached Lorentz DM system at ± 3 mA actuation current and an operational voltage of less than 1 V. This Lorentz DM responded in 500 μs with very low overshoot, ensuring over 1 kHz operation frequency. The large stroke and the high operating frequency of the developed device show applicability to various AO technologies.
- Reporting large linear actuator deflection of ± 150 μm motion at ± 14.7 mA current within a 0.48 Tesla magnetic field. This actuator array is suitable for various 2D surface modification application due to its large deformation with low operational current and temperature, as well as a narrow contact area to a target surface.
- The bonding of the serpentine spring actuator and the mirror substrate was performed at a low temperature of 80 °C to prevent deformation induced by the thermal stress of the polymer mirror. Alignment between the two substrates was achieved using a specially designed mirror vacuum holder and ABM contact mask aligner.

Research Publications:

These research and relevant research results have been published in journals and conferences as follows.

[Journal Papers]

1. **Byoungyoul Park,** Elnaz Afsharipour, Dwayne Chrusch, Cyrus Shafai, David Andersen and Greg Burley (2018) A Low Voltage and Large Stroke Lorentz Force Continuous Deformable Polymer Mirror for Wavefront Control, *Sensors and Actuators A*, Accepted in July 24, 2018.
2. ***Cover Page* Byoungyoul Park**, Elnaz Afsharipour, Dwayne Chrusch, Cyrus Shafai, David Andersen and Greg Burley (Aug. 2017) Large Displacement Bi-Directional Out-Of-Plane Lorentz Actuator Array for Surface Manipulation, *Journal of Micromechanics and Microengineering*, Vol 27(8), pp. 085005,
3. Elnaz Afsharipour, **Byoungyoul Park**, and Cyrus Shafai (Feb. 2017) Determination of Reactive RF-Sputtering Parameters for Fabrication of SiOx Films Specified Refractive Index, for Highly Reflective SiOx Distributed Bragg Reflector *IEEE Photonics Journal*, 9(1), pp.1–16.
4. **Byoungyoul Park**, Meiting Li, Sampath Liyanage and Cyrus Shafai (April 2016) Lorentz force based resonant MEMS magnetic field sensor with optical readout, *Sensor and Actuator A*, 241, pp. 12-18.
5. **Byoungyoul Park**, Tao Chen and Cyrus Shafai (Sep. 2015) Design and Simulation of A MEMS Based Horseshoe Shaped Low Current Lorentz Deformable Mirror (LCL-DM), proceeding of *COMSOL 2015* in Boston, USA.

[Conference]

1. **Byoungyoul Park**, Ms. Elnaz Afsharipour, Mr. Dwayne Chrusch, Prof. Cyrus Shafai, Dr. David Andersen, Dr. Greg Burley (July 2018) Aluminum-Polymer Deformable Mirror using Electromagnetic Actuators for Spatial Light Modulation, *2018 International Conference on Optical MEMS and Nanophotonics (OMN)*, Lausanne, Switzerland, Accepted.
2. Elnaz Afsharipour, **Byoungyoul Park**, Ramin Soltanzadeh, Cyrus Shafai (July 2018) An electromagnetically actuated 3-axis gimbal-less micro-mirror for beam steering, *2018 International Conference on Optical MEMS and Nanophotonics (OMN)*, Lausanne, Switzerland, Accepted.

3. **Byoungyoul Park**, Elnaz Afsharipour and Cyrus Shafai (Aug. 2017) A Lorentz Force Actuated Continuous Deformable Polymer Mirror for Wavefront Control, *MDPI Proceedings in Eurosensor 2017*, 1, 554, doi:10.3390/proceedings1040554
4. Elnaz Afsharipour, **Byoungyoul Park** and Cyrus Shafai (Aug. 2017) Large Tilt Angle Lorentz Force Actuated Micro-Mirror with 3 DOF for Optical Applications, *MDPI Proceedings in Eurosensor 2017*, 1, 351, doi:10.3390/proceedings1040351
5. **Byoungyoul Park** (Aug. 2017) Study MEMS in the Heart of North America, Canada-Korea Conference 2017, Montreal, Canada, Oral Presentation.
6. **Byoungyoul Park**, Cyrus Shafai (Aug. 2017) A Low Voltage Lorentz Actuator Enabled Deformable Polymer Mirror (DPM) System for Smart MEMS Sheet, Canada-Korea Conference 2017, Montreal, Canada, Oral Presentation.
7. C. Ross, K. El-Sankary, S. Chapman, C. Shafai, **B. Park**, Y. Zhou, and G. Burley (June 2017) Next Generation Adaptive Optics on the TMT: An ASIC Driver for Low-Voltage MEMS Deformable Mirrors, *Adaptive Optics for Extremely Large Telescopes (AO4ELT5) conference*, Tenerife, Spain, 25-30.
8. **Byoungyoul Park**, Dwayne Chrusch, Cyrus Shafai (May 2016) Development of a Novel MEMS Based Horseshoe Shape Lorentz Actuator Array for Adaptive Optics, Manitoba Material Conference 2016, Winnipeg, Canada, Poster Presentation.
9. **Byoungyoul Park**, Dwayne Chrusch, and Cyrus Shafai (May 2016) Development of a Novel MEMS Based Low Current Lorentz Actuator Array for Adaptive Optics, CASCA Annual Conference, Winnipeg, Canada, Poster Presentation.
10. **Byoungyoul Park** and Cyrus Shafai (May 2015) A Low Current MEMS Lorentz Deformable Mirror (LCL-DM) System for Adaptive Optics, Manitoba Materials Conference 2015, Poster Presentation.
11. T. Chen, C. Shafai, A. Rajapakse, **B.Y. Park** (Sep. 2014) Micromachined Electric Field Mill Employing a Vertical Moving Shutter. Procedia Engineering in Eurosensor 2014, 87, pp. 452-455, https://doi.org/10.1016/j.proeng.2014.11.352.
12. **Byoungyoul Park**, C. Shafai, T. Chen, M. Li, and Y. Zhou (May 2014) The Cu/Cr/Cu Multilayered Horseshoe Shape MEMS Actuator with Low Current and Large Deformable Mirror for Adaptive Optics, Manitoba Materials Conference 2014, Poster Presentation.

1.4 Thesis Overview

This thesis is organized into eight chapters followed by appendices and bibliography.

- Chapter 1 introduces a comprehensive introduction of adaptive optics (AO), the motivation of the thesis, and a list of thesis contribution and its organization.
- Chapter 2 provides a literature review covering state of the art technology in MEMS-based DM compared with classical DM, including research background and the contributions of other researchers in the field. Also, the characteristics of the geometry and material of the mirror are compared.
- Chapter 3 presents the continuous deformable polymer mirror design and its optimization method by computer simulation using COMSOL Multiphysics software. The characteristics of the mirror fabricated by the bulk-micromachining process are analyzed.
- Chapter 4 introduces a MEMS-based Lorentz actuator, and compares its advantages and disadvantages. Justification for selecting a Lorentz DM will be given, and two different actuator designs are presented. One being a cantilever arm Lorentz actuator, and the other a serpentine spring-based Lorentz actuator for driving the DM mirror. Modeling and computer simulation for optimizing each actuator design is presented.
- In Chapter 5, the actuator fabrication process using surface micromachining and the electroplating technique for the cantilever arm Lorentz actuator is briefly introduced. Methods for solving problems found in an electroplated thick Cu crossbar and an actuator release process is discussed. Also, the fabrication process of the newly proposed serpentine spring Lorentz actuator is demonstrated using a bulk-micromachining process.
- Chapter 6 introduces an experimental set-up for the Lorentz actuator and mirror device characterization. Actuators with various spring thicknesses were evaluated and compared with the simulation results. The prepared 5 × 5 actuator array substrate and mirror substrate are

bonded together and characterized by an optical and electrical test bench. The static and dynamic behavior of the actuator and Lorentz DM device is analyzed.

- In Chapter 7, a brief discussion of the bonding technique between the actuator and the mirror will examine the possibility of applying AO technology to high order wavefront aberration.
- Chapter 8 provides a summary of the research developed in this dissertation and a list of future work that should be performed in order to build on the project. The chapter ends with concluding remarks with highlights showcasing the implications of the work.

2

Deformable Mirror (DM) for Adaptive Optics (AO)

Contents

2.1 Classical DMs

The classical DM systems are mainly driven by ferroelectric (piezoelectric or electrostrictive) or voice-coil mechanisms due to their relatively high stroke, high accuracy, and fast response time. For the piezoelectric DM, the very thin mirror surface is deformed by compression or expansion of many

piezoelectric actuators arrays according to the intensity of the applied voltage. Actuators are fabricated from a solid block of lead zirconate titanate (PZT) and are attached underneath the mirror membrane. The most advanced piezoelectric DMs are stacked array DMs and bimorph DMs (see Figure 2.1) [3]. Both stacked array DM system and bimorph DM systems can provide over ± 5 µm stroke with an approximate control voltage of ± 400 V at 10 kHz and 1 kHz frequencies, respectively. These conventional piezoelectric DMs cost ~ $1,000 per actuator due to their structural complexity and low fabrication yield.

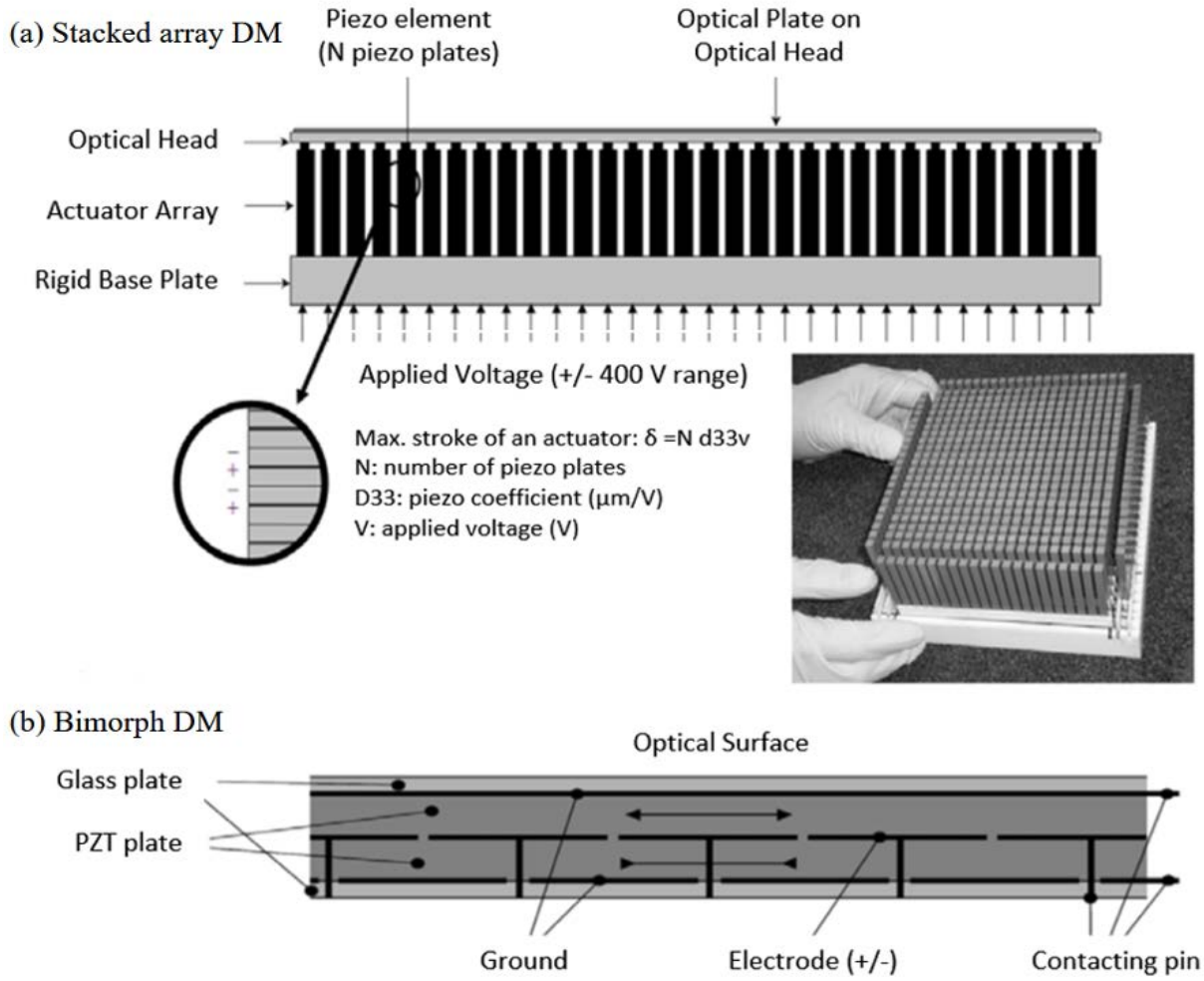

Reproduced from [Madec, P.-Y., Overview of deformable mirror technologies for adaptive optics and astronomy. In *SPIE Astronomical Telescopes+ Instrumentation*, International Society for Optics and Photonics, pp. 844705–844705, 2012.], with the permission of SPIE and author P-Y Madec.

Figure 2.1: Schematic diagram of the operation principle of the ferroelectric actuator. (a) Stacked arrayed DM and (b) Bimorph DM [3].

The electrostrictive DM was studied and fabricated on the basis of lead magnesium niobate (PMN) electrostrictive actuators with sensitivities ranging from 0.3 nm/V to 12 nm/V, as reported by Ealey [6] (see Figure 2.2). The PMN actuators have low hysteresis because of it is non-polarized nature and do not age or creep, unlike PZT actuators. However, PMN introduces design issues related to nonlinear material behavior and prestress effects. In addition, as in the case of the PALM-3000 (JPL Adaptive Optics) which consists of the most recently developed 3388 electrostrictive actuators, a very high operational voltage of over 300 V is required for a stroke of around 1 μm [7,8]. Such high operational voltages cause many problems in integrating the DM with on-chip driving circuits. Therefore in these cases, the high voltage DM requires multiple wire connections to external high voltage amplifiers. This results in a large space occupancy, high power consumption, and increased complexity of the system.

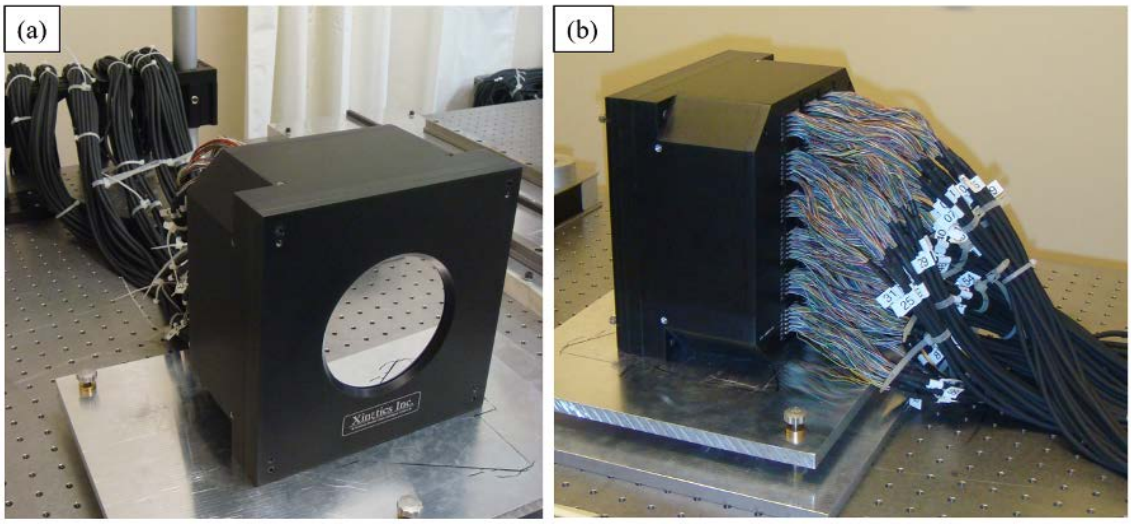

Reproduced from [A. H. Bouchez *et al.*, Status of the PALM-3000 high-order adaptive optics system. *Proc. Of SPIE,* vol. 7439, p. 74390H, 2009.], with the permission of SPIE

Figure 2.2: (a) Photograph of the front side of the 3388-electrostrictive actuator DM (PALM-3000), (b) photograph of the backside of the DM cable connected with each actuator node to apply high operational voltage up to 400 V [8].

In conventional AO technology, the voice-coil actuator DM system is the most recent technology, and it is based on the use of a thin floated optical shell on the magnetic field created by an array of voice coil actuators as shown in Figure 2.3. The voice-coil actuator DM can create a stroke of around 50 - 70

μm at a frequency of 80 kHz with an actuator pitch of 30 mm. The power consumption for 8 m class telescopes is about 1500 – 2,500 W and requires cooling equipment.

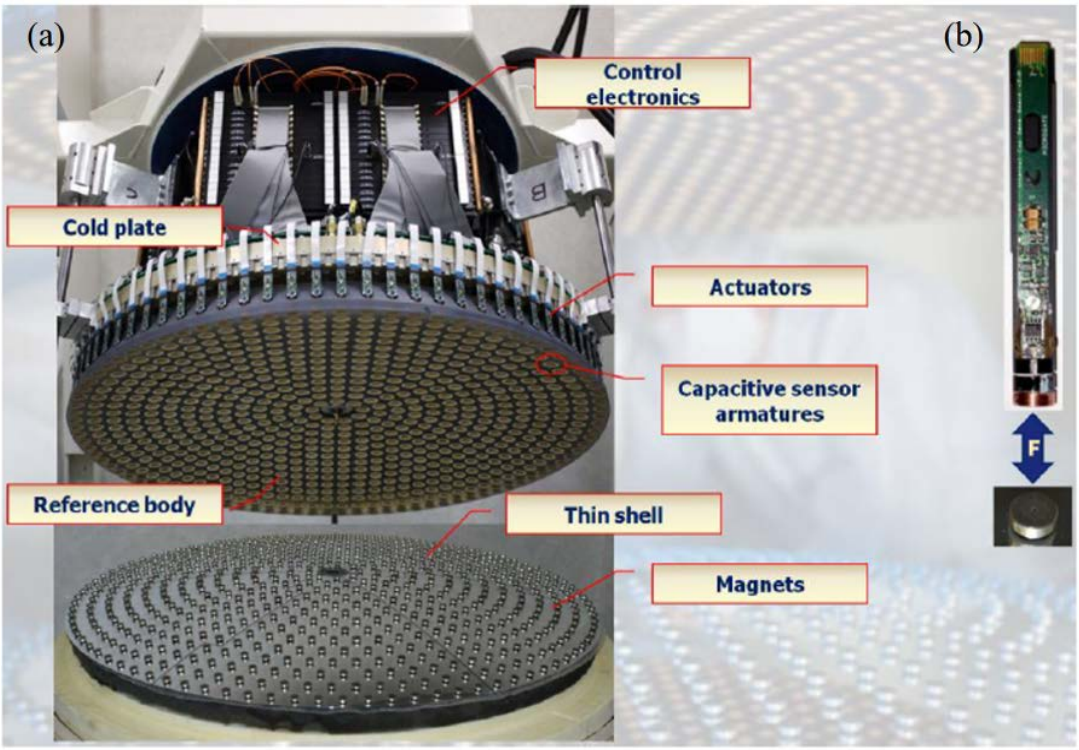

Reproduced from [Biasi, R., Gallieni, D., Salinari, P., Riccardi, A., & Mantegazza, P., Contactless thin adaptive mirror technology: past, present, and future. *In Adaptive Optics Systems II*, International Society for Optics and Photonics, Vol. 7736, p. 77362B, 2010.], with the permission of SPIE and author Roberto Biasi.

Figure 2.3: Voice-coil actuator DM [19]. (a) Secondary DM with the thin shell lying on its supporting tool for the Large Binocular Telescope (LBT). (b) a cut-off of voice coil actuator.

2.2 MEMS DMs

The traditional DM systems are costly due to their overall complexity, high power consumption, significant space occupancy, and high-risk manufacturing process. Therefore, the new generation of MEMS-based DM technology has been studied focusing on a compact size, low power consumption, and high-cost efficient features.

Four main transducing mechanisms, piezoelectric, electromagnetic, thermal, and electrostatic, have been studied as a driving force for the MEMS actuator in the last two decades. Each of which has its

advantages and restrictions [20]. For example, the piezoelectric material is not compatible with semiconductor fabrication technology, and a magnetic field and magnetic material require relatively complex structured electromagnetic actuators. The thermal actuator can supply a significant force and stroke, but suffer from high power consumption and long response time. The electrostatic actuators are more widely used due to their high level of compatibility with microfabrication processes, low power consumption, simple structure, and fast response time. However, it still requires a high operational voltage and shows nonlinear behavior. Lorentz force excited MEMS actuators have a bi-directional motion and no magnetic hysteresis effect. Also, they do not require a magnetic material which is not compatible with conventional semiconductor fabrication processes. These advantages result in the simple design of actuators with a fast response, reasonable power consumption, and ideal for large stroke applications [21,22].

This section will discuss electrostatic force based DM, which have been studied extensively and commercialized. Next, the piezoelectric and electromagnetic force based DM which offer considerable deformation and lower operation voltage are compared to electrostatic DM. Finally, the Lorentz actuator used as the driving element of the DM in this thesis will be discussed.

2.2.1 Electrostatic DM

Since the electrostatically actuated DM was first introduced by M. Yellin in 1976 [23], much research was undertaken. The fundamental principle of electrostatic DM is using the attraction force between two parallel plates when applying different voltages on each plate. Equation (2.1) describes the motion of an electrostatic actuator [21].

$$F_{ES} = -\frac{1}{2}\varepsilon_0 A\left(\frac{V_m - V_s}{z}\right)^2 \tag{2.1}$$

Where V_m is the voltage on the membrane, V_s is the voltage on the nearby voltage source (pull-down electrode), A is electrode area, ε_0 is vacuum permittivity, and z is the distance separating the

membrane and voltage source. From this equation, an electrostatic actuator can only have a pulling (attraction) force. Consequently, an electrostatic force is inversely proportional to the square of the distance between the two electrodes.

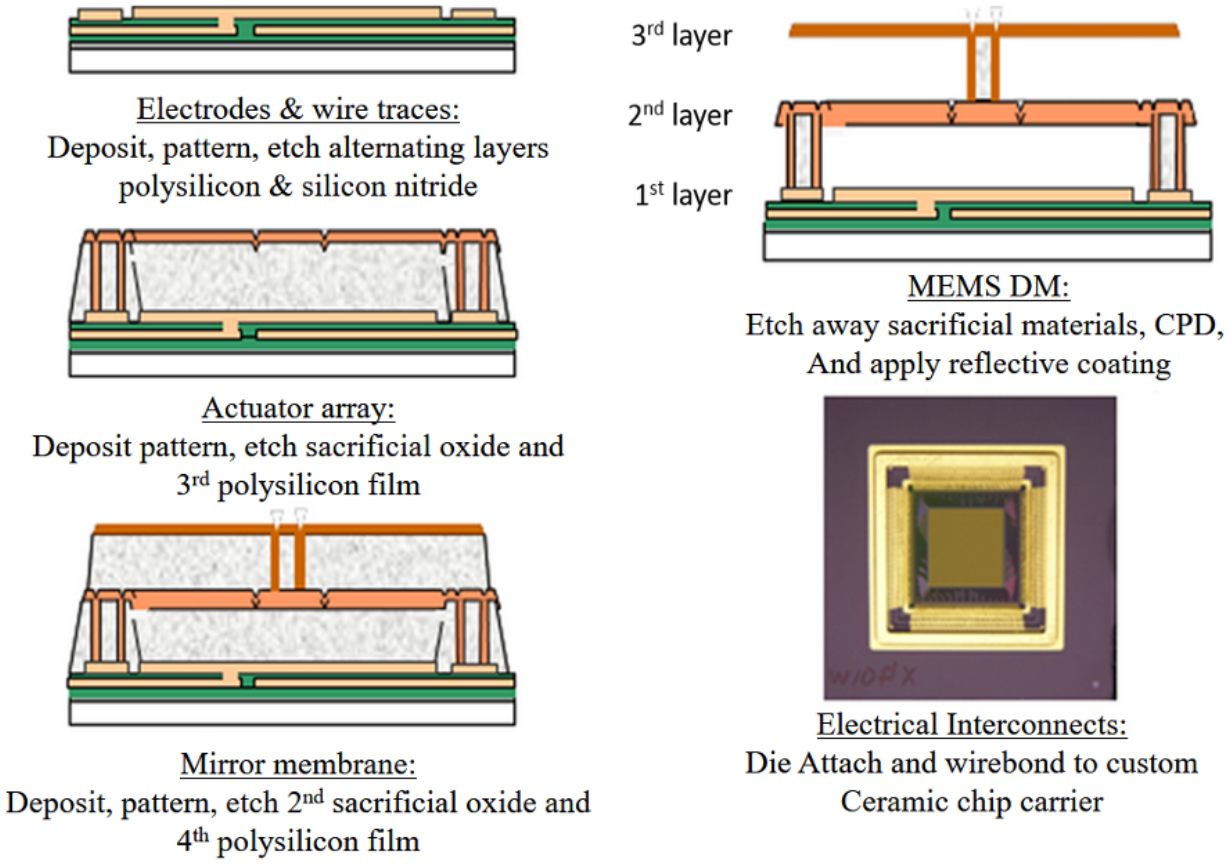

Reproduced from [Hill, A., Cornelissen, S., Dillon, D., Lam, C., Palmer, D., & Saddlemyer, L., Flexure mount for a MEMS deformable mirror for the Gemini Planet Imager, *Proceedings of SPIE*, Vol. 8450, pp. 84500H–84500H–12, 2012. https://doi.org/10.1117/12.926842], with the permission of SPIE and author Steven A. Cornelissen.

Figure 2.4: MEMS DM manufacturing process. Conducting and insulating thin films are deposited and selectively etched to build up the electrodes, pillars, and the membrane [24].

One of the leading companies in the MEMS DM technology, Boston Micromachines Corp., founded in 1999 in Cambridge, Massachusetts, is the first MEMS-based electrostatic DM supplier. The electrostatic force created by the applied voltage between the 1st layer (bottom electrode) and the 2nd layer (actuator electrode) pulls the actuator membrane. As a result, the mirror face-sheet (3rd layer) is deformed

corresponding to the actuator movement (see Figure 2.4). Their latest 64 × 64 actuator array DMs are capable of generating a stroke of 3.5 µm with 300 ~ 450 µm actuator pitch with thin polysilicon membrane [24]. It is also capable of working with a frequency of ~ 10 kHz with a minimal inter-actuator coupling (13 %). The inter-actuator coupling is expressed as a percentage of the displacement of the surrounding actuator relative to the displacement of the poked actuator. This continuous membrane DM system has an surface roughness of < 10 *nm* RMS with a 99.8 % fill factor. However, it suffers from high operational voltage (> 200 V) for ~ 5 µm deformation, due to its small electrode surface area and rigid mirror membrane. Also, its fabrication process (polyMUMPs and wet etching) is susceptible to material defects that are difficult to eliminate. The low fabrication yield is a significant problem. Moreover, there is well-known instability caused by the electrostatic force between two parallel plates that happens at 2/3 of the initial gap. This is known as the static pull-in condition [25]. Therefore, the gap between the two plates should be large enough to increase the driving voltage.

Fernandez et al. [26] replaced the polysilicon membrane with a softer gold membrane. The gold membrane was able to move 6.4 µm with an actuation voltage of 360 V. In order to decrease the driving voltage further; a flexible organic polymer was employed. An epoxy-based SU-8 membrane combined with an electrostatic actuator was reported in [27]. It achieved a stroke of 12 µm at 220 V with an electrode gap of 20 µm. In [28], a polyimide deformable mirror showed a 39 µm stroke at 195 V with an electrode gap of 82 µm.

2.2.2 Pretension Electrostatic DM

Iris AO, Berkely, USA, provides 111 and 489 arrays of hexagonal shaped segmented DM [29]. The 700 *µm* diameter hexagonally shaped segment mirror shown in Figure 2.5 is well aligned with the actuator pattern. The three bimorph flexures under the actuator platform offer pretension in the z-direction corresponding to the film stress of the bimorph flexures. The tip, tilt and piston motion is controlled by the applied voltage on all three electrodes beneath the actuator platform. The 489 array DM can provide 5

to 8 µm stroke at a frequency above 1 kHz. However, this DM still requires a driving power density greater than 100 W/cm^2. Also, combining it with the continuous membrane is nearly impossible because the force required to deform the membrane is much higher than the force generated from a pre-tensioned bimorph flexure. This is also true for polymer-based flexible membranes.

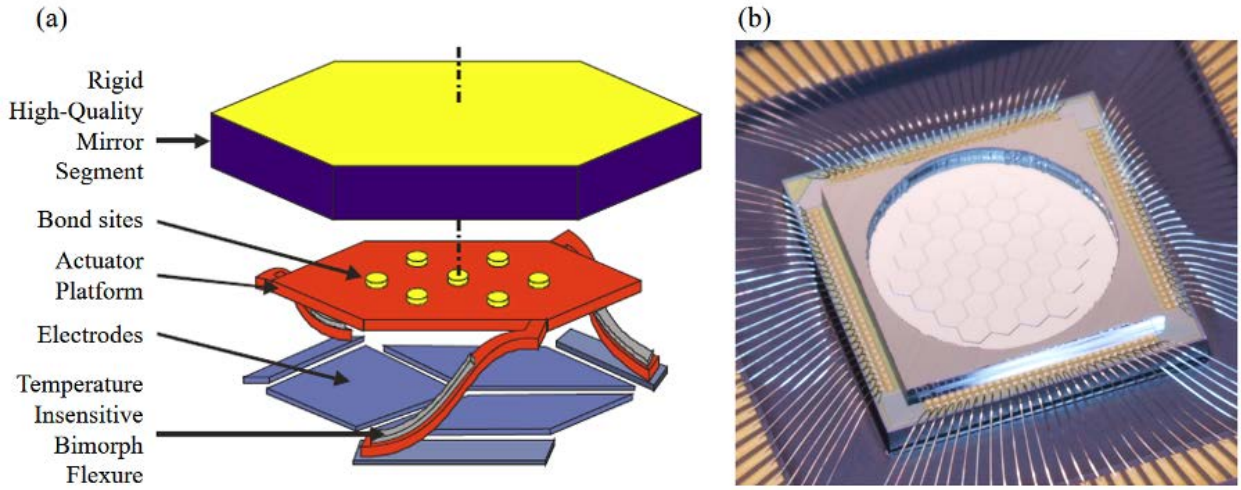

Reproduced from [Helmbrecht, M. A., He, M., Kempf, C., & Rhodes, P., Scaling up of the Iris AO segmented DM technology for atmospheric correction. *In Proc. 10th Adv. Maui Opt. Space Surveillance Technol. Conf.*, pp. E72, 2009.], with the permission of Author Michael Helmbrecht.

Figure 2.5: (a) Schematic diagram of an Iris AO DM segment. (b) Die photograph of a 111-actuator 37-piston/tip/tilt-segment DM with 3.5 mm inscribed aperture [29].

2.2.3 Piezoelectric DM

Extensive research has been conducted to fabricate piezoelectric actuators due to their ability in generating large stroke, and having a fast response time. However, a MEMS-based piezoelectric actuator for AO applications was introduced only recently due to the difficulty in controlling the surface roughness of the PZT material, its high operational voltage, and poor compatibility with the semiconductor fabrication processes [30]. A MEMS-based piezoelectric unimorph microactuator array for DM is introduced in [30], which can deform a 100 µm thick c-Si mirror. The actuators consist of a unimorph structure of PZT film and Si elastic layer (see Figure 2.6(a)). Deposited PZT material was thinned by a

lapping and polishing method to reduce surface roughness and uneven thickness. A 100 µm thick silicon mirror structure was then attached to the PZT film. The designed active area with a diameter of 35 mm is shown in Figure 2.6(b). The measured static deformation is 7.4 µm with an operational voltage of 100 V for 40 µm thick PZT films. The mirror had a resonance frequency of 18 kHz. However, the fabricated mirror surface shows a low order aberration of around 1 µm due to a rough PZT surface. Also, high order aberration formed from the attached post is reported.

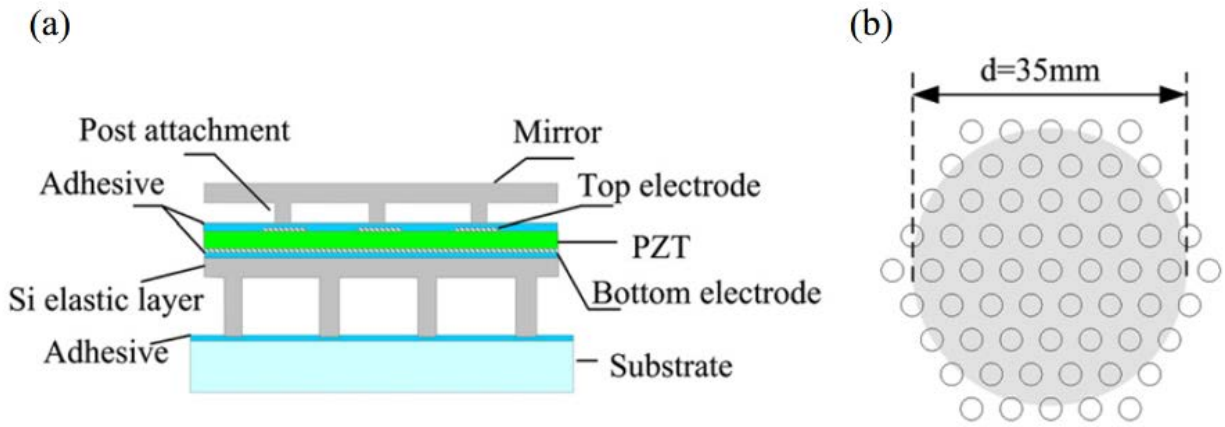

Reproduced from [Ma, J., Liu, Y., Chen, C., Li, B., & Chu, J., Deformable mirrors based on piezoelectric unimorph microactuator array for adaptive optics correction. *Optics Communications*, Vol. 284(21), pp. 5062–5066, 2011. https://doi.org/10.1016/j.optcom.2011.07.021], with the permission of Elsevier

Figure 2.6: Schematic diagram of the piezoelectric DM. (a) A cross-sectional view of an Iris AO DM segment with three unimorph actuators. (b) 61 Actuators array with the active area (gray colored) [30].

2.2.4 Electromagnetic DM

The most appreciated benefits of MEMS electromagnetic actuators is that since they have bidirectional motion, they only need to move half the distance in comparison to an electrostatic actuator, which can only move downward. This enables correcting surface flatness issues related to gravity-induced deformation on larger diameter mirror membranes. However, the electromagnetic actuator is usually

designed as a relatively complicated structure since it requires multiple coils to produce sufficient magnetic flux.

A low voltage and large stroke deformable magnetic mirror was demonstrated in [31,32]. It employed an electromagnetic actuator and polymer mirror. The mirror consisted of a thin polyimide membrane (2-5 µm thickness) covered with a permanent magnet matrix and was mounted above an array of planar microcoils on a 50 mm diameter substrate (see Figure 2.7(a)). This work offered a massive 15 µm stroke at a voltage below 1 V with a current of 2.5 A. However, this electromagnetic coil based deformable mirror required high power, and resulted in significant local heating and optical distortion due to thermal convection of surrounding air. Additionally, this particular device suffered from uneven stress points on the mirror at the glue points of the magnets as shown in Figure 2.7(b), thus causing optical aberrations.

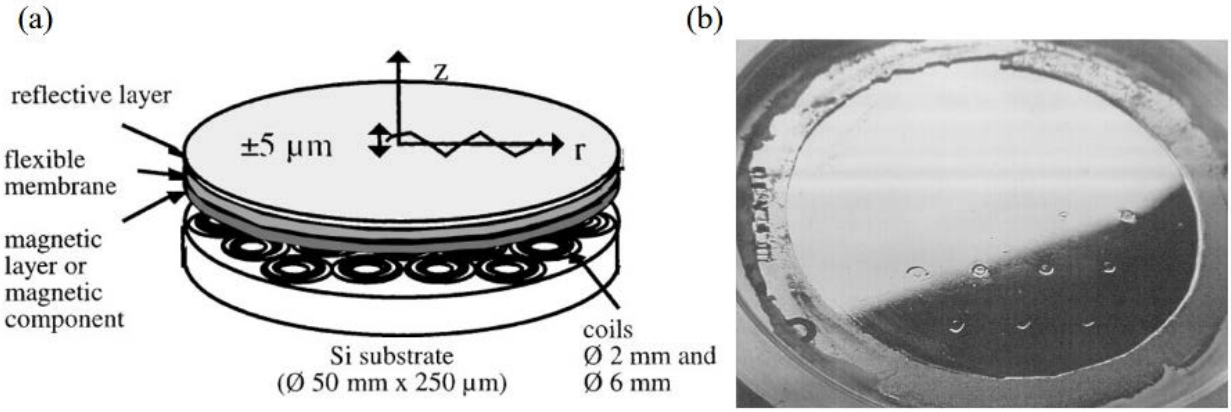

Reproduced from [Divoux, C., Cugat, O., Reyne, G., Boussey-Said, J., & Basrour, S., Deformable mirror using magnetic membranes: application to adaptive optics in astrophysics. *IEEE Transactions on Magnetics*, Vol. 34(5), pp. 3564–3567, 1998], with the permission of IEEE.

Figure 2.7: (a) Schematic diagram of the magnetic deformable mirror and its working principle. (b) Stress points on the mirror by the glued miniature permanent magnets [31].

2.2.5 Summary

Classical DM systems have several disadvantages of high structural complexity, high power consumption, and large space occupancy. On the other hand, MEMS technology is able to offer high-performance, cost-effective, and leaner and lighter electronic devices. However, MEMS-based electrostatic and PZT DMs still suffer from high operational voltages, complicated device structure, and low fabrication yield. The electromagnetic DMs can be driven at a low operational voltage of less than 1 V, but require a high current of over 2.5A and have a complex structure due to the coil structure required for generating a magnetic field.

2.3 Mirror Geometry and Material

2.3.1 Mirror Geometry

Low order wavefront distortion such as astigmatism can be corrected by moving a single lens or mirror. However, high order wavefront distortion, which is a result of heterogeneous light propagation media such as atmospheric turbulence, complex optical systems, and biological cells, requires correction on each part of the beam in real time. Segmented mirrors or continuous faceplate DMs are devices that work in this manner are called multichannel correctors. Figure 2.8 shows the schematic diagram of each device.

Segmented deformable mirrors consist of an array of compactly spaced mirror segments, and their piston, tip, and tilt motion are controlled by their respective actuators. Thus, correction of high-order distortion can be achieved by the individual contribution of each of the mirror segments. The shape of these segment mirrors can be made square, hexagonal, or circular. The segmented DMs have several advantages including the simplicity in replacing segments, no mechanical cross-coupling between mirror segments, matching closely to a geometrically registered wavefront sensor and having an unlimited

aperture by adding more segments. However, the discontinuities (gap) between the segments can scatter the incoming light in an undesirable and uncontrolled manner.

Multichannel continuous faceplate mirror includes a single section of the mirror and an array of actuators. Actuators can be discretely perpendicular to the surface (see Figure 2.8a) or continuous such as a bimorph mirror (see Figure 2.8b). The advantages of continuous DMs include a very sharp image because of negligible edge diffraction. Also, the wavefront to be corrected is commonly smooth, so using a well calibrated continuous DMs can produce better results than segmented DMs. However, this advantage is often diminished due to structural constraints that limit the shape of mirror that can be formed. The stress and strain in the mirror materials result in structural coupling between the actuators. The actual shape of the continuous DMs surface when it is pressed by a single actuator is called its influence function. It is a function of mirror faceplate parameters such as thickness, Young's modulus, and Poisson's ratio. This influence function can be measured and used to obtain the inter-actuator coupling coefficient [33]. In the continuous DMs, the inter-actuator coupling should be adjusted very precisely in order to have a precise mirror deformation shape.

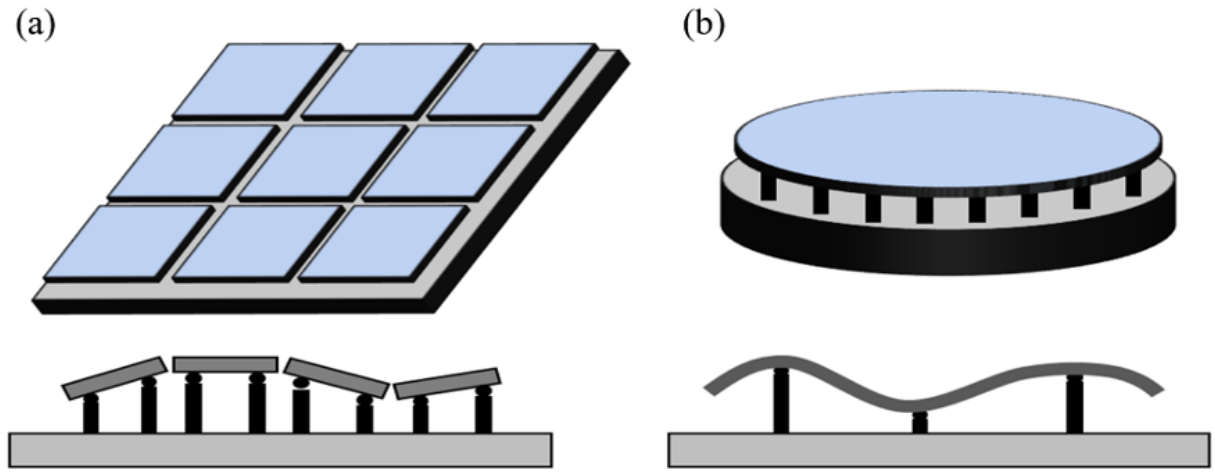

Figure 2.8 Two main categories of the deformable mirror. (a) Segmented and (b) continuous faceplate DM.

2.3.2 Mirror Material

2.3.2.1 Inorganic Rigid Mirror

Typically, continuous DMs consist of a flexible thin mirror faceplate and an array of actuators to activate a mirror deformation. Initially, MEMS-based continuous DM membranes were fabricated with crystalline silicon, poly-silicon, or silicon nitride. This is because they are a well-proven materials in the semiconductor industry [9,34,35]. The poly-silicon and silicon nitride membranes can be formed by sputtering, CVD, or PECVD techniques. These allow for achieving high smoothness of the film surface and low external residual stress due to the similar coefficient of thermal expansion (CTE) with a crystalline silicon substrate shown in Table 2.1. The c-Si membrane is fabricated using a bulk micromachining process, which means that the membrane consists of the same material as the substrate. However, its stiffness limits the membrane stroke range to less than 5 μm in most DM designs. Young's modulus, representing a stiffness of an elastic material, of these materials are much higher than that of polymer materials.

Table 2.1: Thermal and mechanical properties of the inorganic and organic material in DM membrane mirror structures [35-41].

Materials	Young's modulus (GPa)	Tensile or Yield Strength (GPa)	Density (g/cm^3)	Thermal Conductivity (W/mK)	CTE @R.T. (μm/K)
<100> *c-Si* [36,37]	162	6.9^Y	2.33	157	2.6
Poly-silicon [35,39]	150	1.2^T	~ 2.33	20 - 30	2.33
Silicon nitride [35,38]	130 (Sputter)	0.15^T	2.4 – 2.8 (PECVD)	18.5	2.8
Epoxy (SU-8) [39,41]	2	0.137^Y	~ 1.42	0.3	52
Polyimide [35,40]	8.67	0.05^T	~ 1.42	11.7	2

^{Y}: Yield Strength ^{T}: Tensile Strength CTE: Coefficient of Thermal Expansion

2.3.2.2 Organic Soft Mirror

The continuous deformable mirrors (CDMs) require a flexible and smooth mirror membrane to minimize the operational voltage in electrostatic and piezoelectric DMs, or current in electromagnetic DMs. This mirror material should also be compatible with microfabrication processes and have a compatible CTE to a silicon substrate to minimize thermal stress in the film. The most representative carbon-based polymer material is epoxy. Epoxy is a thermoset polymer consisting of 3-dimensional crosslinking of Bisphenol A and Epichlorohydrin shown in Figure 2.9. The chemical formula of epoxy resin shows a 3-dimensionally compact network structure of benzene that provides robust mechanical properties and chemical stability. Therefore, epoxy is very widely used from adhesives to advanced semiconductor and aerospace industries. In addition, cyclopentanone solution based epoxy (SU-8) generates a photo-acid after exposed to UV light and initiates polymerization by opening an epoxy ring [42]. Due to this photosensitive reaction, epoxy can be used for negative photoresists in the semiconductor process. Moreover, epoxy is highly transparent in the ultraviolet region, which allows for using it as a thick layer formable negative photoresist. The epoxy-based negative photoresist SU-8 was developed by IBM in 1989 [42], and is well established as a material for electroplating molds and general microstructures for MEMS devices. The critical thermal and mechanical properties are shown in Table 2.1.

The first research on developing epoxy based micro-beams and membranes structure for MEMS was conducted by Andrew Hartley [44]. In this paper, the various dimensions of SU-8 cantilevers and membranes were fabricated and tested. Soon after, an SU-8 membrane based electrostatic continuous deformable polymer membrane was reported by C. Friese et al. [27]. Figure 2.10 shows the schematic view of the SU-8 membrane based electrostatic DM. The gold is deposited and patterned on the substrate, followed by spinning and patterning the SU-8 spacer layer. Finally, the membrane coated top substrate is bonded on top of the spacer by using the direct polymer bonding technique. The maximum deformation achieved was 12 μm at 220 V on a 7 mm diameter membrane with 18 μm electrode spacing.

Polyimide based DM has also been studied, and was demonstrated to reduce the thermal stress generated by the significant CTE differences between crystalline silicon (2.6 μm/K) and SU-8 (52 μm/K). In [28], PI-2601 (HD Microsystems^{TM}) was chosen as the membrane material, which has relatively high Young's modulus (~10 GPa) as shown in Table 2.1. Research results showed a 40 Hz resonant frequency with a large deformation of 39 μm at 197 V on a 2.15 μm thick, 20 mm diameter membrane with an electrode gap of 82 μm. This resonant frequency is lower than that for commercial silicon-based deformable mirrors (which are commonly over ~ 1 kHz), only due to the larger diameter, and therefore larger mass of the structure. However, the polyimide-based DM still has a higher Young's modulus than SU-8, requiring a higher operational voltage or higher current under the same conditions.

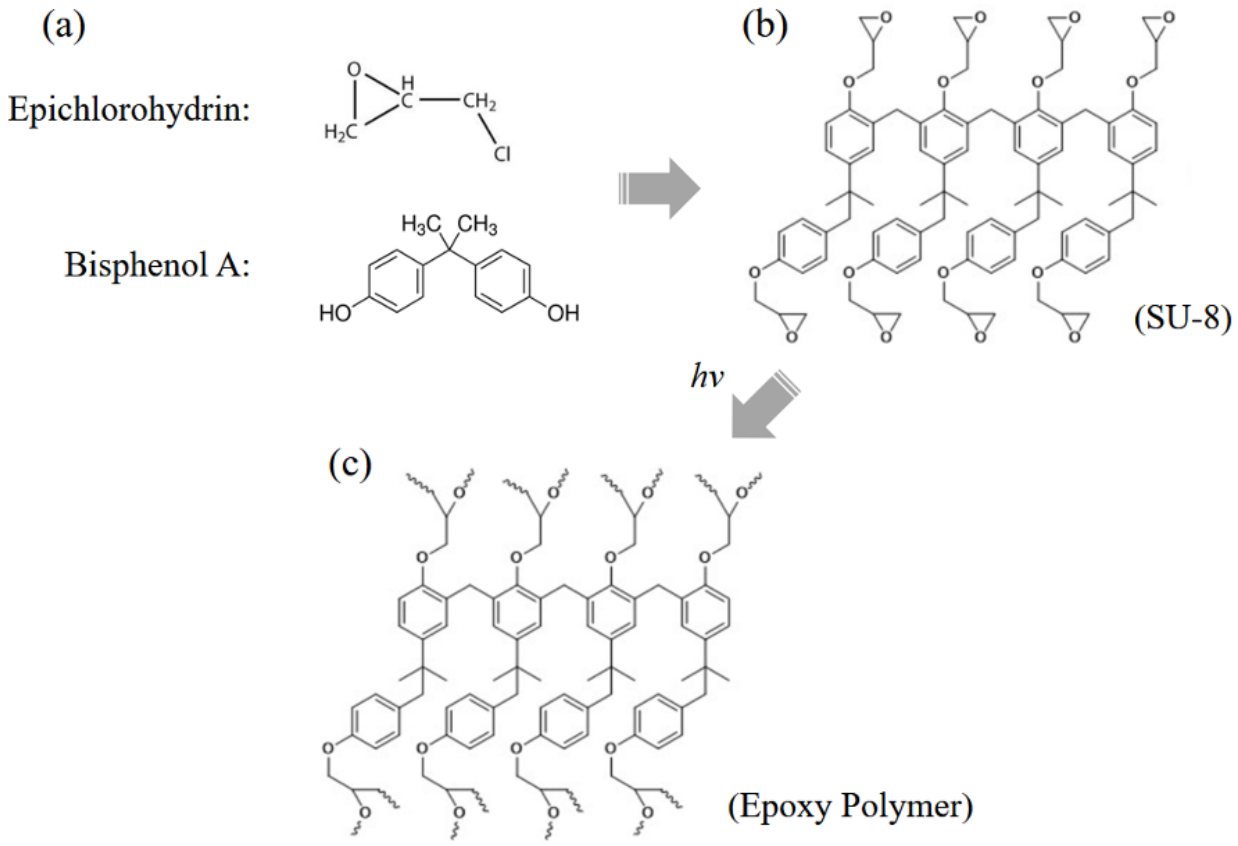

Figure 2.9: Chemical formula of epoxy and its monomers. (a) Reactants, (b) SU-8 monomer, and (c) 3D crosslinked epoxy structure after photoinitiated polymerization [88].

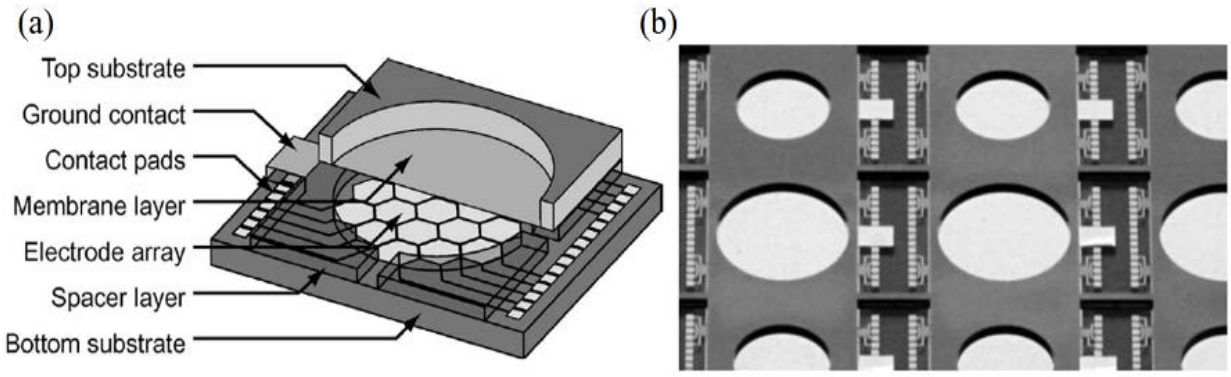

Reproduced from [Friese, C., & Zappe, H., Deformable Polymer Adaptive Optical Mirrors. *Journal of Microelectromechanical Systems*, 17(1), pp. 11–19. 2008. https://doi.org/10.1109/JMEMS.2007.913075], with the permission of IEEE.

Figure 2.10: (a) Schematic view of the deformable polymer membrane mirror, (b) Picture of the finished wafer stack after dry etching [27].

2.4 Chapter Summary

Although offering a sufficiently high deformation stroke and working frequency, the traditional DM technology has critical drawbacks including high power consumption, high cost, and significant space occupancy. Also, the most widely used electrostatic force based MEMS DM suffers from high operational voltage due to its one-directional motion and small electrode size. Therefore, it is desirable to use a MEMS-based Lorentz force actuator that has bi-directional motion, low power consumption, high thermo-mechanical stability, easy fabrication, and large deformation stroke. Furthermore, in order to have substantial displacements, it is necessary to increase the unit mirror cell size and to use soft material for the membrane in order to reduce power consumption. As a result, the MEMS-based Lorentz actuator with continuous polymer deformable mirror is the best alternative for AO.

3

Design and Fabrication of Continuous Deformable Polymer Mirror

Contents

3.1 Design Criteria of the DM

It was explained in Chapter 1 that adaptive optics technology is important for image correction of astronomical observations perturbed by the Earth's atmosphere. The problems caused by these perturbations are even more important for extremely large telescopes such as the ELT in Chile (aperture 39.3 m) [45], the GMT in Hawaii (aperture 24.5 m) [46], and the TMT in Hawaii (aperture 30 m) [47].

Thus, the new continuous deformable polymer mirror system will demand many more control channels, and will have a higher stroke. Moreover, due to the large size of the telescope structure, the image resolution of the telescope is determined by not only the wavefront distortion from atmospheric turbulence, but also by wind-induced structural vibration. The narrow field infrared adaptive optics system (NFIRAOS) for the TMT project consists of two DM with 10 μm stroke linear actuators [48]. The first DM has a 300 mm diameter with an array of 64 × 64 linear actuators that are mounted on a tip-tilt platform in order to correct for high amplitude image motion caused by the atmospheric turbulence of the ground layer. Low order wavefront distortion from high altitudes will be corrected by the secondary 360 mm diameter DM consisting of an array of 75 × 75 actuators.

In this thesis, we have studied mirror and actuator array systems for driving a DM for AO needed for a telescope similar to that of the TMT project. The required specifications are shown in Table 3.1 for the second mirror.

Table 3.1: Specification for the first DM of the TMT telescope.

Items	Specification
Dimension	64 x 64 actuators
Pitch	~ 2 *mm*
Actuator Stroke	10 μm
Actuation Speed	> 800 *Hz*
Mirror Surface Roughness	< 30 nm *RMS*
Inter-actuator coupling	10 – 30 %

The DM specifications of an AO system are defined from the overall AO error budget including the measurement noise, the tomographic reconstruction of the turbulent volume above the telescope, and the finite number of DM actuators, etc. There are four important concepts to consider in developing the specification. These are the Strehl ratio, the number of actuators, actuator mechanical stroke, and temporal response. The Strehl ratio is defined as the ratio of the peak perturbed image intensity from a

point source to the maximum attainable intensity of an ideal optical system limited only by diffraction. Depending on the AO application requirements driving the design of the telescope, its associated DM specifications can be different. Therefore, the specifications required for the TMT DM are discussed in Appendix A.

3.2 Design and Simulation of the DM System

3.2.1 Mirror Design

The low voltage Lorentz DM is comprised of an underlying Lorentz actuator attached to an overlying deformable mirror. According to the TMT DM specification in Table 3.1, the DM system requires deformation of ± 5 μm, an aluminum metal reflective surface for visible light observation, 2 mm pitch, an actuation speed over 800 Hz and 10 - 30 % inter-actuator coupling for adjacent mirror locations above each actuator. In this research, the 2D array of actuators is set to 5 × 5 to assess the feasibility of the design.

A schematic of the Lorentz DM is shown in Figure 3.1. The upper layer of the structure is a single crystal silicon frame clamping a 12 mm × 12 mm polymer mirror. An epoxy-based SU-8 photoresist is used as the structural material, which is compatible with semiconductor fabrication processes and has a low Young's modulus (about 2 GPa). The reflective surface is prepared by evaporating a thin aluminum film on both sides of the SU-8 membrane. The two-sided aluminum coating is used for stress-balancing, and protecting the SU-8 layer from corrosion and degeneration. The corrosion and degeneration can be caused by external moisture or oxygen. Each aluminum layer has a thickness of 250 nm, and reflectivity of over 80 % in visible light [49]. In the case of IR range observation, a reflective gold layer of approximately 120 nm can also be used which provides over 90 % reflectivity [50].

The actuator substrate attached underneath the mirror substrate provides the force needed to deform the mirror. To maximize this force, the actuator crossbar that creates the Lorentz force is rotated

45° from the *x*-axis, since the Lorentz force is proportional to the length of the crossbar in this design. The force provided by the Lorentz actuator has to be capable of deforming the mirror by 10 µm and be driven at a low current of a few mA to minimize power consumption. Joule heating induced by the current flowing in the wire should also be low, so as to minimize the mechanical property change of the material and limit thermal expantsion. The stiffness of the overall system (actuator + mirror) should be optimized with respect to the mass of the elements so that the Lorentz DM has a resonant frequency of over 800 Hz. Finally, the inter-actuator coupling created by the physical bonding of the actuators and the mirror should be designed to be 10 – 30 % depend on the applications. For example, with only 10 % inter-actuator coupling (rigid system), the system can compensate for higher order aberrations (good for astronomy telescopes). On the other hand, high inter-actuator coupling of ~ 30 %, can correct low order aberrations (good for retinal imaging). A more detailed discussion about the Lorentz actuator array design is explained in Chapter 4.

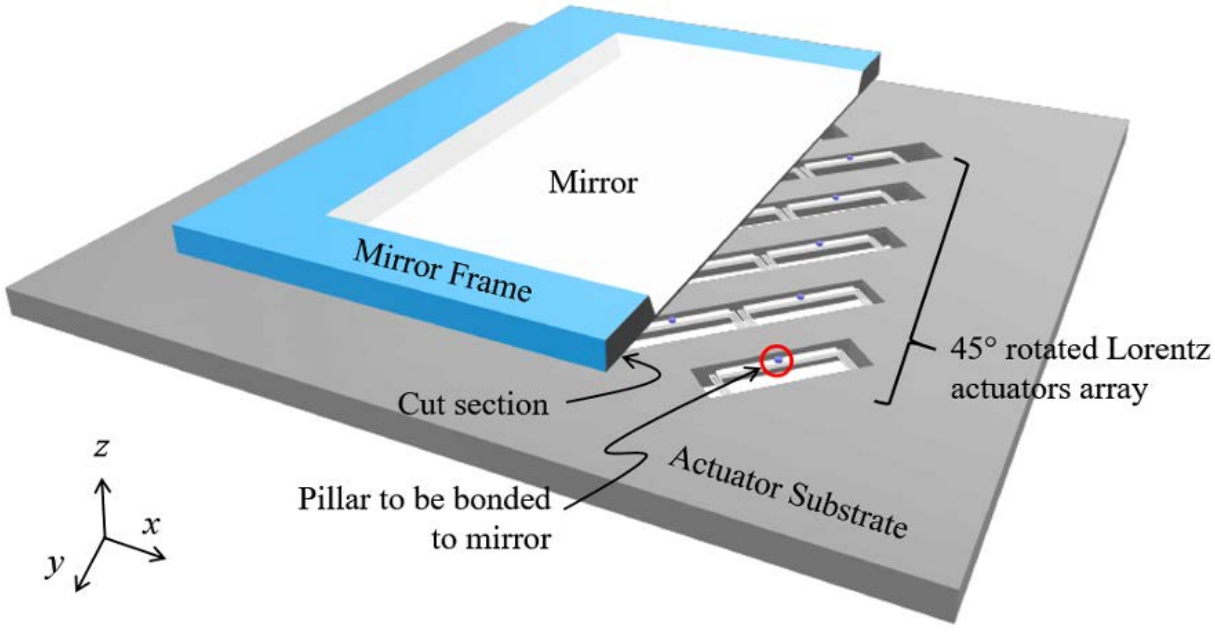

Figure 3.1: Illustration of the Lorentz DM consisting of the continuous deformable polymer mirror and 5 × 5 actuator array.

3.2.2 Boundary Conditions of the COMSOL Simulation

It is difficult to understand the correlation between mirror deformation, inter-actuator coupling, and actuator spring constant, due to the complexity of the mutual behavior of the actuator array and the thin elastic membrane mirror deformation. Therefore, FEM simulation using COMSOL Multiphysics software in order to study the Lorentz DM performance is performed under the boundary conditions defined in this section [51].

Figure 3.2 shows the boundary conditions under clamped mirror (red line). Here, the clamping means that there is no translation or rotation permitted ($x = 0$, $y = 0$, and $z = 0$). The model consists of a 5 × 5 actuator array, beneath a 12 mm x 12 mm square mirror clamped at the outer boundary. The mirror is divided into a square area of 2 × 2 mm^2 containing the geometry of the actuator array. Therefore, the dimension of the square shape unit-cell mirror is defined as 4 × 4 mm^2 along the pitch of the actuator.

The mirror is constructed by coating 250 nm thick aluminum films on both sides of the 4 μm thick SU-8 film. The material properties used in this model are listed in Table 3.2. The central actuator node is subjected to a force in the z-direction by the actuator. All actuator attached nodes are made of the same material as the mirror, but their Young's modulus is set to 169 GPa (equivalent to crystalline silicon) to account for the effect of a rigid silicon pillar contact area on the actuator. The actuator stroke is fixed at 5 μm since the required mirror stroke is 10 μm and the Lorentz actuator has bi-directional out-of-plane motion. Various geometrical combinations are studied by parameterizing the entire structure.

The overall COMSOL simulation was broken down into three individual steps, in order to achieve accurate simulation results and reduce computation time.

STEP 1: Simulate the mirror deformation and the maximum stress for 5 μm deformation.

STEP 2: Simulate the resonance frequency and deformation shape of the mirror.

STEP 3: Simulate the spring constant of the Lorentz actuator for various inter-actuator coupling of the Lorentz DM.

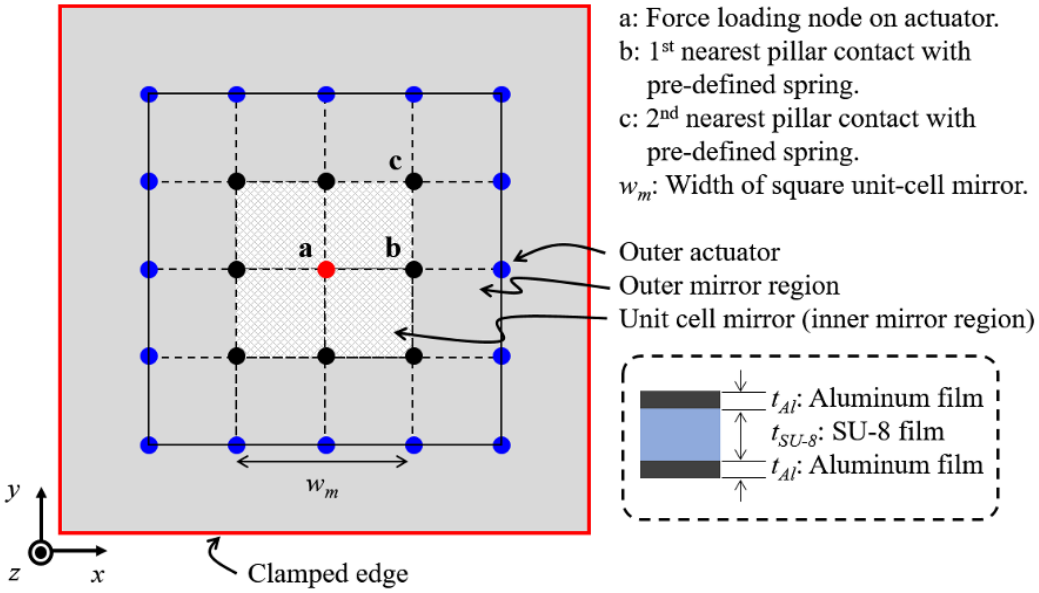

Figure 3.2: Boundary conditions of the membrane and its vertical structure (lower right corner).

Table 3.2: Material properties for the mirror [40,52]

Properties / Material	SU-8	Aluminum
Density (Kg/m^3)	1219	2700
Young's Modulus (GPa)	2	69
Poisson's Ratio	0.22	0.35
Thermal Conductivity (W/m·K)	0.3	237
Heat Capacity at Constant Pressure (J/(kg·K))	1420	904
The coefficient of Thermal Expansion (µm/K)	52	23.1
Specific Heat (J/Kg/K)	-	898.7
Yield Strength of Thin Film (MPa)	137 [52]	124 [40]

3.2.3 Mirror Deformation and Stress Failure (STEP 1)

Simulations are carried out using a 3D solid mechanics interface under the structural mechanics toolbox in the COMSOL Multiphysics software. The Solid Mechanics interface is based on solving

equations of motion together with a constitutive model for a solid material. Variables such as displacements, stress, and strain are computed.

For the boundary conditions of the mirror, all actuator nodes except the central actuator node (a) and all sides of the mirror are clamped. The force required to have z-axis out-of-plane deformation in the unit cell mirror is loaded on the central actuators. The stress and strain created by the central loading force are spread over the entire area of the mirror due to continuous mirror geometry. In this step of the simulation, it is assumed that the actuator joint is clamped in order to find the maximum required force for 5 µm membrane deformation and the maximum stress. The resonance frequency of the Lorentz DM system with 10 to 30 % inter-actuator coupling is simulated in step 2.

The mirror structure in Figure 3.2 is constructed in the model builder, and the boundary conditions are defined through the solid mechanics module. The design parameters and definitions for the mirror are given in Table 3.3. Among these parameters, F is arbitrarily increased to the range where the deformation value of the unit cell mirror becomes 5 µm. For efficient and accurate simulation, a free triangular mesh is selected that matches the mirror geometry. Mesh size is applied differently for each region of actuator nodes, and for the inner and outer mirrors. In the simulation, the computation result, time, and memory usage vary greatly depending on the mesh size. Therefore, the mesh dependence of the simulation is investigated to find the most efficient number of meshes. This mesh evaluation is applied equally to all further simulations, but a detailed description is given only in this section in order to reduce the redundancy of the thesis.

Table 3.3: Simulation parameters, definitions and the simulated range for the mirror design.

Parameter	Definition	Range
w_m	Width of square shape unit mirror width	2000 µm
t_m	Mirror thickness	4.5 µm
F	Applied force on the central actuator node	0.1 to 20 µN

Figure 3.3 shows the unit cell mirror deformation and computation time as a function of number of domains in the mirror structure depending on the number of mesh. As shown in Figure 3.3, the maximum deformation of the unit cell mirror is saturated at around 10,000 meshed domains, and the computation time is about 50 seconds. Therefore, the number of domains is fixed to 10,000 in this simulation.

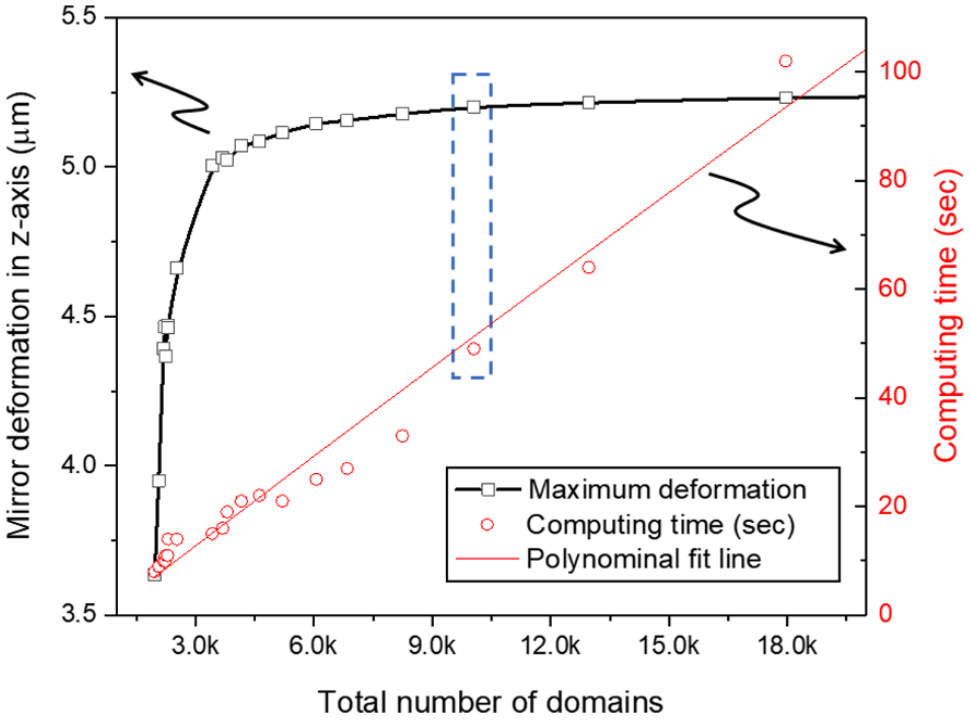

Figure 3.3: Maximum mirror deformation and computation time as a function of the number of mesh domains in the unit cell mirror.

We can see from Figure 3.4 that the unit cell mirror requires 12 μN of force to cause a deformation of 5 μm at the central actuator node location, which corresponds to a spring constant (k_m) of 2.4 N/m. Deformations of less than around 3 μm follow a linear deformation profile as a function of force applied on the unit cell mirror. At deformations greater than 2 μm, the deformation profile becomes nonlinear. The nonlinear mirror deformation occurs when the strain is limited by the confined structure. This typically happens when the deformation is greater than half the thickness of the elastic material [53]. The nonlinearity of the mirror deformation can be reduced by attaching actuators which reduce

geometrical confinement. The maximum equivalent stress produced in the 5 µm deformation of the mirror is 6.1 MPa around the central node. Since this stress is less than 5 % of the yield strength of SU-8 and aluminum of 137 MPa and 124 MPa respectively, no damage to the mirror is expected.

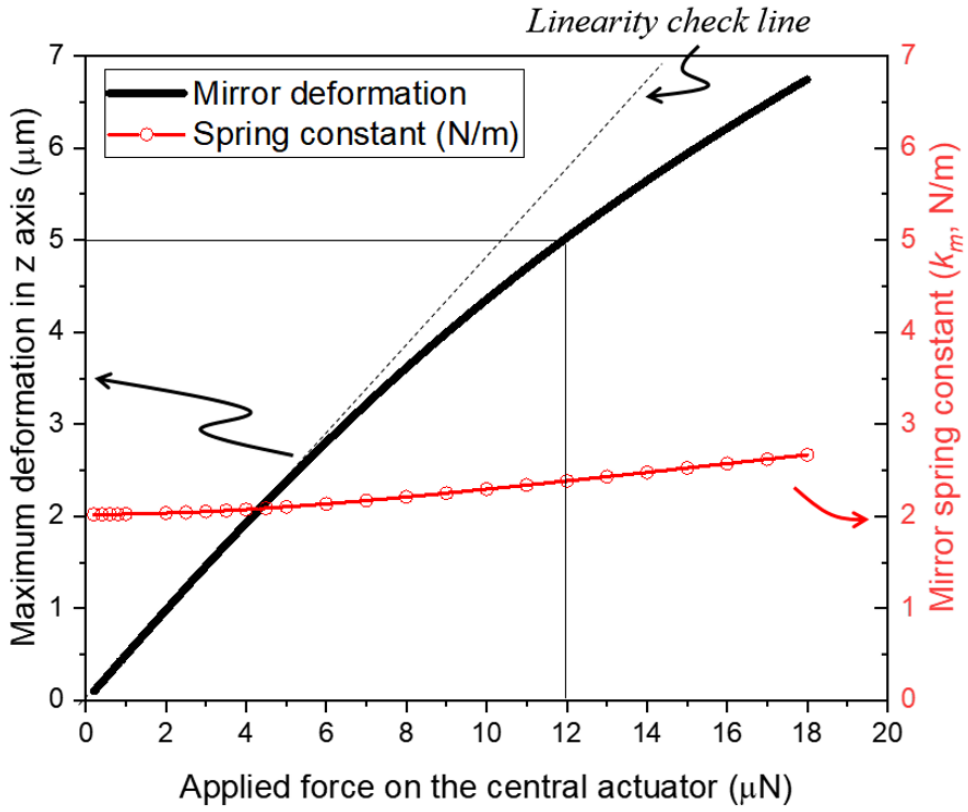

Figure 3.4: The Al/SU-8/Al mirror deformation and spring constant (k_m) as a function of applied force.

3.2.4 Resonance Frequency and Deformation Shape (STEP 2)

The resonant frequency of the Al/SU-8/Al mirror is simulated under the same boundary conditions as in Step 1. The resonance frequency of the mirror depends on the spring constant of the actuator due to the geometrical constraints of the coupled actuator array shown in Figure 3.5. The spring constant of all actuators are varied from 0 to 5 N/m. The spring constant of each actuator is defined using the spring foundation in the Solid Mechanics module of COMSOL. Figure 3.5 shows the resonance frequency of the Lorentz DM as a function of the actuator spring constant and the first resonance mode.

The simulation results show that the actuators with a spring constant of more than 1 N/m satisfy the TMT specification of an 800 Hz operational frequency (see Table 3.1).

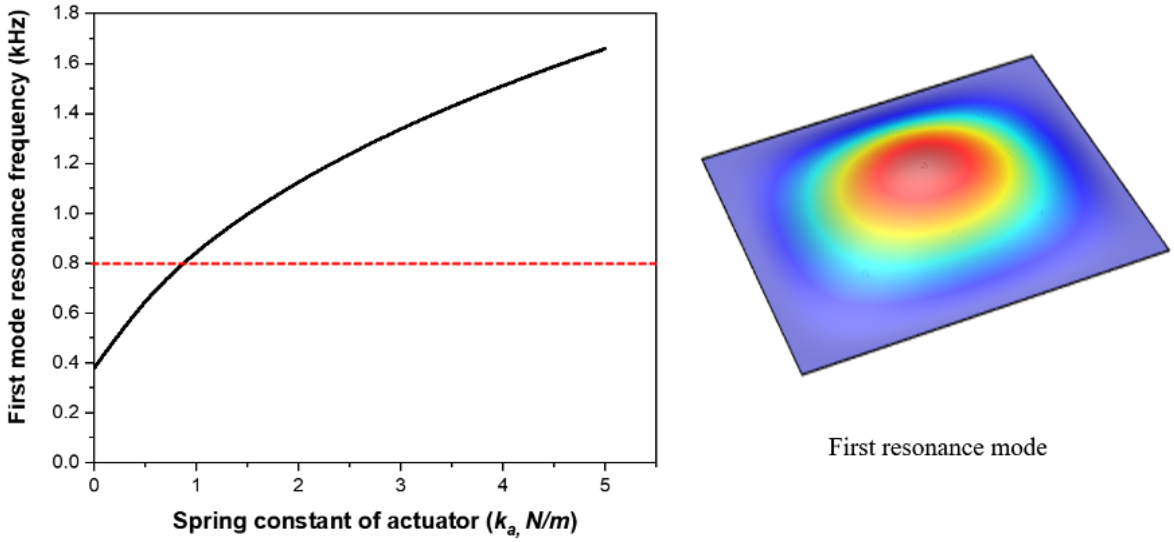

Figure 3.5: Lorentz DM resonance mode and corresponding frequency.

Figure 3.6 shows the simulated deformation shape of the 12 × 12 mm Al/SU-8/Al mirror when a force is applied from the central actuator node. To simulate the mirror deformation, the force is changed until the central actuator is deformed by 5 µm. The spring constant of all actuators was varied from 0 to clamped using the spring foundation module in COMSOL. The actuator pitch is 2 mm.

An x-axis and xy-plane cross-section of the deformed mirror with a varying actuator spring constant is shown in Figure 3.7. The mirror deflection with the clamped actuator node (k_a = clamped) is in the opposite direction of both the nearest neighbor actuators and the next in line actuators. This is because the mirror pivots on the nearest neighbor pillar. The inter-actuator coupling of the mirror is inversely proportional to the spring constant of the actuator (k_a). The mirror deformation does not cross the first actuator nodes of outside mirror until the k_a is 1.0 N/m in x-axis and 0.25 N/m in xy-plane. After then, the mirror deformation starts to spread to the external mirror surface. It can be noted that the inter-actuator coupling of the Lorentz DM can be controlled by adjusting the spring constant of the actuator array as well as the Lorentz force on the nearest actuator node.

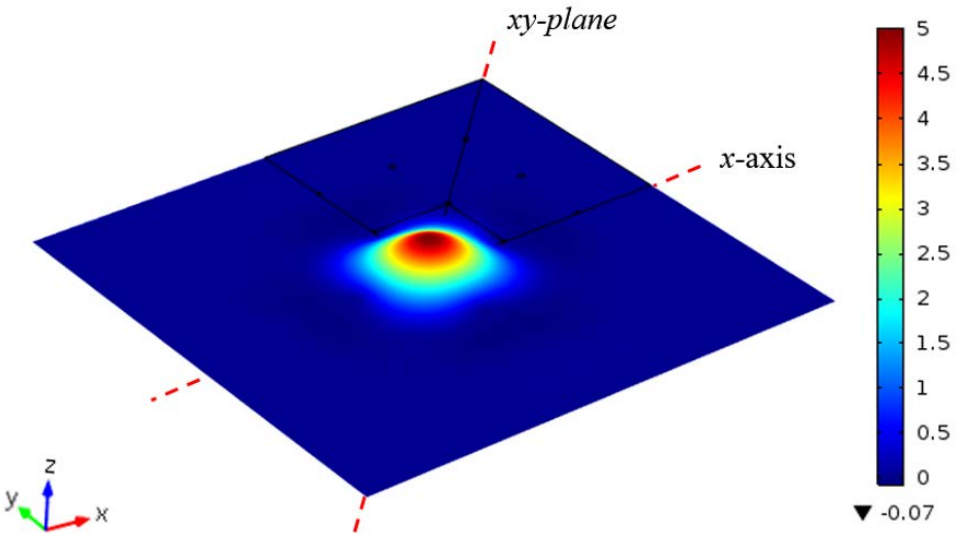

Figure 3.6: The Al/SU-8/Al deformation shape in 3D with clamped actuator geometry.

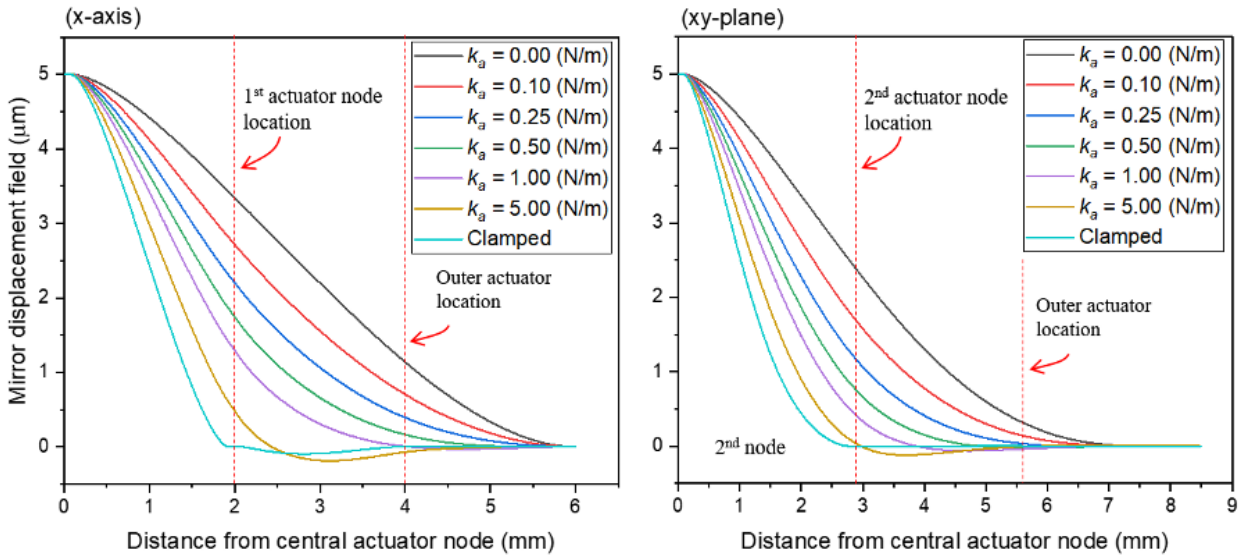

Figure 3.7: Cross-sections of Al/SU-8/Al mirror deformation in the *x*-axis (left) and the *xy*-plane (right) as a function of actuator spring constant (k_a, N/m).

3.2.5 Spring constant of the actuator (k_a) and inter-actuator coupling (STEP 3)

The resulting mirror deformation causes inter-actuator coupling between the central actuator node and the 1st and 2nd nearest actuator nodes. The inter-actuator coupling is also known as the influence

function. The magnitude of inter-actuator coupling depends on the stiffness of both the actuators and the mirror membrane.

This section defines the design criteria of the Lorentz DM. The methodology for defining these design criteria consists of calculating the spring constant of the actuator, and the force required to achieve a mirror deformation of ± 5 µm according to the Lorentz DM inter-actuator coupling. Using the calculated value of the spring constant of the mirror clamped nearest actuator nodes (k_m), the spring constant of the actuator (k_a) is calculated in Equation (3.1).

$$F_a = -\frac{k_a}{A}\left(u - u_0\right) \tag{3.1}$$

Where F_a is the force on the nearest actuator nodes, k_a is the spring constant of the nearest actuators, A is the area of the actuator node boundary, and (u-u_0) represents node boundary displacement in 3D. Table 3.4 shows the design parameters and definitions used to determine k_a.

Table 3.4: Simulation parameters and definitions for actuator spring constant (k_a) and the simulated range.

Parameter	Definition	Range
F_c	Force (µN) applied on the central actuator node	1.0 to 15 µN
k_a	Spring constant (N/m) on the nearest actuator nodes	0.1 to 5.0 N/m

The simulation results are shown in Figure 3.8. It is observed that a more rigid actuator requires more force to deform the mirror, but increases with resonant frequency. On the other hand, softer actuators reduce the operation power but have more mechanical crosstalk. According to the simulation results, the actuator with a 0.6 N/m spring constant gives 30 % inter-actuator coupling with a required force of 5.3 µN on the central actuator node in order to deform the mirror by 5 µm. In this case, the total

required force on the central actuator node is about 8.3 µN (= 5.3 µN + (0.6 N/m × 5 µm)) after adding actuators beneath the central node.

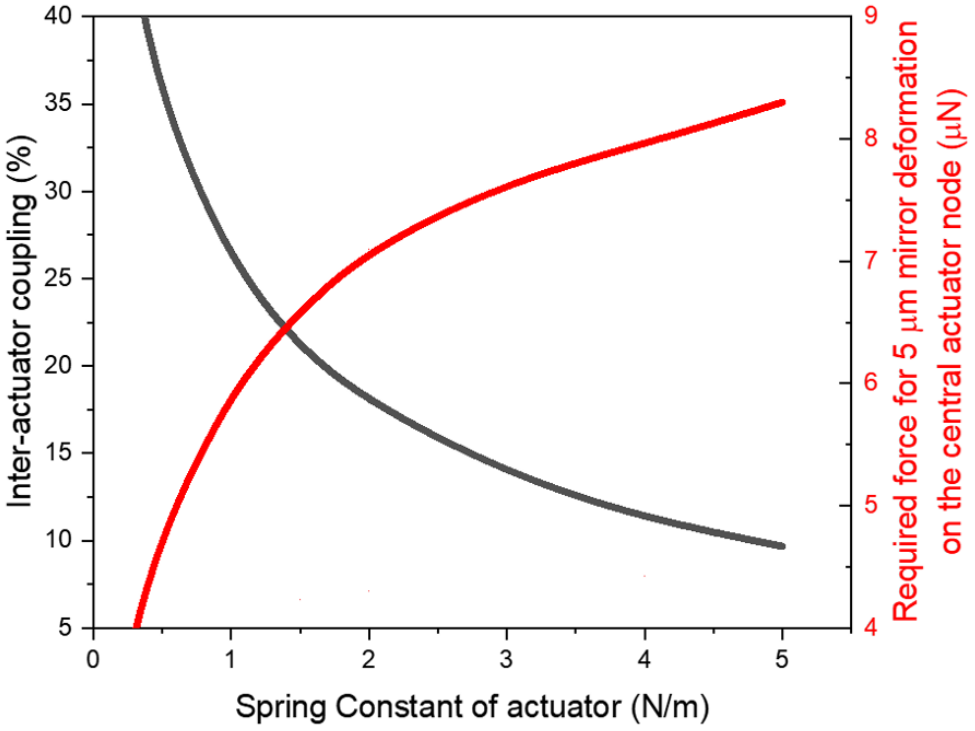

Figure 3.8: Inter-actuator coupling (crosstalk) and required force for 5 µm deformation of Al/SU-8/Al unit-cell mirror on the central node as a function of the spring constant of the actuators. This figure is used as a design criteria to define a geometry of the Lorentz DM system.

3.3 Microfabrication

The Al/SU-8/Al mirror is fabricated using various techniques at the Nano-System Fabrication Laboratory (NSFL) at the University of Manitoba. A double-sided polished <100> orientation lightly doped p-type crystalline silicon is used as the starting substrate. An important parameter to achieve during the membrane fabrication is high smoothness and planarity of the mirror surface.

The membrane fabrication begins with a 1.5 µm wet thermal SiO_2 growth on the silicon wafer, which will then be used as a mask in the subsequent KOH etch (Figure 3.9(a)). The thermal oxide layer on the backside of the silicon wafer is patterned lithographically and etched in a 10:1 BOE solution. The

exposed silicon is etched in a 30 % KOH solution at 80 °C until a 30 µm silicon membrane remains (Figure 3.9(b), Figure 3.10(b)). After the backside etch, the frontside SiO_2 is etched away in a 10:1 BOE solution.

The thick 30 µm silicon membrane is used as the base for fabrication of the mirror since its large thickness keeps it flat (unbent by stress) during the following coating steps. The 30 µm silicon membrane is coated with a tri-layer of Al/SU-8/Al. By sandwiching the SU-8 between the two Al layers, the stress is balanced, thus maintaining flatness (Figure 3.9(c), Figure 3.10(c)). A 250 nm thick Al film is deposited by thermal evaporation. SU-8-2025 (MicroChem, USA) is then spin coated on the aluminum mirror to a thickness of 4 µm to serve as the flexible membrane. To further cross-link and remove solvent from the SU-8 film, a hard bake is performed at 150 °C for 60 minutes. Following the hard bake, the second 250 nm thick aluminum layer is evaporated.

A silicon plasma etching process is used to remove the silicon membrane under the mirror. This is done in a Trion Phantom II plasma etcher. The process gas flow during plasma etching is 45 sccm CF_4 and 5 sccm O_2 at a pressure of 300 mTorr, using 145 W ICP and 100 W RIE power. The etch time is about 25 minutes. Following this, a XeF_2 gas etch is used to remove any remaining silicon residue. The XeF_2 gas is applied to the etching chamber, using multiple 90-second pulses, as needed to remove the remaining silicon. Then, a final plasma cleaning is done for ~ 1 min to the mirror surface to remove any remaining silicon composites. Process gases flows were 45 sccm CF_4 and 5 sccm O_2 at 300 mTorr pressure, using 100 W ICP and 20 W RIE power. Finally, an additional 50 nm aluminum film is evaporated to cover any undesired non-reflective regions on the membrane (Figure 3.9(d), Figure 3.10(d)). A photograph of samples fabricated by each fabrication process is shown in Figure 3.10.

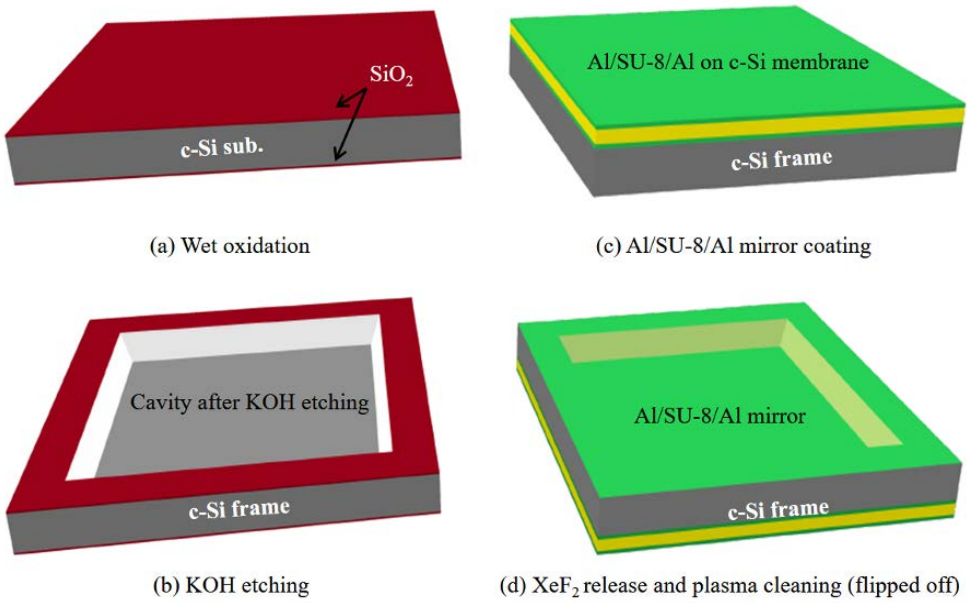

Figure 3.9: Fabrication process flow of the Al/SU-8/Al continuous deformable polymer mirror.

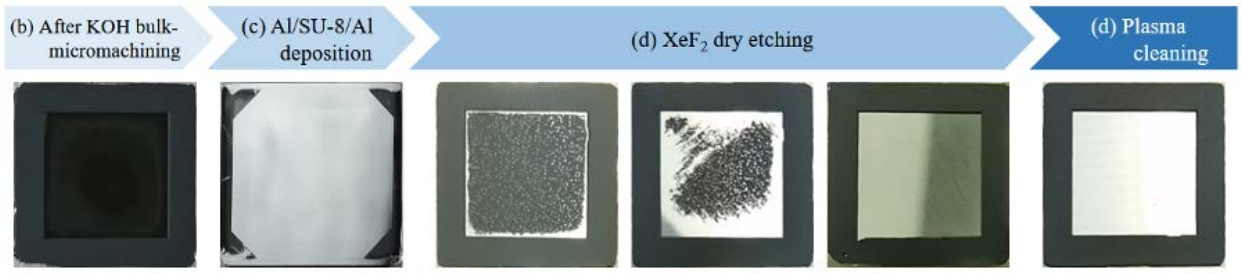

Figure 3.10: Photographs of Al/SU-8/Al mirrors following each silicon film removal process. The last photo in (d) shows a rough mirror surface.

It should be mentioned, that several trials were undertaken to develop this process. In order to remove the silicon membrane supporting the Al/SU-8/Al mirror during deposition, RIE plasma etching was used (Trion Phantom II ICP-RIE). However, the Al film surface was damaged and the mirror deformed due to ion milling and high temperatures during the plasma etching process (see Figure 3.11(a)). Therefore, plasma etching was stopped when the Al surface became visible. The remaining silicon was then removed with a XeF_2 gas etch (see Figure 3.10(d)). However, as shown in the last photo in Figure 3.10(d), the Al mirror surface was rough after the silicon was completely removed. This is because the

Si_xAl_y, SiO_x, or Al_xO_y material can be formed at the silicon interface during the Al evaporation process and not removed by XeF_2. BOE was first used to remove the possible remaining oxide. Then, the mirror failed to withstand the high density BOE liquid etching solution and was torn as shown in Figure 3.11(b). Therefore, the final plasma cleaning process was applied to remove composite material on the mirror. In addition, the mirror surface quality can be improved by growing a few nanometres of SiO_2 as a barrier before evaporating Al.

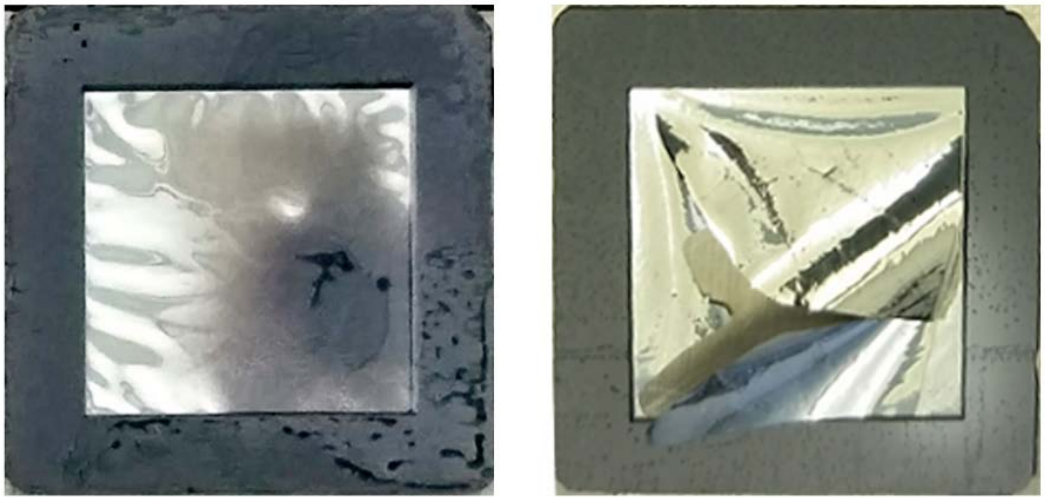

(a) A damaged mirror by Plasma (b) A torn mirror by the high density BOE

Figure 3.11: (a) Photograph of a damaged Al/SU-8/Al mirror by high plasma energy. (b) Ripped mirror by the liquid BOE solution.

3.3.1 Mirror Topology

The surface profile of the fabricated Al/SU-8/Al membrane mirror was carefully measured using a Fogale Photomap 3D optical profiler (Figure 3.12(b)). The mirror topology was compared with a polished silicon wafer (Figure 3.12(a)). The RMS roughness of the Al/SU-8/Al mirror was observed to be 6.5 nm, which is close to the 5.6 nm surface roughness of polished silicon wafer. This observation indicates that the polished smooth silicon surface was properly transferred to the membrane mirror. Furthermore, the mirror is mechanically robust. The mirror did not tear when a stack of hexagonal nuts with a combined mass of 21 g was stacked on top of it (see Figure 3.13).

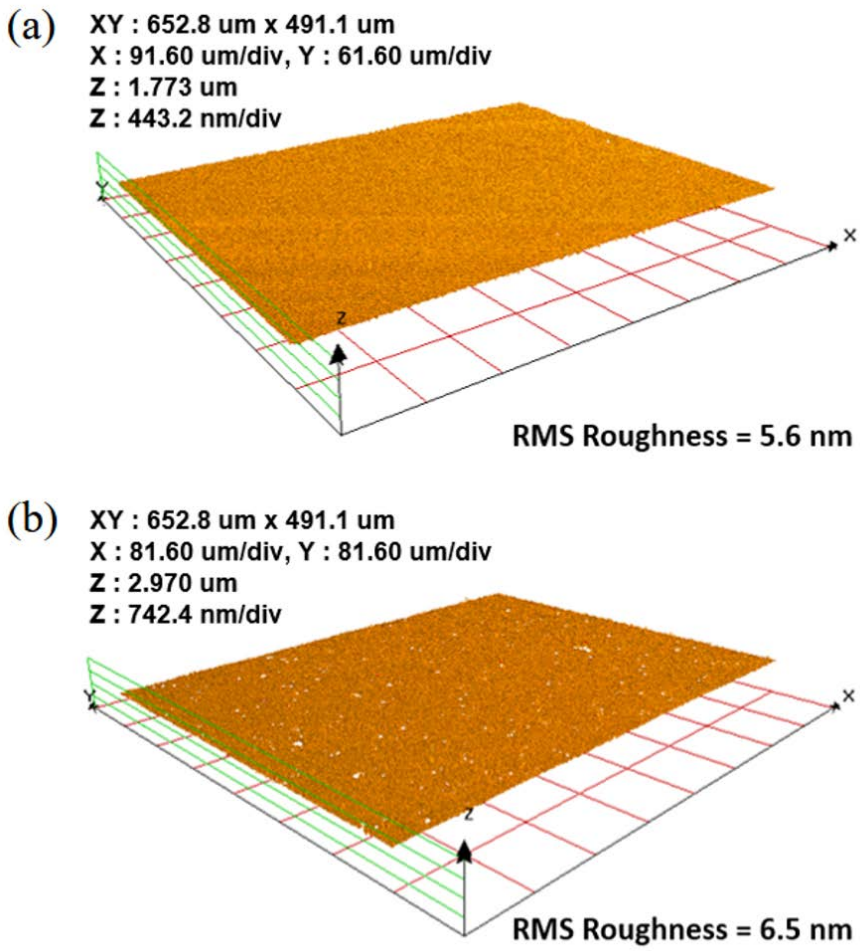

Figure 3.12: (a) The topography of polished silicon wafer. (b) The topography of the Al/SU-8/Al mirror.

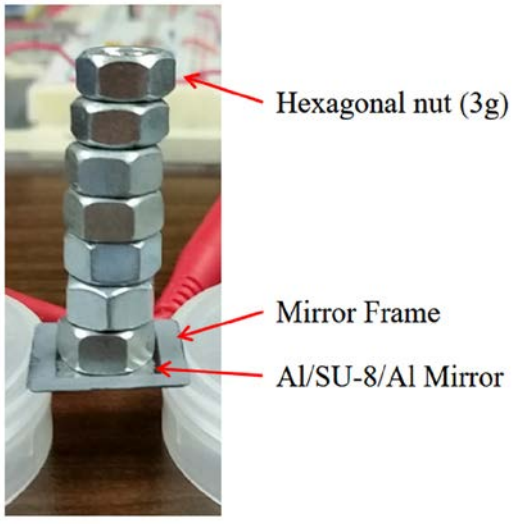

Figure 3.13: Photograph of testing the mechanical strength of an Al/SU-8/Al mirror. Each nut is 3g.

3.4 Chapter Summary

The design and fabrication process of the epoxy (SU-8) based continuous deformable polymer mirror was accomplished. The FEM simulation results show that the first mode resonance frequency of the Lorentz DM is over 800 Hz at over 1 N/m spring constant of the Lorentz actuator, which satisfies the AO specification for TMT as shown in Table 3.1. The spring constant of the Lorentz actuator can be determined according to an inter-actuator coupling range from 10 to 30 %. The computed maximum stress with a 5 μm deformation is 6.1 MPa, which is less than 5 % of the yield strength of the SU-8 (137 MPa) and aluminum (124 MPa) films. The FEM simulation results of the Al/SU-8/Al mirror were also required in order to design the Lorentz actuators. This will be covered in Chapter 4.

4

Actuator Design and Simulation

Contents

4.1 Introduction

The primary goal of this chapter is to develop a new design of MEMS-based Lorentz actuator with low operational voltage and current, which meets the design criteria of the Lorentz DM developed in Chapter 3. The most significant advantage of the Lorentz actuator is that since it can move up and down (bidirectional motion), it only needs to move half the distance in comparison to an electrostatic actuator, which can only move downward. Additionally, undesirable mirror deformation induced by gravity and/or film stress can be corrected since this Lorentz actuator can have bi-directional motion. Also, the total power dissipation in the Lorentz actuator at the same actuator pitch is approximately less than half of that of an electrostatic actuator DM. The actuator is designed to meet the Lorentz DM design criteria investigated in Chapter 3 to ensure that the actuator would be able to operate with telescopes such as the TMT.

4.1.1 Lorentz Actuator

The novel structural simplicity of the MEMS Lorentz actuator enhances fabrication yield compared to electromagnetic coil actuators and electrostatic actuators for DM applications. The Lorentz force can be calculated by using Equation (4.1) relating the magnetic field ($\vec{B}$), current ($\vec{i}$), and wire length (l) of the conductor [37]. The directional relationship between the force, current, and magnetic field flux is shown in Figure 4.1(a).

$$\vec{F} = \vec{B} \times \vec{i}L \tag{4.1}$$

The first MEMS Lorentz actuator is introduced by Ko et al. in 2002 [54]. This laterally driven Lorentz actuator had a single leaf spring structure with 1.2 μm width × 16 μm thickness × 920 μm length (see Figure 4.1(b)). The single leaf spring consisted of a heavily doped n-type polysilicon fabricated using standard semiconductor fabrication techniques. A 60 μm large lateral deflection at the center was reported

at a current of 566 mA. Moreover, the leaf spring was mechanically robust, as demonstrated by the 1 m height free drop test on a cement floor.

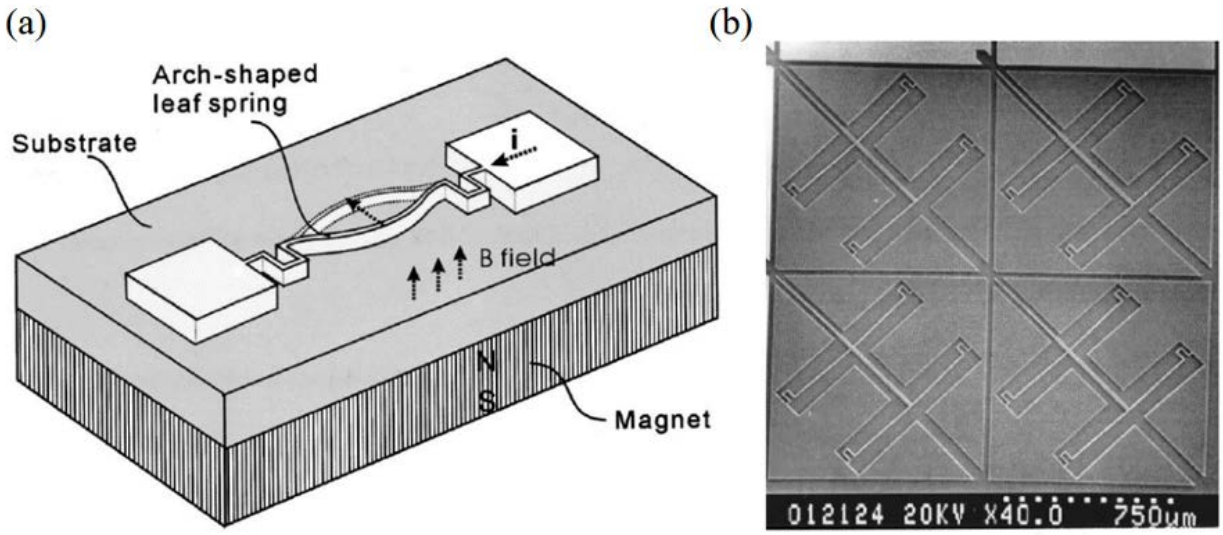

Reproduced from [Ko, J. S., Lee, M. L., Lee, D.-S., Choi, C. A., & Tae Kim, Y., Development and application of a laterally driven electromagnetic microactuator. Applied Physics Letters, 81(3), pp. 547–549, 2002. https://doi.org/10.1063/1.1494462], with the permission of AIP Publishing.

Figure 4.1: (a) Working principle of the laterally driven Lorentz actuator, (b) SEM image of the fabricated optical switch [55].

Then, Lv et al. published work on a laterally displaced serpentine structure Lorentz actuator in 2014 [22]. A 1 µm thick Al serpentine structure was deposited and patterned (see Figure 4.2). The backside silicon substrate was removed to release the device using the deep reactive ion etch (DRIE) technique. Due to the easy manufacturing process for a simple structure, a fabrication yield of nearly 100 % was reported. The lateral displacement reported in the paper was more than 55 µm at a driving current of 7 mA with a magnetic field of 0.14 Tesla. The resonant frequency of the actuator was approximately 1.2 kHz. The vertical deflection can be easily achieved by changing the orientation of the permanent magnet's magnetic field.

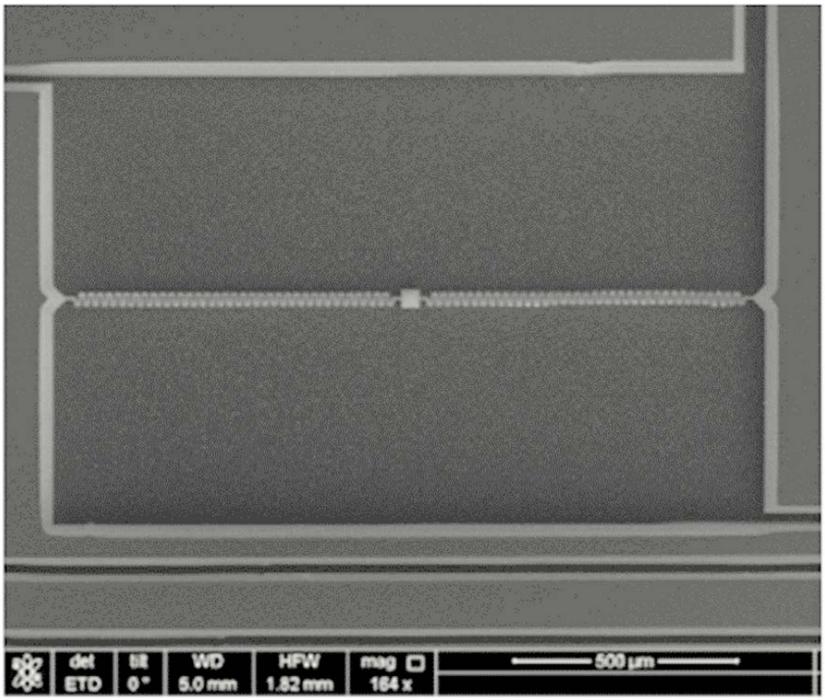

Figure 4.2: SEM image of the laterally driven Lorentz actuator [22].

However, this Lorentz actuator has critical drawbacks when applied to DM. First, a thin and long metallic serpentine structure is too soft to deform the rigid membrane. Here, the spring constant of the serpentine structure is about 0.18 N/m and is calculated using Equation (4.2) [37]

$$k = \frac{\vec{B} \times \vec{i}\vec{L}}{d}, \tag{4.2}$$

where, k is spring constant (N/m), and d is maximum deflection magnitude. This spring constant is about ten times smaller than even for the very soft polymer membrane case (~ 2 N/m for 2000 µm square SU-8 membrane). As a result, the DM system employing this Lorentz actuator can have several disadvantages. First, the DM system can have high mechanical crosstalk between the nearest actuator positions. Second, the generated Lorentz force deflects a soft serpentine structure rather than deforming the membrane. Thus,

a membrane surface could have undesired serpentine marks that cause diffraction of light. Lastly, the long and thin serpentine structure increases the electrical resistance, resulting in a temperature increase by Joule heating. Therefore, the device could be thermally stressed and show non-linear deformation. In this chapter, the drawbacks of the previously researched MEMS-based Lorentz actuators are mitigated by applying the long and rigid crossbar, and the flexible spring support structure.

4.2 Common Design Concept of the Lorentz Actuator

The working principle of the horseshoe-shaped Lorentz actuator for the low voltage Lorentz DM is shown in Figure 4.3. The generated Lorentz force on the crossbar is a cross product of the magnetic field ($\vec{B}$) and current ($\vec{i}$) and crossbar length (l) as shown in Equation (4.1). The bi-directional motion of the actuator and mirror can be enabled by changing the direction of current on the crossbar. Thus, a 10 µm mirror deformation can be achieved with only a ± 5 µm motion, thereby requiring lower actuation current.

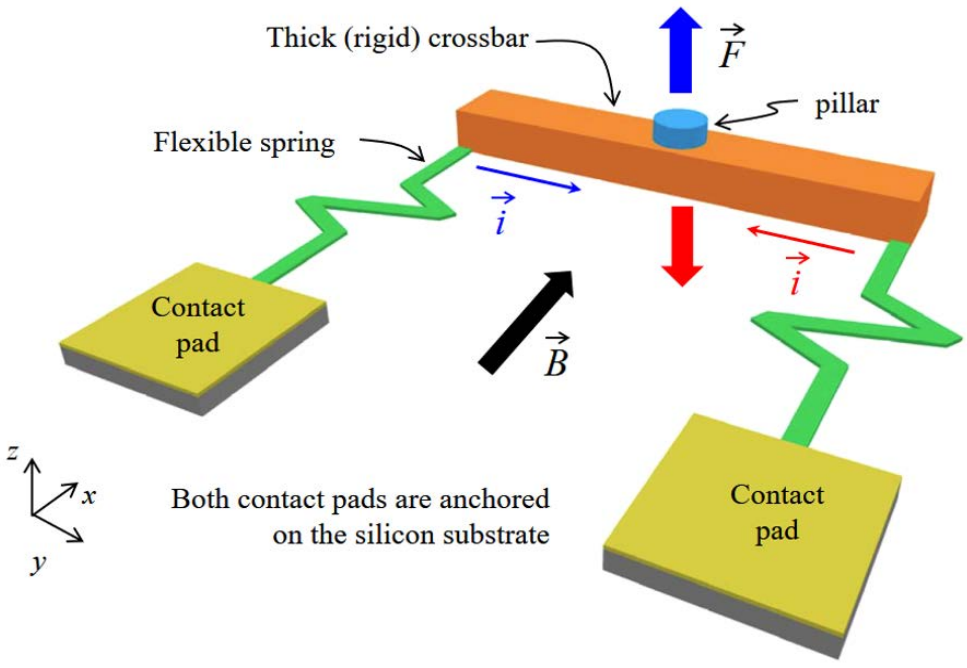

Figure 4.3: Illustration of a common Lorentz force actuator design and its force relationship.

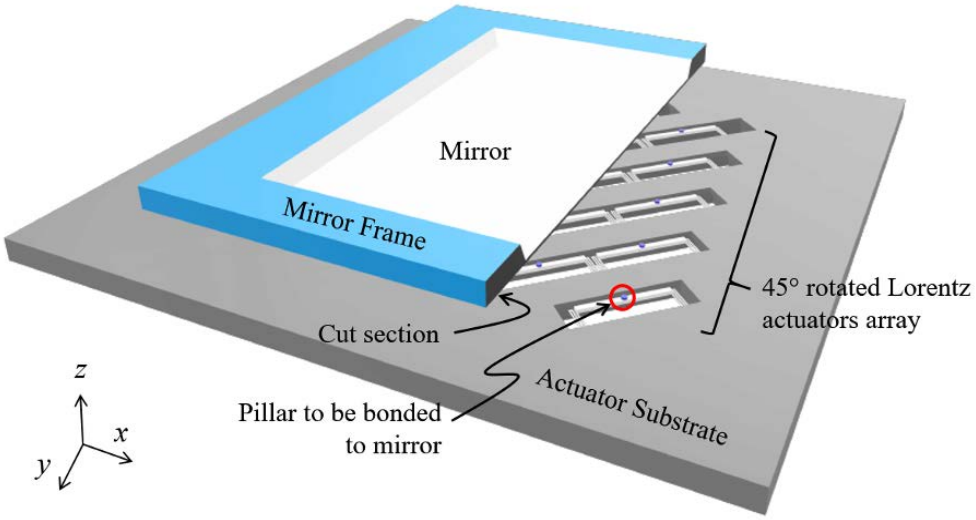

Figure 4.4: Illustration of a 5 × 5 array of a Lorentz actuator below the Al/SU-8/Al mirror.

The Lorentz actuator is comprised of flexible springs on either end of a central thick and rigid crossbar above a permanent magnet (see Figure 4.3). The springs support the crossbar and are flexible enough to allow for vertical movement of the crossbar by the generated Lorentz force. The geometry of the springs can be in the form of a cantilever arm or a serpentine spring. This depends on the thickness and rigidity of the constituent material, as well as the required stroke of the actuator. The total length and cross-sectional area of the spring will be optimized in both cantilever arms and serpentine designs.

The crossbar is an essential element necessary for generating a Lorentz force. Longer crossbars can produce larger Lorentz forces when the magnetic field is fixed. However, long crossbars can be bent while the actuator pushes or pulls the membrane due to its low stiffness. Thus, the crossbar should be designed to be thick (rigid) enough to limit its own bending when it applies a force to the above membrane.

In the centre of the crossbar, a pillar can be fabricated. The height of the pillar is at least half of the maximum deformation of the mirror, and the crossbar will bend under a load during the mirror actuation. The role of the pillar is to prevent the crossbar from touching the mirror with the edges of the crossbar. Finally, the actuator is bonded to the Al/SU-8/Al mirror at an angle of 45° to maximize the

Lorentz force on the crossbar (see Figure 4.4). Metal fusion, adhesive, or/and anodic bonding techniques are applicable for the bonding process, which is described in Chapter 7.

4.3 Cantilever Arm Lorentz Actuator

The detailed geometry and working principle of the cantilever arms Lorentz actuator fabricated by surface micromachining and electroplating is shown in Figure 4.5. The actuator is comprised of cantilever arms on both ends of a thick crossbar. The cantilever arms consist of a Cu/Cr/Cu multi-layered thin film. The material properties of Cu and Cr used in this design are shown in Table 4.1. This multi-layered structure applies stress in the thin cantilever arms to curl the supporting cantilevers upwards in the z-axis initially. The initial vertical deflection of these two supporting cantilevers will provide adequate space for the crossbar to have a downward (pull-down) motion. In addition, the initial deflection of the supporting cantilevers will bring the crossbar into contact with the mirror, which facilitates the bonding of the actuator to the mirror surface.

The long and thick (rigid) conducting crossbar is formed by electroplating on a thin Cu/Cr/Cu multilayered film. In the centre of the crossbar, the pillar can also be fabricated by electroplating. The height of the pillar is more than half (5 μm) of the maximum deformation (10 μm) of the mirror to prevent the crossbar from touching the mirror with the edges of the crossbar.

Table 4.1: Material properties of the cantilever arm Lorentz actuator modeling and simulation.

Material Properties	**Cu**	**Cr**
Density (kg/m^3)	8960	7150
Young's Modulus (GPa)	120	140 [56]
Poisson's Ratio	0.34	0.21
Thermal Conductivity (W/m·K)	401	93.7
Heat Capacity at Constant Pressure (J/(kg·K))	384	448.0
Coefficient of Thermal Expansion, CTE (μm/K)	16.5	4.9
Electrical conductivity (× 10^6 S/m)	51.8	7.9

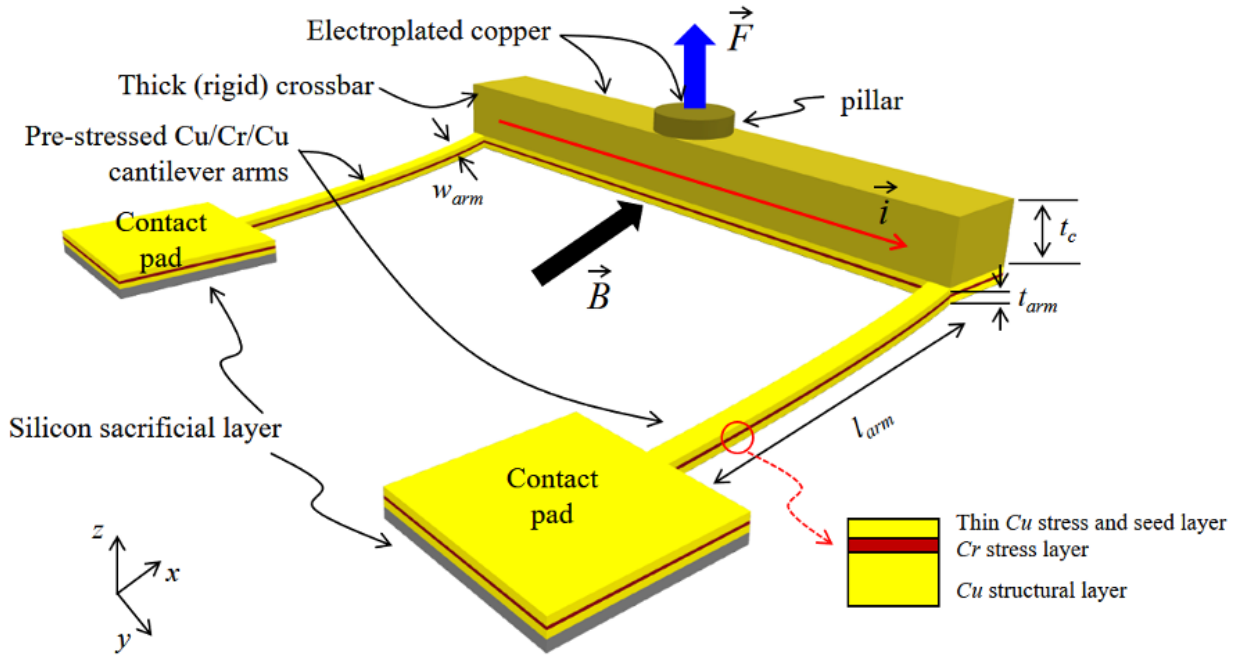

Figure 4.5: Illustration of the geometry and force relationship of the surface micromachined Lorentz force actuator design.

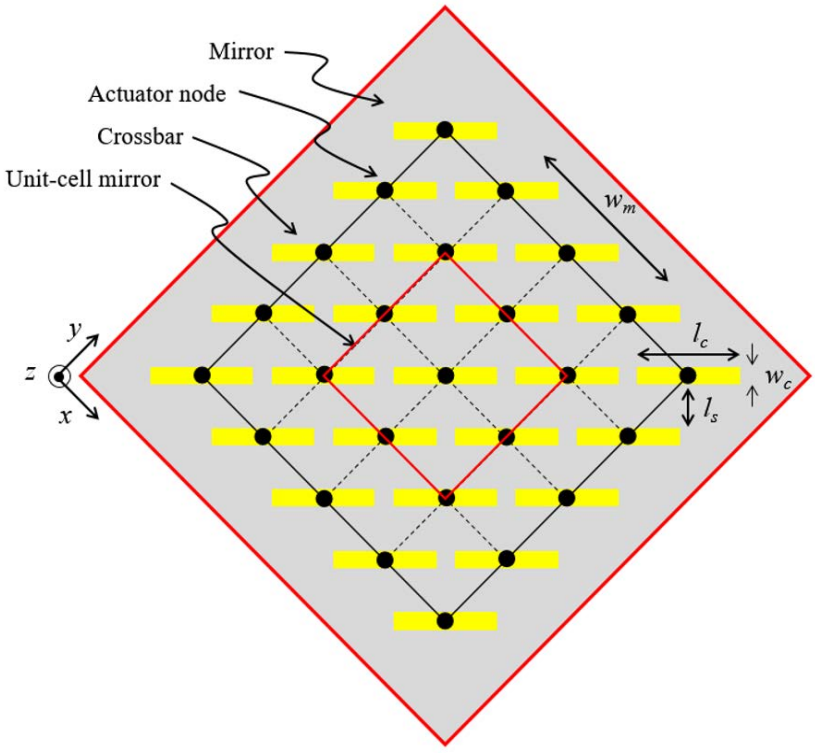

Figure 4.6: Schematic of the Lorentz actuator array with the mirror.

4.3.1 Crossbar Geometry

The geometry of the cantilever arms Lorentz actuator array is illustrated in Figure 4.6. The crossbar length (l_c) should be less than $2\sqrt{2}$ mm, which is the diagonal length of a unit cell mirror. Accordingly, the maximum length of each cantilever arm can be 2 mm.

The crossbar should be designed to be rigid enough to transmit the generated Lorentz force to the pillar with minimal loss due to crossbar bending. The crossbar can be approximated as a cantilever structure clamped by a pillar. Then, the cantilever thickness can be approximated by Equation (4.3). In this equation, the deflection height (d_z) of the crossbar is a function of the applied force at the end (F_z), half length (l_c), Young's modulus (E), and moments of inertia (I). The I is defined by the width (w_c) and thickness (t_c) of the crossbar due to its rectangular cross-section [86]:

$$d_z = \left(\frac{F_z l_c^3}{3EI} \right), \quad \text{and} \quad I = \frac{w_c t_c^3}{12} \quad \text{(moments of inertia).} \tag{4.3}$$

Therefore, the required cantilever thickness can be written as:

$$t_c = \left(\frac{4F_z l_c^3}{E w_c d_c} \right)^{1/3} \tag{4.4}$$

As discussed in Chapter 3, if the Lorentz DM inter-actuator coupling is fixed at 10 %, the spring constant of the actuator is 4.9 N/m and the maximum force (F_z) required for ± 5 μm unit-cell mirror deformation is 32.9 μN. The crossbar deflection (d_z) is allowed to be 10 % (0.5 μm) for at the maximum allowable force (F_z). The crossbar dimension is set to 1800 μm (l_c) × 150 μm (w_c). Therefore, t_c can be calculated as follows as shown in Equation (4.5). The calculated desirable crossbar thickness (t_c) is 22 μm. The thickness of such thick *Cu* can be achieved by an electroplating technique:

$$t_c = \left(\frac{4 \times 32.9\mu N \times (900\mu m)^3}{120GPa \times 150\mu m \times 0.5\mu m} \right)^{1/3} = 22\mu m. \tag{4.5}$$

4.3.2 Cantilever Arm Geometry

The dimensions of the cantilever arms can be determined by the spring constant (k_a) defined by the inter-actuator coupling of the Lorentz DM in Chapter 3. The required spring constant for 10 to 30 % inter-actuator coupling of the Lorentz DM is 4.9 N/m to 0.6 N/m, respectively (see Figure 3.8). The k_a is calculated using Hooke's law, which is proportional to the force (F_z) and inversely proportional to the displacement (d_z) in the z-axis as shown in Equation (4.6). The cantilever arms (see Figure 4.5) can be approximated as a fixed-free beam under point loading at the free end (crossbar). Therefore, Equation (4.3) is still valid for defining the geometry of the cantilever arms. Then, the geometrical dependence of the spring constant of the cantilever arms can be determined by Equation (4.7), which is calculated by substituting d_z in Equation (4.3) into Equation (4.6). Here, the total spring constant is 2 *ka* since the two cantilever arms are connected in parallel to the crossbar.

The thickness of each Cu (bottom), Cr, and Cu (top) layer was defined to be 700 nm, 100 nm and 200 nm respectively. These are the thicknesses necessary in order to facilitate fabrication and utilize initial curl-up which will be explained in the next section. The Young's modulus of the cantilever arms was assumed to be 120 GPa for Cu since it is close to Cr (140 GPa), and Cu is 9 times thicker than Cr. The length of a cantilever arm (l_{arm}) was fixed to 100 μm [86]:

$$k_a = \frac{F_z}{d_z} \tag{4.6}$$

$$k_a = \frac{E w_{arm} t_{arm}^3}{4 l_{arm}^3} \tag{4.7}$$

Figure 4.7 shows the geometrical dependence of the spring constant of the actuator ($2k_a$) as a function of the width (w_{arm}) and thickness (t_{arm}) of the cantilever arm. From this figure, the applicable w_{arm} and t_{arm} combination with 100 μm and 200 μm cantilever arm (l_{arm}) lengths at 10 to 30 % inter-actuator coupling can be selected in the red-bordered area.

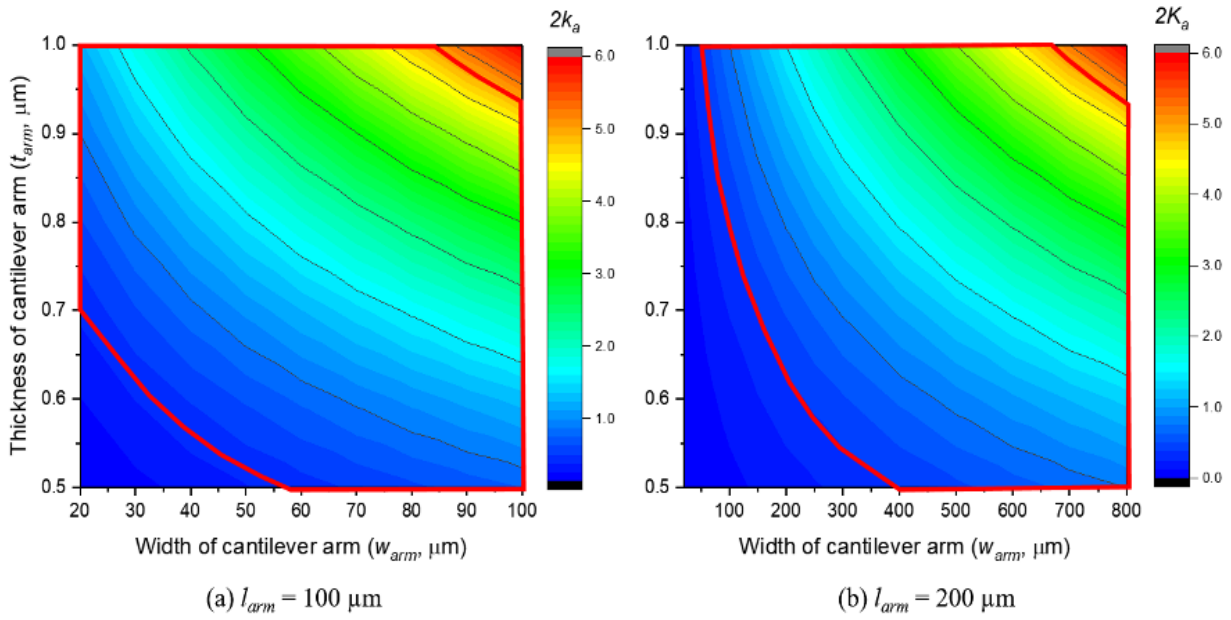

Figure 4.7: Geometrical dependence of the total spring constant of the actuator ($2k_a$) with (a) 100 µm and (b) 200 µm lengths of the cantilever arm. The red-bordered area shows the combination of thickness and width of the cantilever arm for 10 to 30 % inter-actuator coupling of the Lorentz DM.

4.3.3 Pre-stressed Cantilever Arms

The stress in the multi-layered Cu/Cr/Cu films of the cantilever arms enables initial curl-up of the actuator. In order to determine the initial z-axis displacement, it is necessary to know the stress in each film. Thus, the stress of each Cu and Cr film and multilayered Cu/Cr/Cu films are determined based on experiment and simulation.

The film stress developed during sputter deposition is mainly due to intrinsic and extrinsic stresses. The intrinsic stress is caused by impurities, lattice mismatch from dislocated atoms, and lattice expansion or contraction during grain growth. The extrinsic stress is caused by CTE (Coefficient of Thermal Expansion) mismatch between the deposited film and substrate. The wafer is cooled down after deposition, but the film and the substrate are contracted at different speeds due to CTE mismatch. As a result, the intrinsic stress of the wafer is increased. Finally, the wafer bends up or down dependent on

whether the final stress is positive or negative to accommodate these additional stress effects, and reaches a steady state as shown in Figure 4.8.

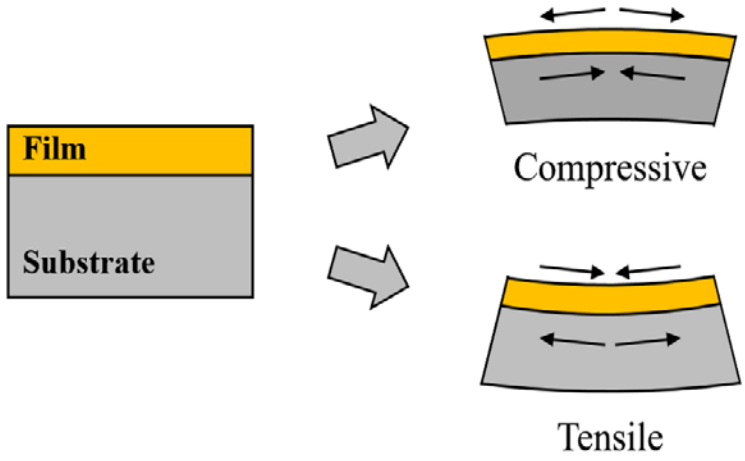

Figure 4.8: Film bow due to intrinsic stress from CTE mismatch. The curvature corresponding to the film stress is tensile (positive) or compressive (negative).

4.3.3.1 Thin Film Stress of Cu

The thin film stress of Cu and Cr film on a 3" <100> orientation silicon substrate is reported in the Nano Systems Fabrication Laboratory (NSFL) internal research report [58]. The Cu and Cr films used in this experiment were prepared by Semicore's MRC 8667 RF/DC/RF bias three target sputtering system in the NSFL. The stress levels of each film were obtained from the Toho FLX-2320 thin film stress measurement system at room temperature after cooling down the wafer. In order to facilitate characterization and fabrication of the actuator, the total thickness of the Cu/Cr/Cu multilayered cantilever arms was fixed at 1 μm. The bottom Cu film was used as a structural layer at the bottom, and the additional stress layer and seed layer for electroplating on top of the cantilever arm. In this structure, the difference between the film stress of each layer should be substantial to obtain a more pronounced cantilever deflection. Therefore, the film stress of the Cu structural layer should be minimized, and the Cr stress layer should be deposited under high-stress conditions.

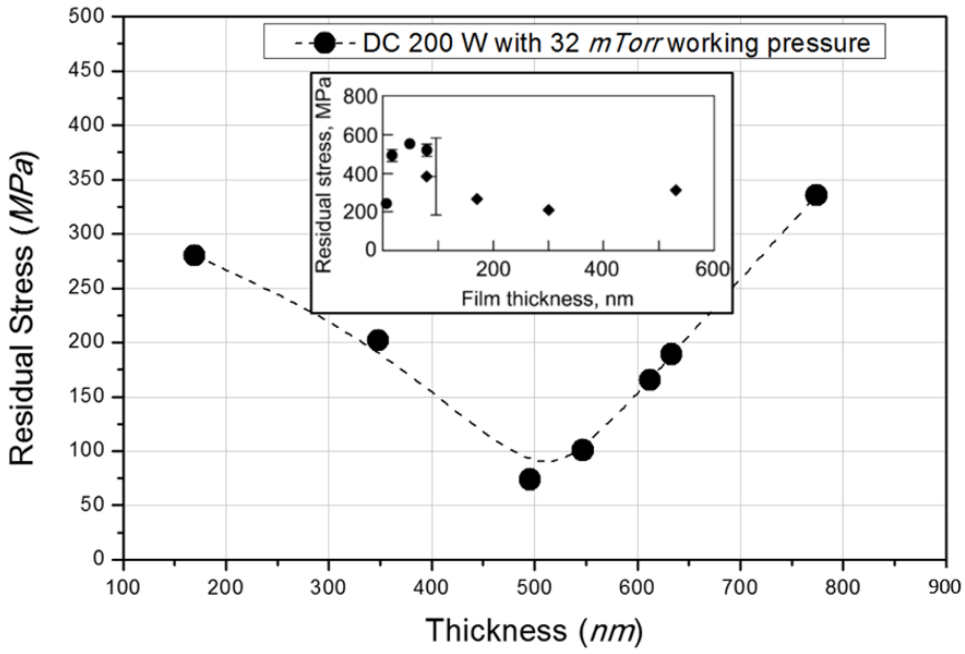

Rectangular shape inset: Reproduced from [Hanabusa, T., Kusaka, K., & Sakata, O., Residual stress and thermal stress observation in thin copper films. *Thin Solid Films*, Vol. 459(1–2), pp. 245–248, 2004. https://doi.org/10.1016/j.tsf.2003.12.102], with the permission of Elsevier.

Figure 4.9: The film stress of sputter deposited Cu as a function of film thickness. The rectangular shape inlet shows a similar result achieved from reference [58].

The Cu film used in this experiment was prepared at a maximum Ar pressure of 32 mTorr in an MRC 8667 sputtering system since the low film stress Cu was obtained at a high Ar deposition pressure in reference [57]. The film stress in sputter deposited Cu films always shows a tensile profile regardless of film thickness as shown in Figure 4.9. These experimental results are in good agreement with the paper reported by Hanabusa, which is shown in the rectangular shape inset in Figure 4.9. The residual stress of a deposited Cu film decreases steadily from 270 MPa at 50 nm thick to 70 MPa at 500 nm thick. Afterward, the film tends to increase the stress as the film thickens up to 800 nm. The stress relaxation mechanism in films thinner than 500 nm was explained by Hanabusa's paper. According to the paper, the compressive stresses developed during the cooling stage will force the atoms through the grain boundaries and the film surface. The atomic migration forms hillocks at the grain boundaries on the film surface and reduces the

stress. From this experiment, the lowest stress on the Cu film was 70 MPa and was obtained at a thickness of 500 nm.

4.3.3.2 Thin Film Stress of Cr

The amount of initial curl-up displacement of the cantilever arm is mainly defined by the stress of the Cr film. The film stress was observed to be proportional to the film thickness according to the stress measurement results from the NSFL and was in accordance with the results in S. Yu Grachev's paper [59] as shown in Figure 4.10. This phenomenon occurs because as the film thickens (t_f), the microstructure of the film becomes dense, and therefore, the amount of film expansion decreases. The correlation between the film thickness and the stress can be found in the Stoney equation in Equation (4.8) [60]. According to this formula, the stress of the film is inversely proportional to the film thickness:

$$\sigma_a = \frac{E_s t_s^2}{6t_f} \times \frac{1}{R}, \tag{4.8}$$

Here, σ_a is the average stress in the plane of the film, E_s is the biaxial elastic modulus of the substrate, t_s is the substrate thickness, t_f is the film thickness, and 1/R is the system curvature. According to reference [57], the thinner the Cr, the higher the film stress. Therefore, the thickness of Cr was chosen to 100 nm, which had a high film stress.

The stress of the Cr film deposited at 200 W DC power decreased as the Ar working pressure increased at the same film thickness. In [59], the stress in the Cr film should be proportional to the grain boundary density and inversely proportional to the grain width. The grain width in the sputter deposited Cr film was observed to rise with increasing the Ar pressure. The grain width is indicated by a hollow red triangle in Figure 4.10. The trend of sputtered Cr film stress corresponds to Grachev's paper.

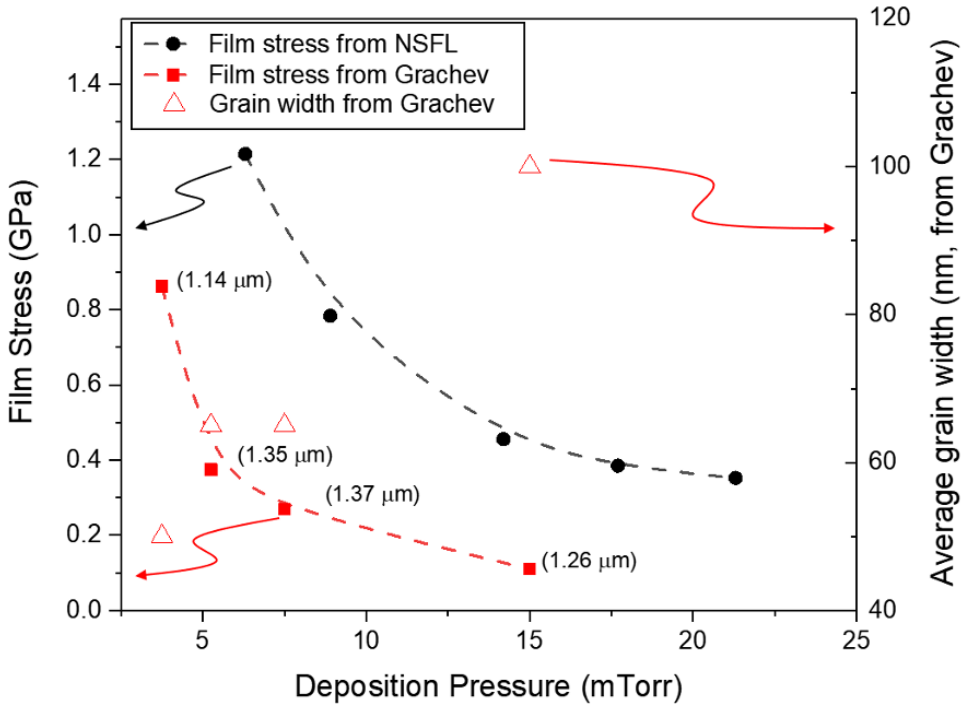

Red colored: Reproduced from [Grachev, S. Y., Tichelaar, F. D., & Janssen, G. C. A. M., Stress in sputter-deposited Cr films: Influence of Ar pressure. *Journal of Applied Physics*, Vol. 97(7), pp. 073508, 2005. https://doi.org/10.1063/1.1876579], with the permission of AIP Publishing.

Figure 4.10: The changes of film stress of the 100 nm thick Cr deposited by sputtering at 200 W DC as a function of Ar working pressure compared with reference [59].

4.3.3.3 Initial curl-up displacement

The z-axis initial curl-up displacement of the actuator was simulated using COMSOL Multiphysics software by applying film stress on the top Cu and the Cr. The film stress of each top Cu and Cr layer with respect to the thickness and the deposition condition is biaxial stress. It is biaxial stress due to a 2D confined film structure. Thus, it is only applied to the *xy* plane in COMSOL. The amount of initial curl-up displacement has to be greater than 10 μm to obtain a ± 5 μm bi-directional Al/SU-8/Al mirror deformation. The total thickness of the Cu/Cr/Cu multilayers was fixed at 1 μm. The thickness of the top Cu seed layer was fixed at 200 nm for stable electrodeposition as reported in the NSFL internal report [61]. The thickness of the Cr stress layer, which plays the primary role in the initial displacement of

the actuator, was set at 100 nm. Accordingly, the thickness of the bottom Cu layer becomes 700 nm to make the total cantilever arm thickness to be 1 µm. This thickness allows for sufficiently low film stress (250 MPa) compared to Cr (800 MPa at 100 nm with 200 W power and ~ 9 mTorr Ar deposition condition). The structural parameters, definitions and simulation range, and film stress are given in Table 4.2. The material properties used in the simulation are shown in Table 4.1.

Figure 4.11 shows the simulated average curl-up displacement on the crossbar for various lengths and widths of the cantilever arm. We can see that the stress-induced cantilever arm displacement increases with its length and width. Further, it can be noted that the minimum requirement of over 5 µm displacement in the actuator design was satisfied in all combinations within the simulation range.

Table 4.2: Simulation parameters, definitions, and the simulated range for initial curl-up displacement of the cantilever arm Lorentz actuator design.

Parameter	Definition	Range
w_c	Crossbar width	150 µm
t_c	Crossbar thickness	20 µm
w_{arm}	Cantilever arm width	40 to 140 µm
l_{arm}	Cantilever arm length	100, 150, 200 µm
t_{tcu_arm}	Seed *Cu* thickness	200 nm
t_{cr_arm}	*Cr* stress layer thickness	100 nm
t_{bcu_arm}	*Cu* structural layer thickness	700 nm
Sigma_Cr	Film stress of 100 nm thick *Cr* layer deposited at DC 200 W and 8.9 mTorr.	800 MPa
Sigma_Cu	Film stress of 200 nm thick *seed-Cu* layer deposited at DC 200 W and 32 mTorr *Ar* pressure	250 MPa

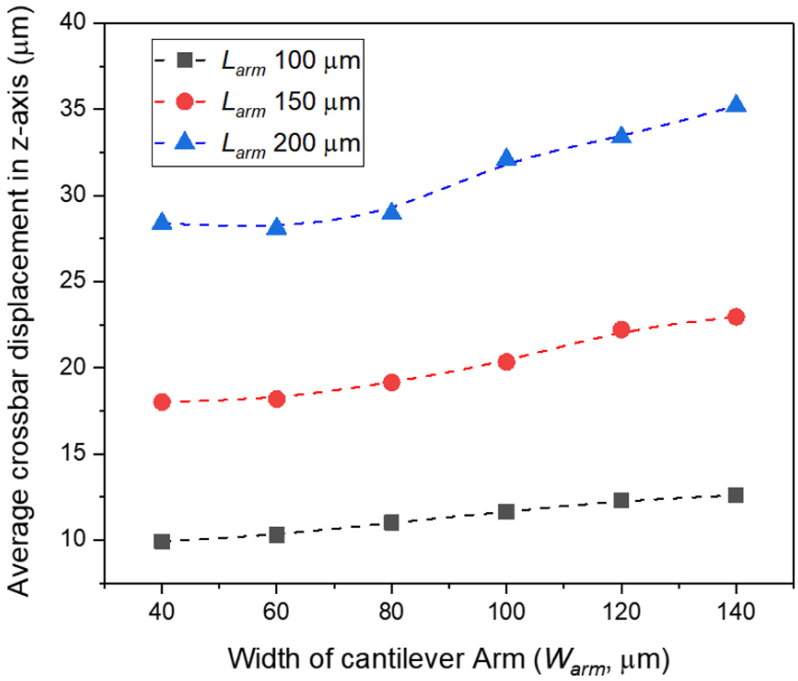

Figure 4.11: The average crossbar displacement by film stress in z-axis as a function of the width of cantilever arm (W_{arm}) and length (L_{arm}). Each film stress value is fixed at 800 MPa and 250 MPa for Cr and seed-Cu respectively (COMSOL simulation result).

4.3.4 Lorentz Actuation

The maximum required current that deforms the unit-cell of the Al/SU-8/Al mirror by ± 5 µm can be obtained using Equation (4.3) with a defined crossbar length of 1800 µm. For example, the Lorentz DM with 30 % crosstalk requires an 8.3 µN force to achieve 5 µm mirror deformation. Therefore, the total required current in a 0.48 Tesla magnetic field is around 10 mA (= 8.3 µN / (0.48 Tesla × 1800 µm)). From Equation (4.7), the stiffness of the actuator is inversely proportional to the cantilever arm length and directly proportional to the cantilever arm thickness. The high stiffness and Cantilever arm Lorentz actuator require a high operational current. As a result, the power consumption of the DM system increases, and controlling the DM system becomes more difficult due to the variation of the material properties by Joule heating. Therefore, the thermal effects on the device as a function of current is discussed in the following section.

4.3.5 Thermal Effect

Joule heating is a significant problem in all electronic devices since it makes it difficult to predict the device characteristics by changing the mechanical properties. Notably, Lorentz force based DMs controlled by current are more sensitive to thermal issues than electrostatic DMs controlled by voltage. The heat generated by the Joule heating mechanism affects the Lorentz actuator and the Al/SU-8/Al mirror in various ways.

One of the significant effects of Joule heating is the change in Young's modulus (E). The E changes with temperature due to weakening the interatomic integration which is defined by Equation (4.9) below [35]:

$$E = \frac{Stress}{Strain} = \frac{F / A_{tot}}{\Delta l / l_0} = \frac{F l_0}{\Delta l A_{tot}} \tag{4.9}$$

where F is applied force, A_{tot} is the area of the face where the force is applied, Δl is a strain, and l_0 is the original length. The E is used to analyze the mechanical behavior of the system. In this equation, the Joule heating temperature is a function of A_{tot}, ΔL, and L_0. The temperature dependence of Young's modulus of polycrystalline Cu was reported in reference [62]. Figure 4.12 shows the temperature dependence of Young's modulus of Cu. The E decreases by around 6 GPa (4 % compared to room temperature E_{cu} = 120 GPa) when the temperature rises by 100 °C from room temperature. Then, the spring constant of the actuator structure declines by 8 %. Therefore, the thermal loading (ΔT) at room temperature should be kept under 50 K to ensure stable operation of the actuator.

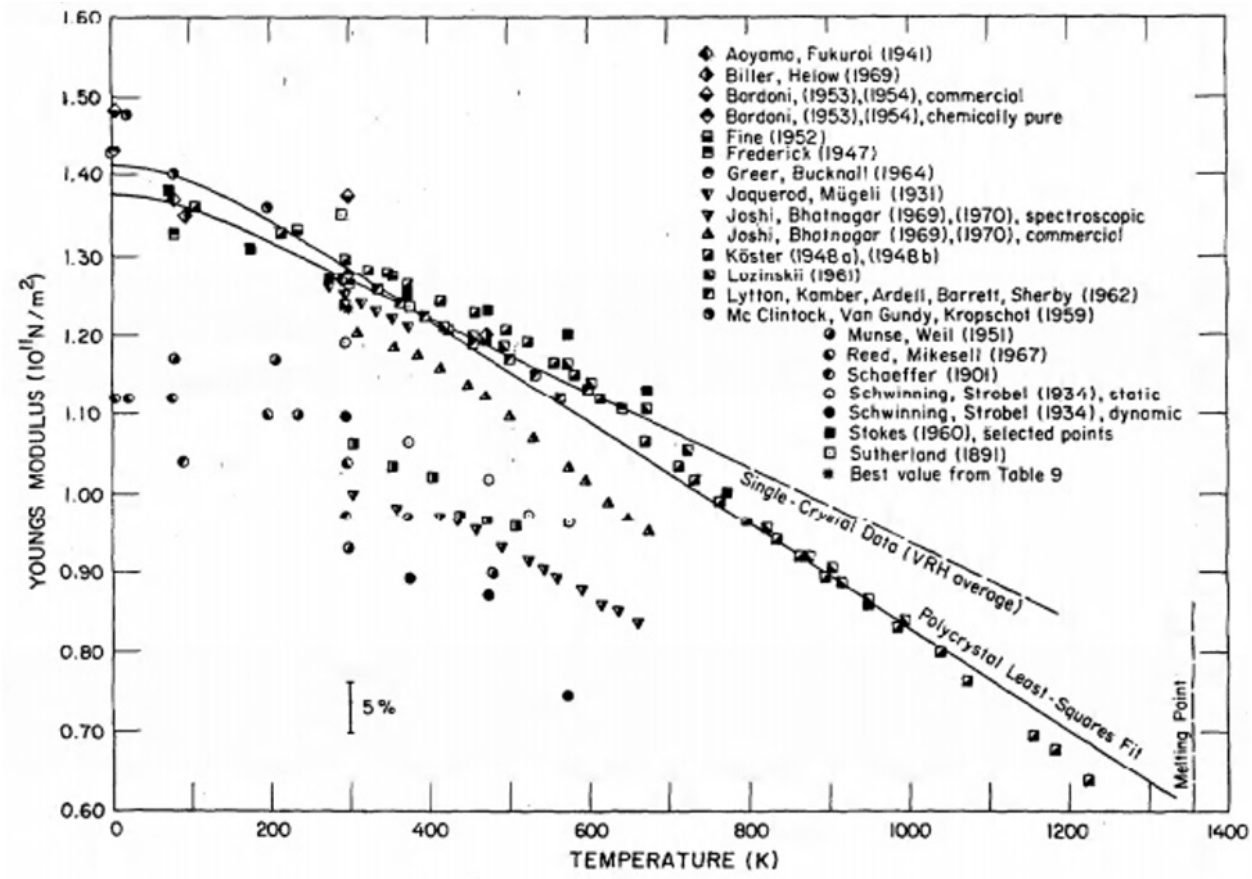

Reproduced from [Ledbetter, H. M., & Naimon, E. R., Elastic Properties of Metals and Alloys Copper, *Journal of Physical and Chemical Reference Data*, 3(4), pp. 897–935. 1974], with the permission of AIP Publishing.

Figure 4.12: Temperature dependence of Young's modulus of Cu [62].

Therefore, it is necessary to estimate the temperature change from Joule heating. According to Joule's first law, the total thermal power (P) generated by an electrical current (I) is proportional to the product of its resistance (R) and the square of the current:

$$P \approx I^2 R \tag{4.10}$$

The R depends on the dimensions of the conductor and the resistivity (ρ) of the material:

$$R = \rho \frac{L}{A} \tag{4.11}$$

where L is conductor length, and A is the cross-sectional area. The heat generated in the actuator structure is dissipated into the substrate, along with both cantilever arms by conduction. Both ends of the cantilever arms are connected to the substrate by a poly-silicon sacrificial layer. The heat conduction is described by Fourier's law. The rate of heat transfer through actuator (crossbar and serpentine spirng) is proportional to the temperature gradient and cross-sectional area as shown in Equation (4.12) [35]:

$$P = kA\frac{\Delta T}{L} \tag{4.12}$$

The total thermal power from Joule heating is proportional to the cross-sectional area (A), and the temperature difference (ΔT), but inversely proportional to the conductor length (L). k is the thermal conductivity. Equation (4.13), which combines the Joule heating and the thermal conduction, can be used to understand the Joule heating effect of the actuator depending on the structure and applied current. From this equation, the temperature (ΔT) variation is proportional to the square of the length of the wire and the applied current and is inversely proportional to the square of the cross-sectional area of the wire. Therefore, to minimize the undesirable thermal effects on the actuator design, the cantilever arms should have a short length and large cross-sectional area:

$$\Delta T = \rho I^2 \frac{l^2}{kA^2} \tag{4.13}$$

The effects of Joule heating on the actuator are shown in Figure 4.13. The calculation assumes that all the energy created by Joule heating is converted into thermal energy, and is dissipated to the substrate through both of the cantilever arms by conduction. Various dimensions of the cantilever arms are considered, whose details are given in Table 4.3. This figure can be used to predict the maximum heat loading of the device. For example, in order to achieve the desired ± 5 μm mirror deformation of the Lorentz DM with 30 % inter-actuator coupling, the actuator requires 6.4 mA of current in a 0.48 Tesla magnetic field. The dimensions of a 0.4 N/m spring constant cantilever is 200 μm (l_{arm}) × 550 μm (w_{arm})×1 μm (t_{arm}). Therefore, the maximum heat loading (ΔT_{max}) from Figure 4.13 is ~ 0.1 mK, which is negligible for DM operation.

Table 4.3: Calculation parameters, definitions, and the calculating range for initial curl-up displacement of the actuator design

Parameter	Definition	Range
W_c	Crossbar width	150 µm
Lc	Crossbar length	1800 µm
T_c	Crossbar thickness	20 µm
W_{arm}	Cantilever arm width	40 to 140 µm
L_{arm}	Cantilever arm length	100, 150, 200 µm
T_{tcu_arm}	Seed *Cu* thickness	200 nm
T_{cr_arm}	*Cr* stress layer thickness	100 nm
T_{bcu_arm}	*Cu* structural layer thickness	700 nm
T_{arm}	*Cu/Cr/Cu* Cantilever arm thickness	1 µm

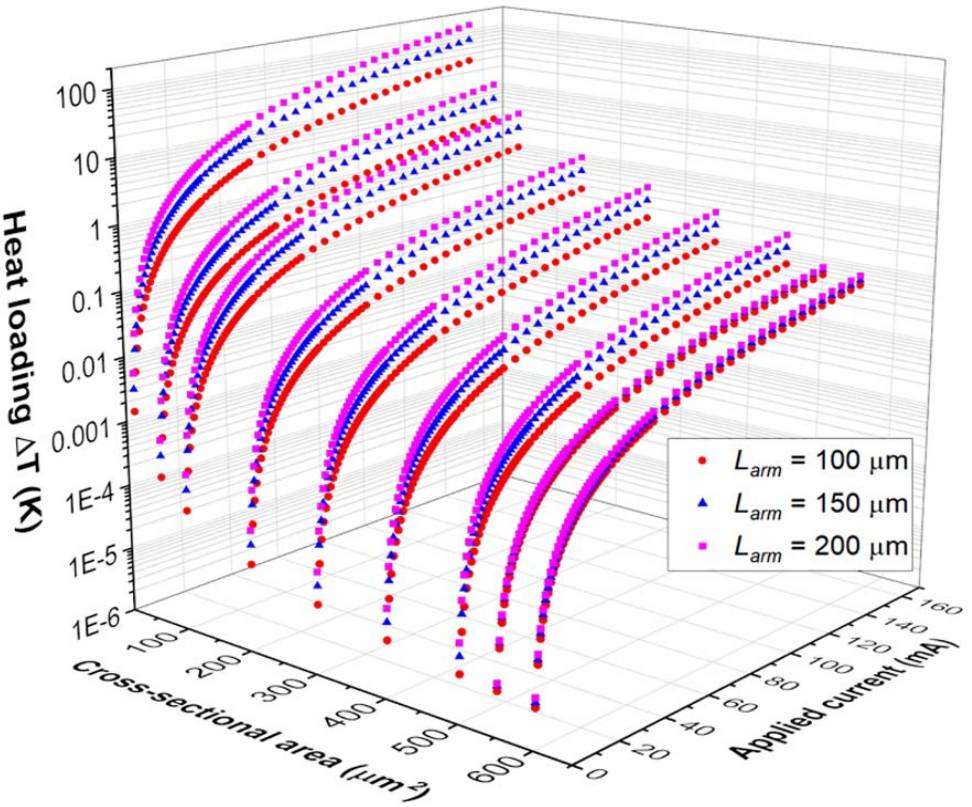

Figure 4.13: Heat loading (ΔT) on the center of the crossbar as a function of Joule heating current, and widths and thicknesses of the actuator.

4.4 Serpentine Spring Lorentz Actuator

This section introduces a serpentine spring Lorentz actuator design, and discusses the modeling and simulation of the actuator characteristics under normal operating conditions. Firstly, mechanical and thermal modeling is performed to determine the geometry of the crossbar and the thermal behavior of the actuator. Secondly, the mechanical and thermal properties of the device will be determined through COMSOL simulation and compared with the modeling results.

The new design is based on a thick and rigid silicon crossbar and flexible serpentine springs constructed using bulk-micromachining. The bulk-micromachining can form a thick silicon crossbar, a pillar, as well as thin spring arms sequentially by KOH bulk-micromachining. The cavity beneath the actuator formed by KOH bulk micromachining can provide a deep enough space to get large actuator stroke. Four important considerations for the actuator design are mentioned below:

- The cantilever arms are replaced by a long single crystal silicon serpentine spring to satisfy the Lorentz DM inter-actuator coupling (10 ~ 30 %) and resonance frequency (> 0.8 kHz) of the entire DM system.
- The Cr stress layer is removed because the initial deflection can be achieved by applying a conductive Al film coating on the silicon serpentine spring.
- The serpentine spring should contain a current carrying metal wire that is short and thick enough to limit Joule heating to acceptable levels.
- The crossbar thickness should be thick enough so that it does not bend when a force is applied to the crossbar.

The actuator design and its working principle is shown in Figure 4.14. The actuator is designed based on flexible supporting serpentine springs on either end of a central thick and rigid crossbar. The rigid crossbar is intended to prevent the crossbar from bending due to its acting opposing force when the

mirror is deformed. Both the crossbar and serpentine springs are made of single crystal silicon, etched from a silicon wafer. The serpentine springs provide mechanical support for the crossbar, a pathway for electrical current, and heat sinking to the substrate. To allow for the current flow necessary for the Lorentz force mechanism, the crossbar and springs are coated with 1.5 μm thick Al.

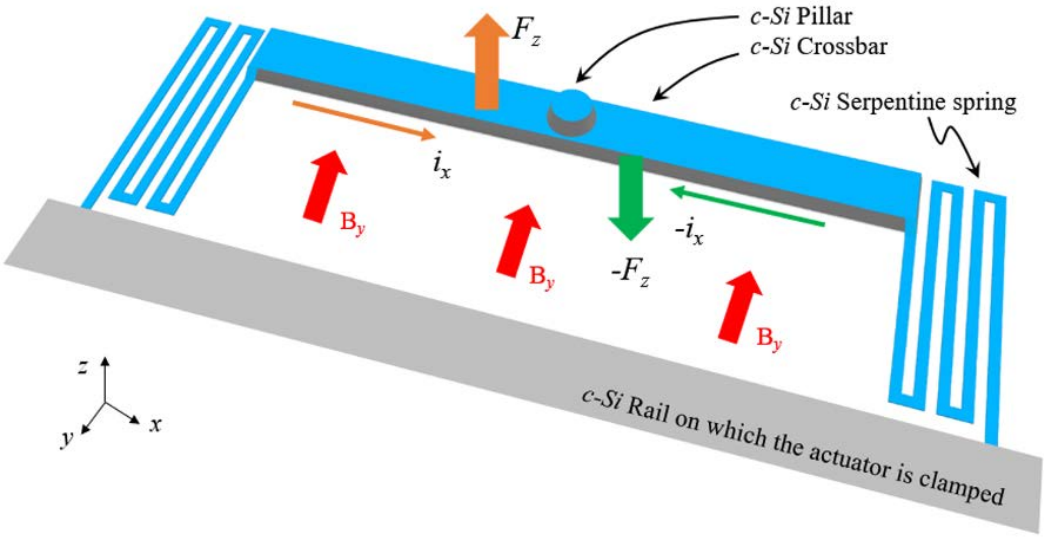

Figure 4.14: Illustration of the c-Si serpentine spring Lorentz actuator design and working principle.

Figure 4.15(a) shows a fabricated 5 × 5 actuator array. The crossbars are rotated 45 degrees to obtain maximum Lorentz force by increasing the crossbar length. The 2080 μm (length) x 200 μm (width) crossbar contains a central pillar which is used to contact the above mirror to be manipulated in Figure 4.15(c). The height of this pillar prevents the crossbar from touching the mirror. Each actuator is connected to a rigid anchor rail, also etched from the silicon wafer. The narrow but rigid (560 μm width × 300 μm thickness) anchor rails allow for an extensive array of actuators to be fabricated in close proximity to each other. Moreover, the rails dissipate heat and provide space for an electrical wire to be connected to an external circuit. Figure 4.15(b) shows the deformable mirror system after bonding the Al/SU-8/Al mirror substrate and actuator array substrate.

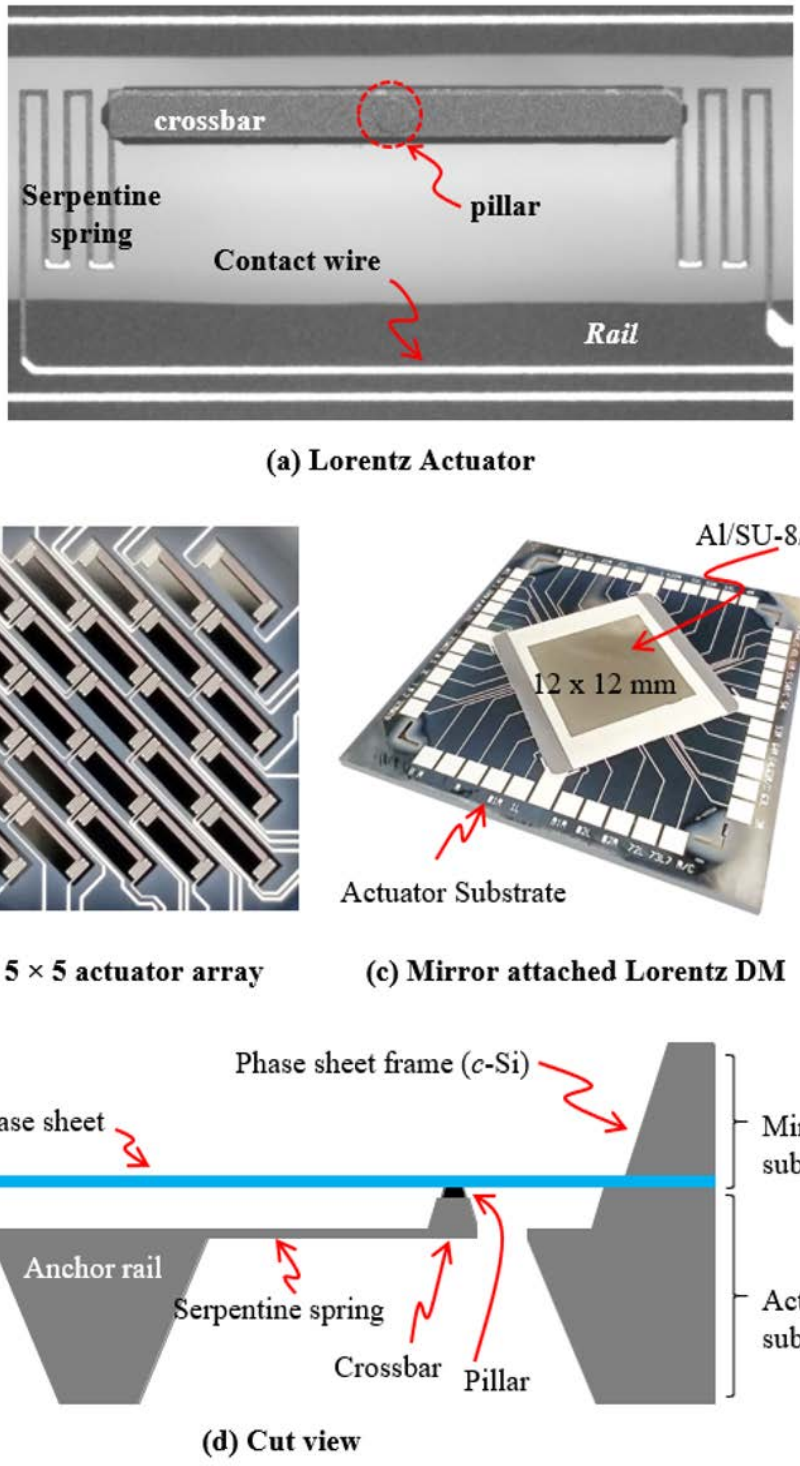

Figure 4.15: (a) Microscope image of a fabricated 5 × 5 c-Si serpentine spring Lorentz actuator array. (b) Mirror attached DM structure. (c) Side view of the assembled DM.

4.4.1 Modeling

4.4.1.1 Geometry of Crossbar

The design of the serpentine spring Lorentz actuator shown in Figure 4.14 begins with determining the dimensions of the crossbar providing the Lorentz force. The crossbar length was set to 2080 µm when including 2-loops of serpentine spring, and the width is fixed at 200 µm. Applying the same model used in section 4.3, the crossbar bending is allowed within 10 % (0.5 µm) of the total actuator displacement of ± 5 µm. From Figure 3.8, for a 10 % inter-actuator coupling where the most rigid spring is required, a force of 32.9 µN is necessary for ± 5 µm mirror deformation. Substituting this value into Equation (4.4), the thickness of the crossbar suitable for crossbar bending of less than 10 % was calculated to be 22.5 µm. Therefore, the crossbar was designed with a thickness of 25 µm to minimize bending sufficiently. Since the actuator structure will be constructed using silicon bulk-micromachining, the thick and smooth surface of the crossbar can be easily obtained. The material properties used in this calculation are shown in Table 4.4. The Young's modulus varies in different crystal planes in single crystalline silicon wafer because it is an anisotropic crystal. The crossbar and cantilever arms were designed and modeled along the <100> crystal plane to ensure sufficient design and fabrication.

Table 4.4: Material properties for the serpentine spring Lorentz actuator modeling and simulation

Properties / Material	crystalline Si	Al
Density (Kg/m^3)	2330	2700
Young's Modulus (GPa)	130 <100> [63]	69
Poisson's Ratio	0.28	0.35
Thermal Conductivity (W/m·K)	130	237
Heat Capacity at Constant Pressure (J/(kg·K))	700	904
Coefficient of Thermal Expansion, CTE (µm/K)	2.6	23.1
Electrical conductivity (× 10^6 S/m)	-	35.5
Yield Strength at Room Temperature (GPa)	3.8 [64]	0.124[40]

4.4.1.2 Thermal Effect

Figure 4.16 shows the structure of a serpentine spring with its crossbar in the xy plane. The serpentine spring can be defined as a repeating pattern of individual spring loops. A single loop consists of two span beams and two connector beams. For the rest of this thesis, the lengths of the connector beams and span beams are fixed. Only beam thickness and width are varied to examine the spring rigidity. The serpentine spring consists of 2-loops with one additional span beam. Each connector beam is of length Lsc = 40 µm and each span beam is of length $Ls_2 = Ls_3 = Ls_4$ = 700 µm except for the first and last span beam. The Ls_1 (crossbar side) and Ls_5 (anchor side) are 500 µm and 750 µm respectively. The thickness and width of each serpentine spring are varied. The crossbar dimension has a length of 2080 µm (L_c), a width of 200 µm (W_c), and a thickness of 25 µm (T_c).

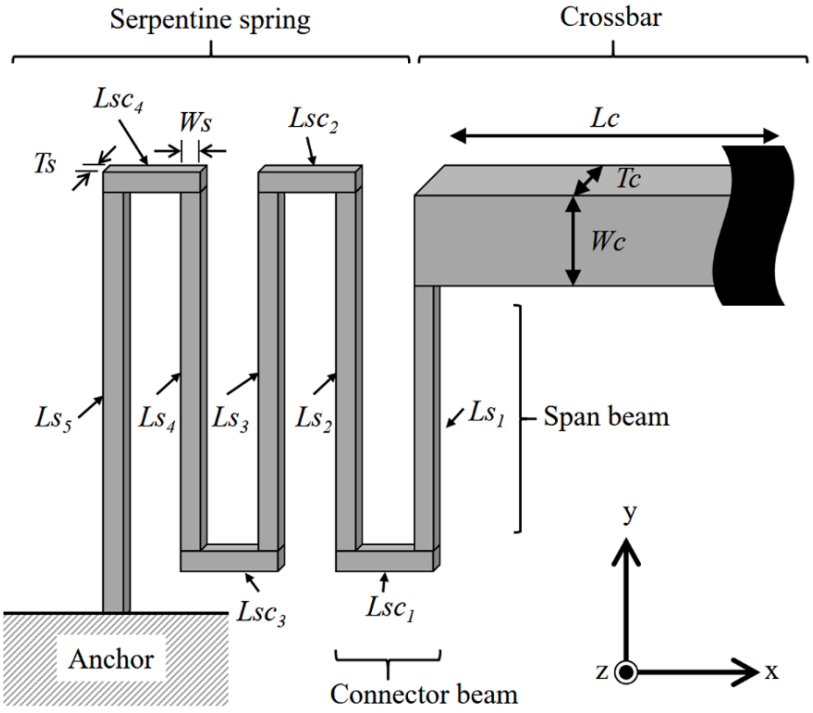

Figure 4.16: Serpentine Spring with the crossbar.

As discussed before, the heat generated by the current flowing in the conductor (Joule heating) changes the mechanical properties of the Lorentz actuator. The Joule heating dependence on the operation

current and the structure of the actuator design was evaluated using Equation (4.13). The maximum temperature change (ΔT) depends on the cross-sectional area of the serpentine spring and the applied current. The material properties and structural parameters used for modeling the device are listed in Tables 4.4 and 4.5, respectively.

Table 4.5: Calculation parameters, definitions, and the calculation range for the thermal effect of the serpentine spring actuator design.

Parameter	Definition	Range
L_c	Crossbar length	2080 µm
W_c	Crossbar width	200 µm
T_c	Crossbar thickness	25 µm
T_{Al}	Aluminum wire thickness	1.5 µm
n	Number of loop of the serpentine spring	1, 2, and 3
L_{sc}	Connector beam length	40 µm
L_{s1} *and* L_{s5}	First and last span beam length in case of 2-loops serpentine spring	500 µm & 750 µm
T_s	Silicon thickness of serpentine spring	4, 6, 8, 10, 12, 14, & 16 µm
W_s	Serpentine spring width	24, 26, 28, 30, 35, & 40 µm
A	Cross-sectional area of serpentine spring	

T_s (µm)	4	4	⋯	10	⋯	16
W_s (µm)	24	26	⋯	30	⋯	40
A ($\times 10^{-12}$m^2)	96	104	⋯	300	⋯	640

The calculation result of ΔT on the crossbar as a function of the variable cross-sectional area of the serpentine spring and applied current is shown in Figure 4.17. The red dotted region shows a ΔT less than 50 K as a function of applied current and the cross-sectional area of the serpentine spring. Figure 4.18 shows the temperature dependence of Young's modulus on <100> orientation crystalline silicon [63]. The Young's modulus of <100> silicon decreases by about 0.5 % as the temperature increases by 100 K

at room temperature. Then, the spring constant of the actuator declines by 0.25 %. Therefore, a maximum ΔT of 50 K for the actuator would not change the device performance.

These results show that the actuation current from 13.6 mA (30 % crosstalk) to a very high 37.6 mA (10 % crosstalk) can be applied to the actuator without changing the device performance. Therefore, the serpentine spring dimension can be selected from Figure 4.17 by comparing with Figure 3.8 (spring constant *vs.* Lorentz DM inter-actuator coupling) and Figure 4.20 (spring thickness *vs.* spring constant).

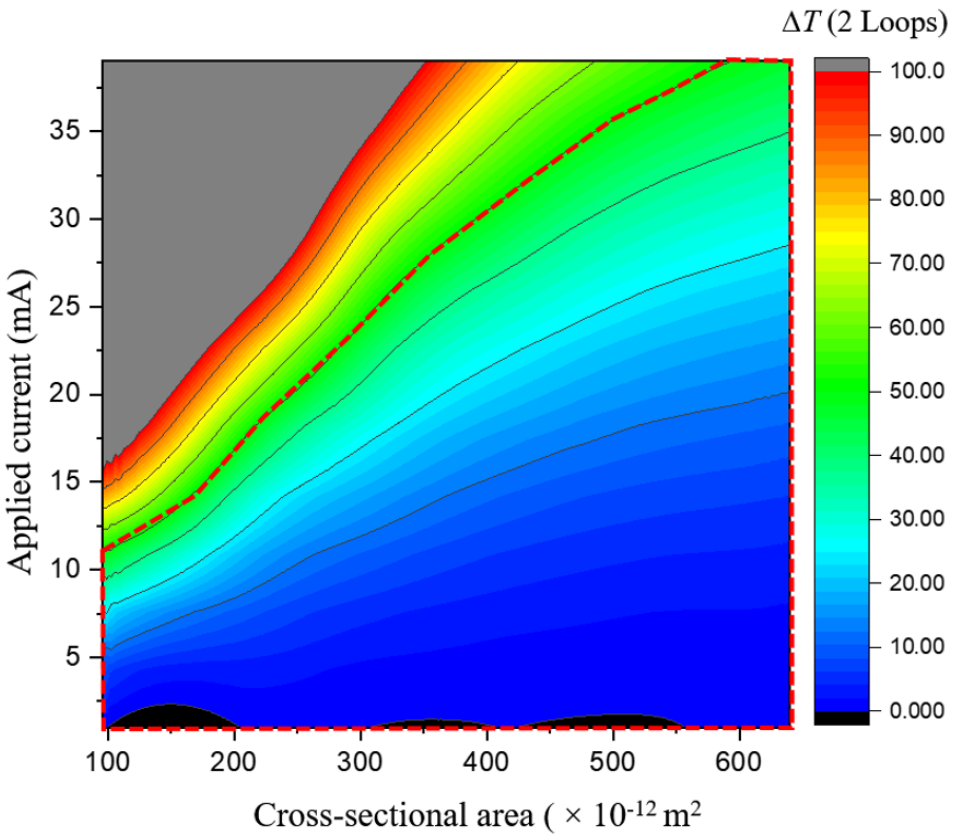

Figure 4.17 Maximum temperature change (ΔT) on the crossbar as a function of applied current and cross-sectional area of the **2-loops** serpentine spring actuator. The red dotted area shows the region where $\Delta T \leq 50$ K.

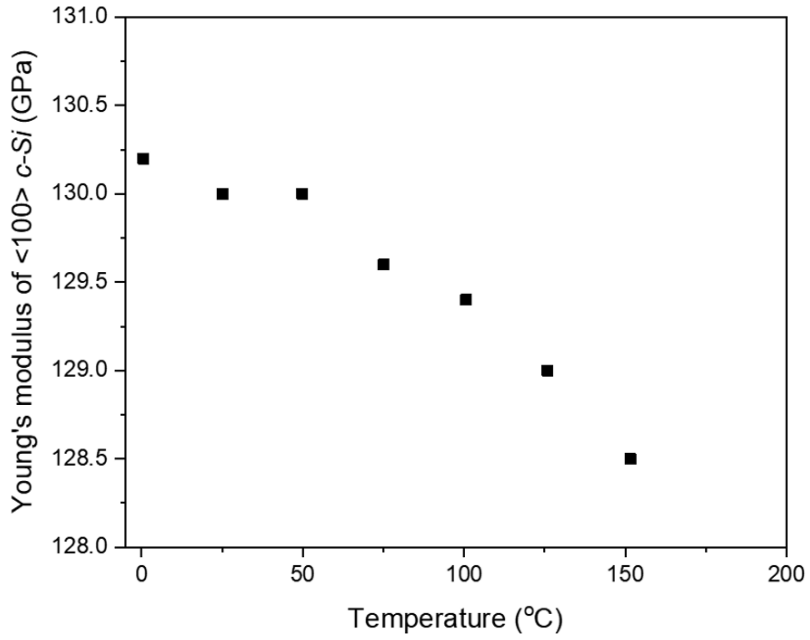

Figure 4.18: Temperature dependence of Young's modulus in the <100> silicon plane [63].

4.4.2 FEM Simulation

Simulations are used to verify the modeling results and to identify the assumptions established during modeling. Different types of COMSOL simulations are performed to predict the performance of the actuator. COMSOL Multiphysics is quite flexible in terms of meshing options and types of elements. The Parametric sweep option in COMSOL can be used to quickly build models for different simulations with full control of simulation parameters. The parameters and material properties used in the simulation can be found in Table 4.4 and Table 4.5.

4.4.2.1 Spring Constant

The spring constants of the actuator are studied using Solid Mechanics in the Structural Mechanics Module of the COMSOL Multiphysics software. To meet the required Lorentz DM inter-

actuator coupling of 10 to 30 %, the spring constant of the actuator is calculated for different widths and thicknesses of the serpentine spring.

The COMSOL simulation starts with the construction of a 2-loop actuator in the model builder. In this simulation, since the serpentine spring is composed of a double layer Al conductive film and crystalline silicon structural layer, the equivalent Young's modulus (E_{eq}) is applied according to each silicon layer thickness as shown in Table 4.6. Figure 4.19 shows an example of a constructed and deflected 2-loops actuator with a 2 μN force applied to the crossbar in the z-axis.

The linear deformation profile of all different geometries of the actuator with an applied force is presented in the same simulation module as shown in Figure 4.20. The linearity of the actuator deformation facilitates the prediction of the performance of the entire DM system. Simulation results for the spring constant of the serpentine spring Lorentz actuator as a function of serpentine spring thickness and width are shown in Figure 4.21. As the thickness and width of the serpentine spring increase, the spring constant also increases.

Table 4.6: Equivalent Young's modulus (E_{eq}) and Shear modulus (G_{eq}) of Al/Silicon double layered serpentine spring with varying silicon thickness.

Definition		***Value***
E_{eq} (GPa)	Equivalent Young's Modulus $E_{eq} = \frac{T_{Al}E_{Al}}{(T_{\mathrm{Al}} + T_{\mathrm{c-Si}})} + \frac{T_{c-Si}E_{c-Si}}{(T_{\mathrm{Al}} + T_{\mathrm{c-Si}})}$	T_{Al} = 1.5 (Unit = μm)
G_{eq} (GPa)	Equivalent Shear Modulus $G_{eq} = \frac{E_{eq}}{2(1-v)}$	

$T_{c\text{-}Si}$	4	6	8	10	12	14	16
E_{eq}	113	118	120	122	123	124	125

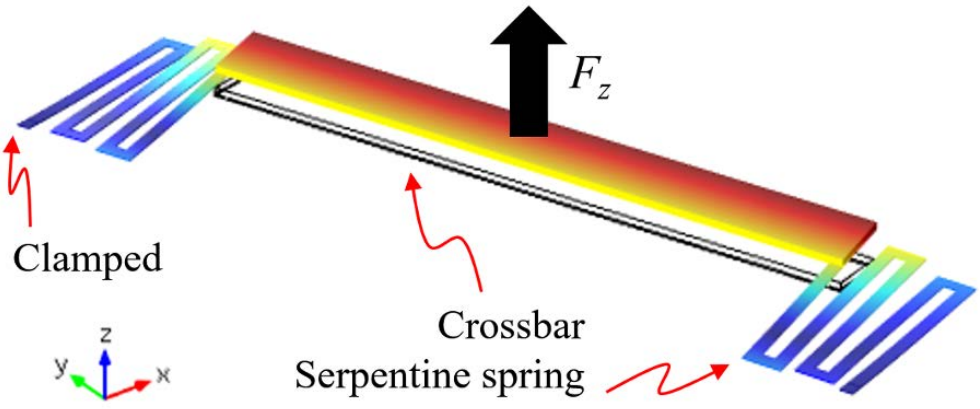

Figure 4.19: Deflected serpentine spring actuator structure by z-directional loading of F_z in COMSOL Multiphysics.

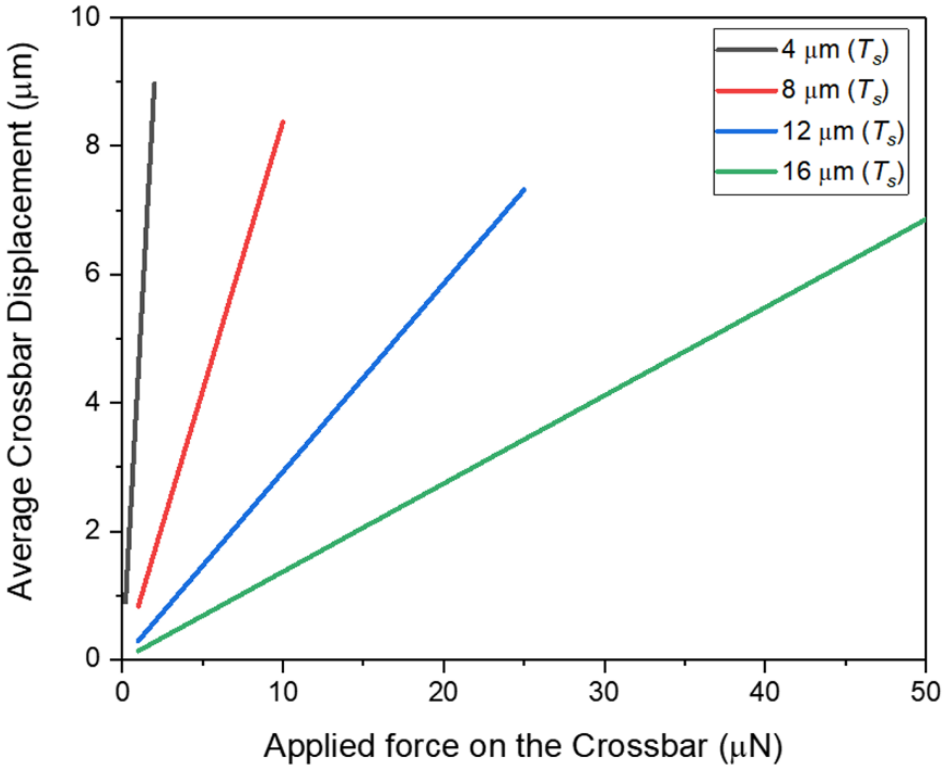

Figure 4.20: Crossbar displacement in z-axis as a function of the thickness of the serpentine spring (T_s) and applied force on the crossbar with 28 μm (W_s) (COMSOL simulation result).

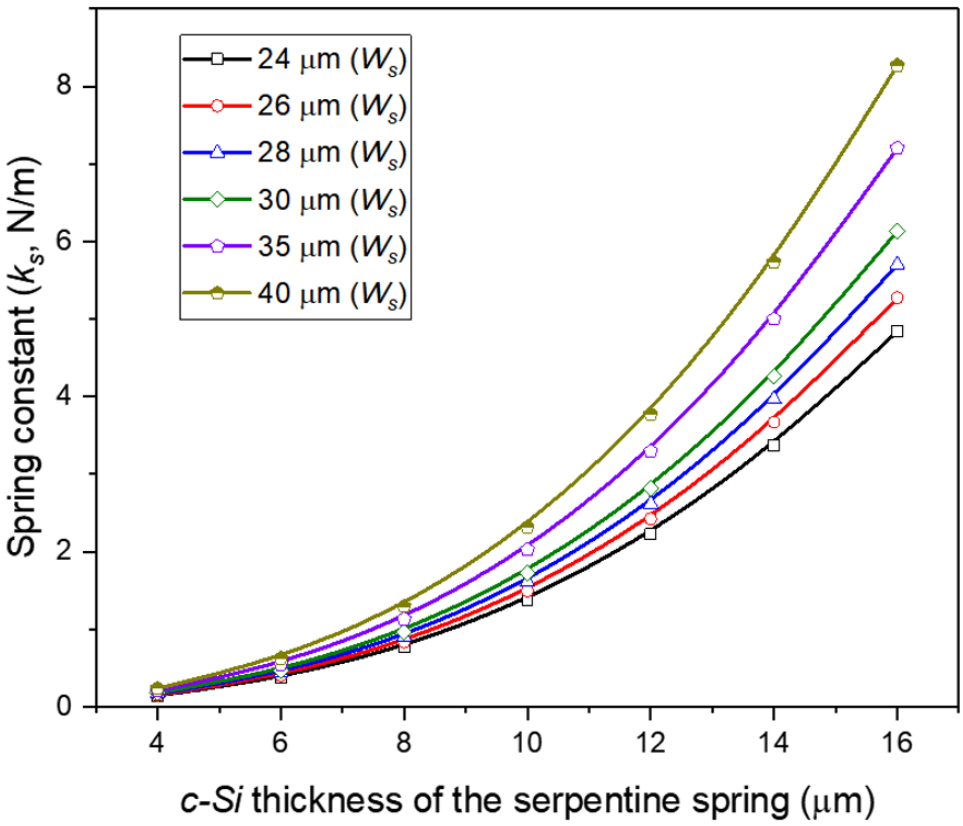

Figure 4.21: The spring constant of the serpentine spring Lorentz actuator as a function of thickness and width of a 2-loops serpentine spring. The thickness of Al is fixed to 1.5 μm. (COMSOL simulation result)

4.4.2.2 Stress Failure

The maximum stress of the serpentine spring should not exceed the yield strength of the material. This is to prevent failure during operation. To find the maximum stress on the actuator, a spring foundation with respect to the mirror spring constant (k_m) was added to the solid mechanic's module (see Figure 4.22(a)). The spring constant of the Al/SU-8/Al mirror as a function of the actuator stiffness can be found in Figure 3.8. In order to examine the stress failure of the actuator, the maximum stress value of the actuator was analyzed for the serpentine spring as a function of its minimum thickness and maximum thickness. The z-axis force applied on the crossbar increased gradually to determine the maximum stress value when the actuator is displaced by 5 μm.

Simulation results show that the stress is concentrated at each corner of the spring as shown in Figure 4.22(b) (red dotted circles). The calculated maximum stress value does not exceed 12 MPa in both 24 µm and 40 µm serpentine springs as shown in Figure 4.23. The yield strength of crystalline silicon is ~ 3.8 GPa at 20 °C as shown in Figure 4.24, which is over 100 times higher than the maximum stress of 12 MPa.

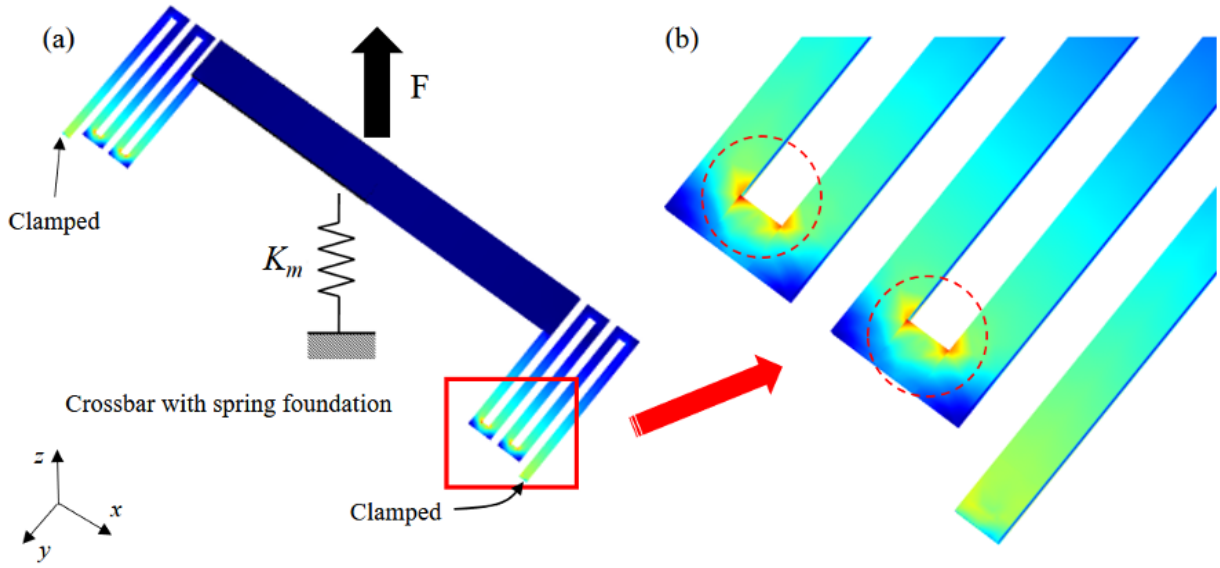

Figure 4.22: (a) A stress distribution diagram of force applied to the z-axis of the serpentine spring Lorentz actuator with an attached spring foundation that replaces the Al/SU-8/Al mirror. (b) Maximum stress is shown in the corner of serpentine spring (red dotted circle).

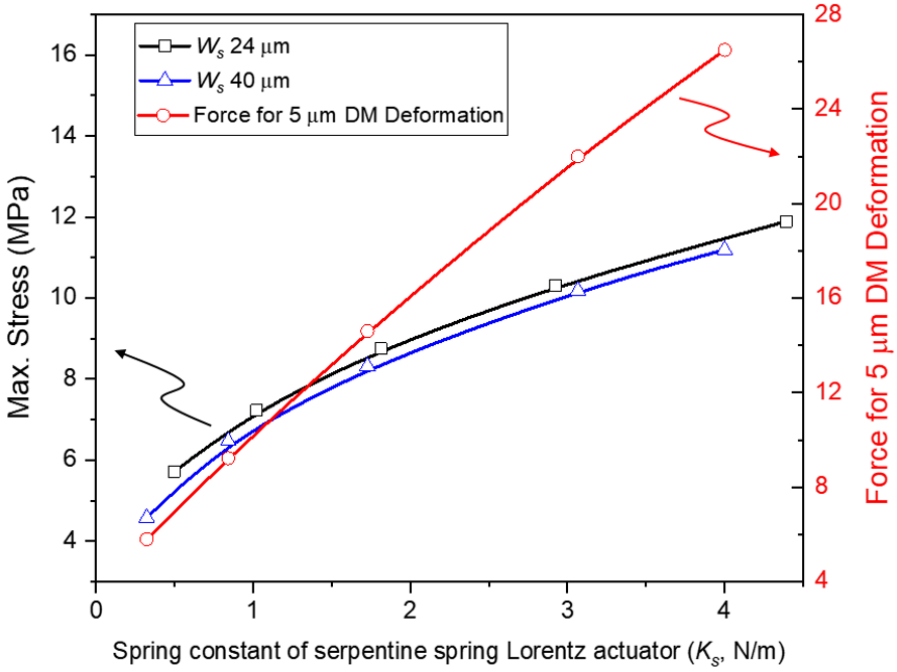

Figure 4.23: Maximum stress on the actuator as a function of the force to deform the DM 5 µm is applied on the crossbar.

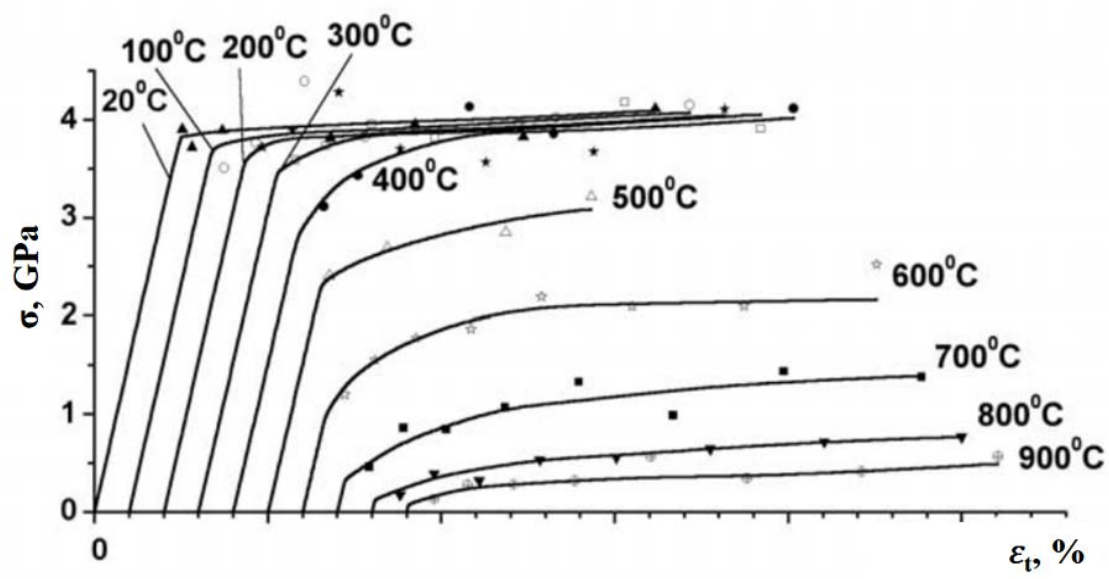

Red colored: Reproduced from [Milman, Y. V., Gridneva, I. V., & Golubenko, A. A., Construction of stess-strain curves for brittle materials by indentation in a wide temperature range. Science of Sintering, Vol. 39(1), pp. 67–75, 2007. https://doi.org/10.2298/SOS0701067M], with the permission of Science of Sintering

Figure 4.24: Stress-strain curves for single-crystal silicon at different temperatures [64].

4.4.2.3 Thermal Effect

Joule heating, which can cause a significant problem for device performance, was simulated and compared with the modeling results in section 4.4.1.2. The Joule Heating module in the COMSOL software was used. In order to determine the heat loading characteristics, only the smallest, middle, and largest cross-sectional area (see Figure 4.25(a)) dimensions of the silicon serpentine spring were selected. The thermal characteristics of all the different dimensions of actuators are shown in Appendix B.

(a)

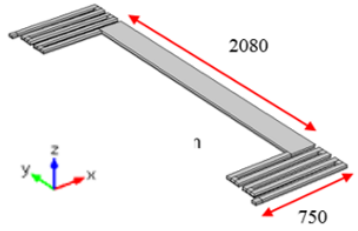

Actuator dimension

- Crossbar length (L_C) = 2080 µm
- Crossbar width (W_C) = 200 µm
- Crossbar thickness (T_C) = 25 µm
- 2-loops serpentine spring dimension

Spring width (W_s)	24 µm	30 µm	40 µm
Spring thickness (T_s)	4 µm	10 µm	16 µm
Cross-sectional area (A)	96 µm^2	300 µm^2	640 µm^2

(b)

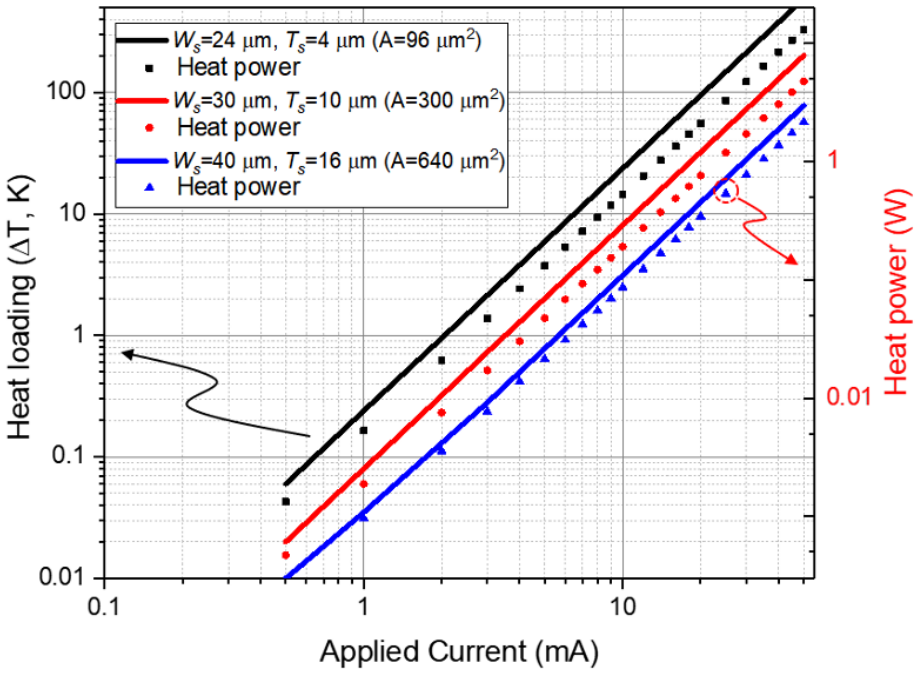

Figure 4.25: (a) The actuator dimensions. (b) Maximum heat loading (left y-axis) and heat power (right y-axis) on the center of the crossbar as a function of applied current with various cross-sectional areas of the serpentine spring. (COMSOL simulation result)

Figure 4.25(b) shows the relationship between the heat loading by Joule heating and the cross-sectional area of the serpentine structure. The dotted line in the graph represents the temperature change corresponding to the same colored heat loading line. The simulation result of heat loading (ΔT) on the actuator fits within about 10 % of the simulation results in Figure 4.17. For example, the heat loading (ΔT) of the actuator with a 98 μm^2 cross-sectional area of the *c-Si* serpentine spring shows a simulation result of 2.02 K and 2.17 K for a modeled 5 mA current.

In this research, a cold (ΔT < 50 K) crossbar is required to operate the DM. Moreover, anodic bonding or metal fusion bonding techniques, which are used to bond the actuator and the mirror, require a hot crossbar temperature (ΔT > 200 K). This figure shows that the Joule heating of the device is adjustable for use in the bonding process as well as for driving the device due to a sufficiently low ΔT.

4.4.3 Summary of Serpentine Spring Lorentz Actuator Design

With the purpose of defining the geometry of the serpentine spring Lorentz actuator, the thermal and mechanical properties of the design were calculated analytically, as well as by using COMSOL simulation. Simulation and analytical results for heat loading show a mismatch of less than 10 %. These results promote the prediction of the performance of the serpentine spring Lorentz actuator.

By comparing Figure 4.17 and Appendix B for heat loading with Figure 4.21 (spring constant) and Figure 3.8 (design criteria of DM system), the required spring constant of the actuator (*ka*) and the maximum possible current can be obtained according to the inter-actuator coupling of the Lorentz DM. The comparison result of the Al/SU-8/Al mirror inter-actuator coupling, spring constant of the actuator, spring thickness, and maximum allowable current for 24 μm width serpentine spring are summarized in Table 4.7. From this table, most of the 2-loops serpentine spring dimensions with 24 μm width and 6.4 μm to 13.1 μm thickness are available to be applied to a Lorentz DM system with ± 5 μm mirror stroke. However, it can be seen that the 24 μm width actuator is not applicable to the Lorentz DM system with less than 20 % inter-actuator coupling. This is due to a current margin of -3.0 % in a 0.4 Tesla magnetic

field. In such a case, it is possible to increase the Lorentz force margin by using a stronger magnet. For example, if the magnetic field is increased to 0.7 Tesla, the current margin increases to 41.1 %, and the actuator can be applied to the Lorentz DM design. More comparison results of the various widths of serpentine spring Lorentz actuator relative to the Lorentz DM inter-actuator coupling are shown in Appendix C.

Table 4.7: Comparison between Lorentz DM inter-actuator coupling, the spring constant of the actuator, c-Si spring thickness, and maximum applicable current for a serpentine spring Lorentz actuator with a 24 µm width serpentine spring.

Items	**Values**				
The Lorentz DM inter-actuator coupling (%)	30.0	25.0	20.0	15.0	10.0
(A) Required force for 5 µm deformation of Al/SU-8/Al mirror (µN)	5.4	6.05	6.75	7.5	8.2
(B) Required spring constant of actuator (N/m. from COMSOL)	0.8	1.1	1.65	2.8	4.9
c-Si spring thickness of the serpentine spring actuator	6.4	7.4	8.7	10.6	13.1
Cross-sectional area of *c-Si* spring (um^2)	153.6	177.6	208.8	254.4	314.4
(C) Max. allowable current (mA) for $\Delta T \leq 50$ K (From COMSOL)	13.5	15	17.5	20.7	25.1
* Required force for 5 µm deformation of the Lorentz DM (µN)	9.4	11.55	15	21.5	32.7
** Required current for 5 µm deformation of the Lorentz DM (mA) with 0.4 Tesla magnet	11.3	13.9	18.0	25.8	39.3
Current margin (%)	16.3	7.5	**-3.0**	**-24.8**	**-56.6**
** Required current for 5 µm deformation of the Lorentz DM (mA) with 0.7 Tesla magnet	6.5	7.9	10.3	14.8	22.5
Current margin (%)	52.2	47.1	41.1	28.7	10.5

* Required force for 5µm deformation of the Lorentz DM = (A) + ((B) × 5 × 10^{-6}m)

** Required current for Lorntz force generated on the crossbar (2080 µm length) within 0.4 and 0.7 Tesla magnetic field.

5

Microfabrication

Contents

5.1 Introduction

The new proposed Lorentz actuator structure can be driven with low voltages (< 1V), and low currents (~ 10 mA) with the fabricated mirror composed of a Al/SU-8/Al membrane. A simple actuator structure ensures high fabrication yield and low cost. Various techniques were investigated to fabricate both the cantilever arm and serpentine spring Lorentz actuators. In the cantilever arm Lorentz actuator design, the spring was fabricated on a silicon wafer using surface micromachining by sputter deposition and electroplating on a thick Cu crossbar. The serpentine spring Lorentz actuator array was fabricated

using a bulk micromachining technique, which constructs the spring, crossbar, and pillar in sequence with the KOH etching process. All materials and dimensions of the Lorentz actuator were selected based on the COMSOL simulation and modeling results presented in Chapter 4.

5.2 Fabrication of the Cantilever Arm Lorentz Actuator

This section briefly describes the actuator fabrication process. More information and discussion can be found in [61].

5.2.1 Mask Preparation

The Lorentz actuator is formed with three different height structures of cantilever arms, crossbars, and pillars. A total of three transparent e-beam masks fabricated in the nanoFab lab (University of Alberta) were used to fabricate the device. Various dimensions of the crossbar and cantilever arm structure were prepared to analyze the mechanical characteristics of the actuator shown in Table 5.1. The mask design for each process is shown in Figure 5.1. Mask 1, Mask 2 and fliped-off Mask 1 are used.

Table 5.1: Parameters and dimensions of the actuator prepared in the mask.

Parameters	Dimension (μm)
Crossbar Length	800, 1800, 2300, and 3300
Crossbar width	50, 100, and 150
Cantilever arm length	100, 200, and 300
Cantilever arm width	40, 60, and 80

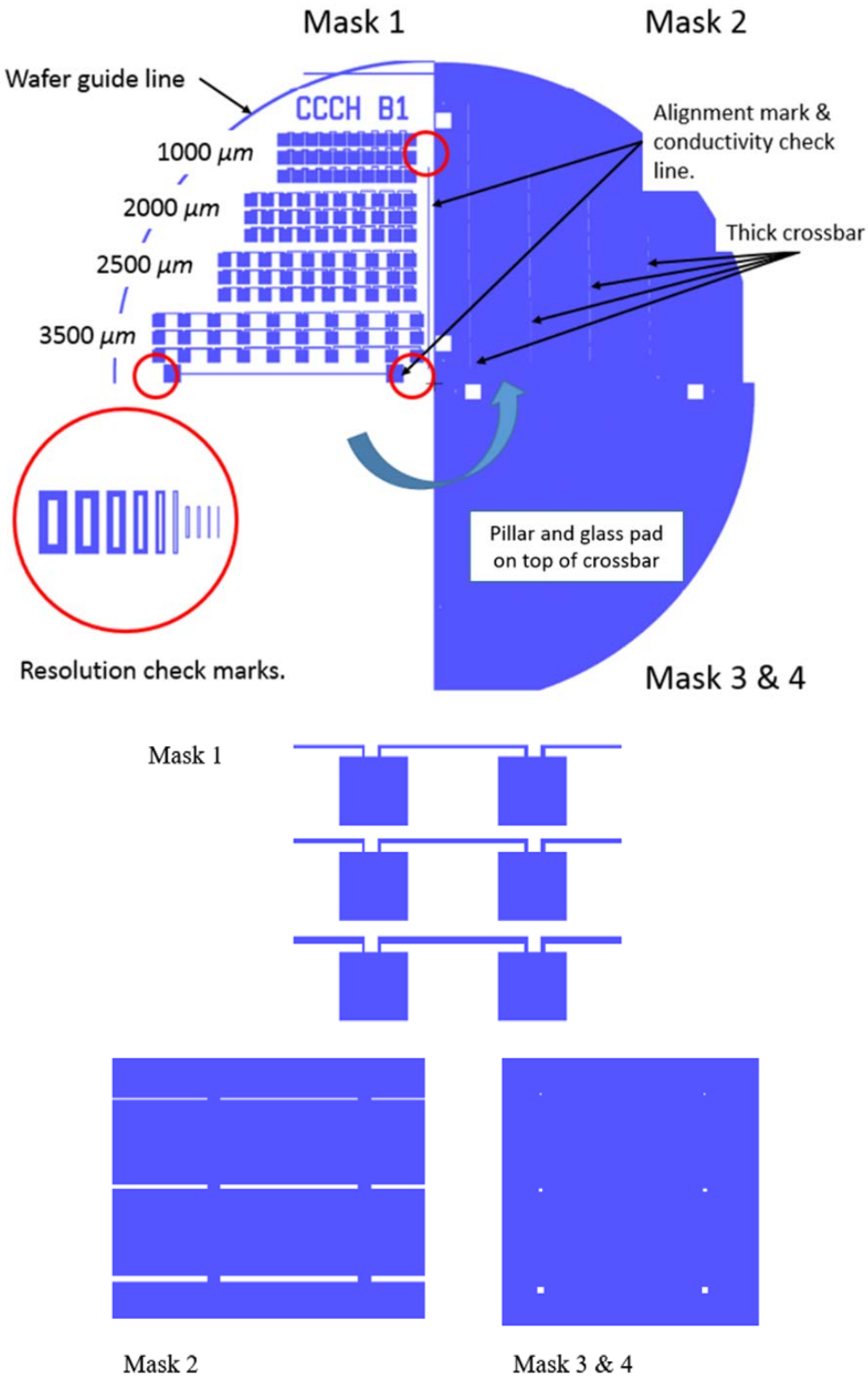

Figure 5.1: (Top) Mask design for the actuator. Masks 3 and 4 were prepared for the future bonding process. (bottom) Mask 1 is actuator seed layer for the electroplating. Mask 2 is electroplating mold. Mask 3 & 4 is pillar structure.

5.2.2 Fabrication Process

The actuator fabrication process is illustrated in Figure 5.2. Surface micromachining and electroplating techniques with a three-mask process are mainly used to fabricate the actuator. An electroplating technique capable of depositing a thick Cu film over 15 μm thick, and the method for producing thick molds for plating with SPR220-7 photoresist are reported in the NSFL internal research report [61]. The fabrication process flow is as follows:

a) The starting substrate is a <100> orientation *c-Si* wafer with ~ 1 μm of wet thermal SiO_2 as an insulator.
b) The actuator fabrication sequence begins with sputtering an ~ 25 nm titanium adhesion layer, a 200 nm silicon sacrificial layer, a 700 nm Cu structural layer, a 100 nm Cr stress layer, and finally a 200 *nm* Cu seed layer for electroplating the thick Cu crossbar.
c) Mask 1 is used to define this overall actuator structure and the crossbar shape with negative tone photoresist SU-8. The SU-8 is used as a wet etch barrier for the selective chrome etchant Chromium Cermet Etchant TFE (CrCE-TFE) process because the potassium hexacyanoferrate contained in CrCE-TFE can decompose most of the positive photoresists. An APS 100 Cu etchant etches away the first Cu seed layer with an etch rate of ~ 8.5 nm/sec. The etch is stopped in the Cr film. Then, the CrCE-TFE removes the unnecessary Cr layer without damaging the Cu structural layers.
d) A thick enough SPR 220-7 positive tone photoresist layer is spun on, and the second mask will cover the surface, except for the crossbar, allowing the exposed Cu surface to be the seed layer for electroplating the several μm thick Cu reinforcement layer.
e) The thick crossbar is formed by electroplating. The SPR 220-7 mold is removed by acetone rinsing.

f) Then, actuator geometry is defined by stripping the bottom Cu film with APS 100 etchant after the lithography process using Mask 1 and the SPR 220-7 photoresist.

g) Finally, the actuator fabrication is completed with the release of the device by an XeF_2 isotropic etch of the underlying titanium adhesion layer and silicon sacrificial layer. The 10:1 BOE is used to remove any possible oxide layer before the release process.

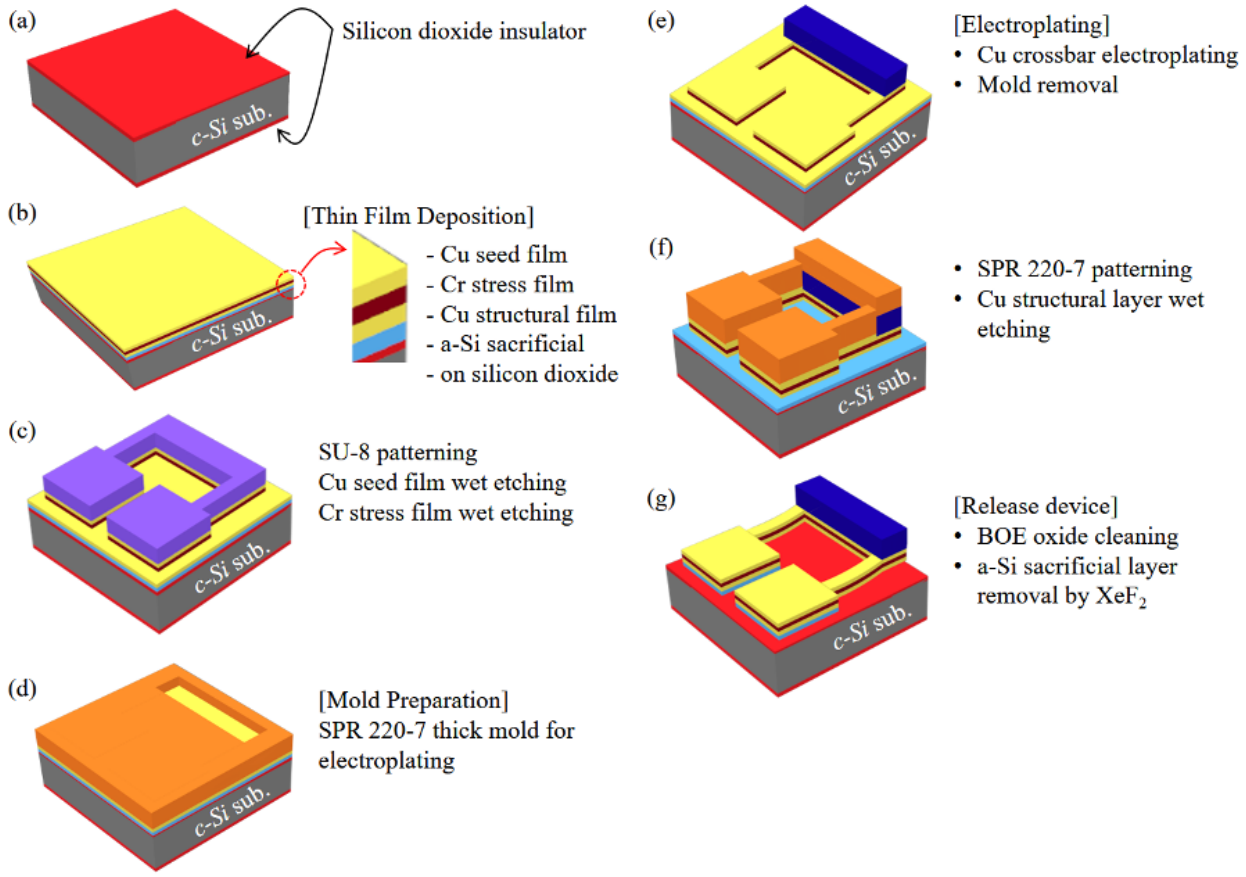

Figure 5.2: Surface micromachining process for the electroplated actuator fabrication.

5.2.3 Summary

In this section, the pre-stressed cantilever arms Lorentz actuator was fabricated. However, the device was not released during the isotropic XeF_2 dry etching process (see Figure 5.3). Even though the isotropic XeF_2 over-etch technique is very selective to the silicon, it is susceptible to oxygen

contamination. The sacrificial layer was oxidized by the long immersion time in a sulfuric acid based Cu plating solution (over 4 hrs). Though this problem can be solved by adding a protection layer on the silicon sacrificial layer, the overall fabrication process would become more complicated. Moreover, the electroplated thick Cu crossbar was not smooth enough for the bonding process (see Figure 5.4). Therefore, a new single crystalline serpentine spring Lorentz actuator was designed in Chapter 4 and the fabrication process will be introduced in the next section. The fabrication result for the new actuator will be provided as well.

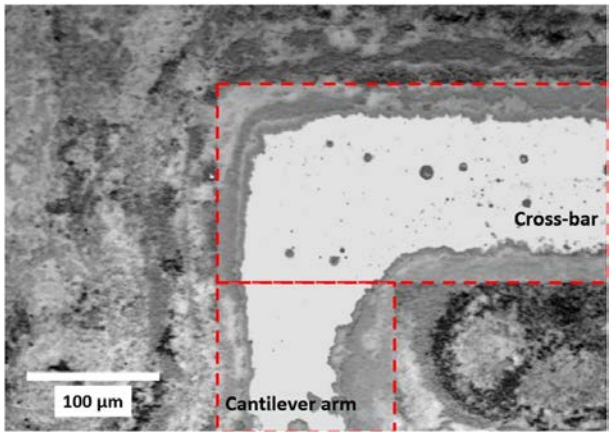

Figure 5.3: Remaining sacrificial silicon layer after XeF_2 etching due to oxidation by the sulfuric acid base Cu plating solution. A Red line shows the crossbar and cantilever arm feature on top of the sacrificial layer.

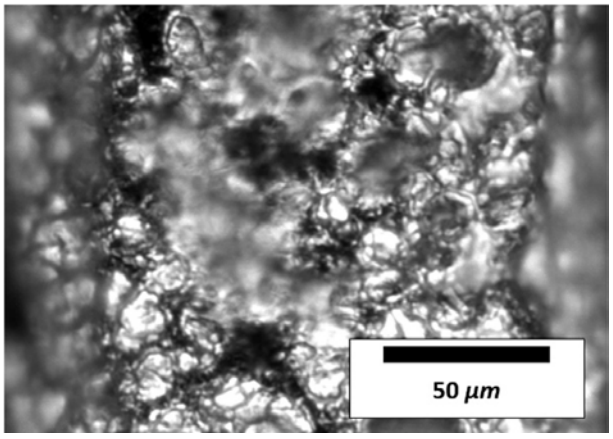

Figure 5.4: Optical microscope image of electroplated thick Cu film (opened seed layer area = 2.0241 cm^2, forward current density = 13 mA/cm^2, pulse duty cycle = 80 % with 1 kHz frequency, electroplating time = 18 h, and thickness = 20 µm).

5.3 Fabrication of the Serpentine Spring Lorentz Actuator

The serpentine springs were fabricated on the thin membrane together with a thick crossbar using the KOH bulk-micromachining technique. The devices were fabricated at the NSFL, and a <100> orientation silicon wafer was selected as a device substrate. Five optically transparency e-beam masks provided by the nanoFab lab were used to transfer the designed patterns onto the substrate. This section presents the fabrication process used to build the actuator. More details of each process can be found elsewhere in literature [31,35,65,66,87]

5.3.1 Mask preparation

According to the design, modeling and simulation study, the serpentine spring Lorentz actuator array is formed using three different height structures of serpentine springs, crossbars, and pillars. A total of six transparent masks were used to fabricate the device. Three masks were used to form each different height structure. A thick photoresist was needed to pattern thick structures such as crossbars and pillars (total ~ 30 μm thickness with 8 μm pillar and ~ 20 μm crossbar). An edge bead removal mask was prepared to remove the edge bead that forms around the wafer formed as a result of thick photoresist spin coating. The edge bead is formed during spin coating due to high viscosity of the photoresist. This edge bead prevents intimate contact between the mask and wafer, which reduces image resolution in the contact lithography process that was used. Lastly, a mask for stripping the conductive film on the actuator structure was prepared. Tanner L-Edit software was used to design the lithography masks.

Figure 5.5 shows the mask design used in the different fabrication stages. For each mask design, the mask dimensions were calculated according to the process parameters. Two masks fabricated by e-beam used for the actuator and Al/SU-8/Al mirror fabrication are presented in Figure 5.6. To optimize the lithography mask, a 5” wafer size transparent glass substrate was selected. All patterns labeled with M-

series were prepared for the Al/SU-8/Al mirror fabrication. The # 6 mirror align & contact mask was prepared to align and bond the fabricated Al/SU-8/Al mirror substrate to the actuator substrate.

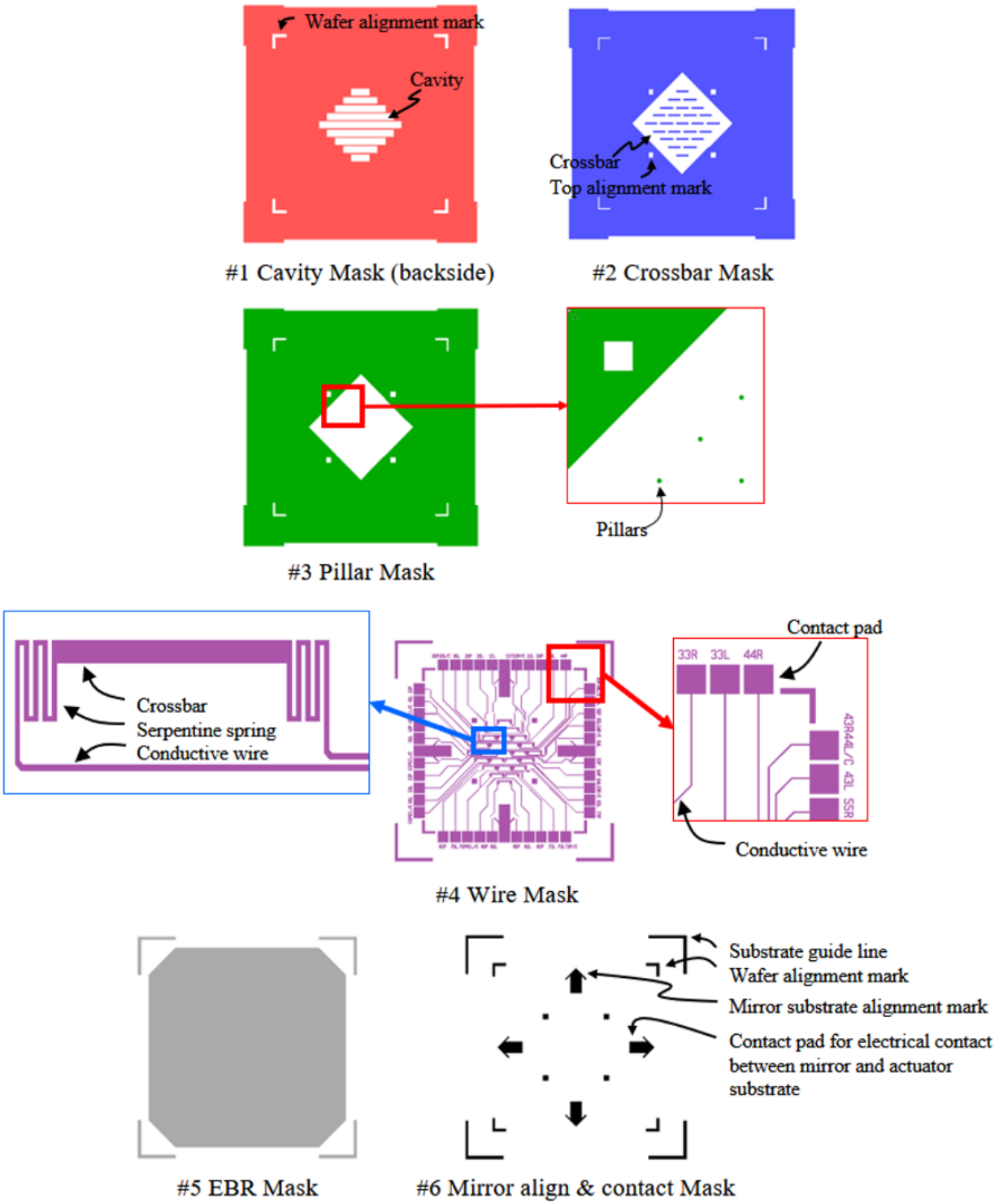

Figure 5.5: Lithography mask usage in different stages of fabrication.

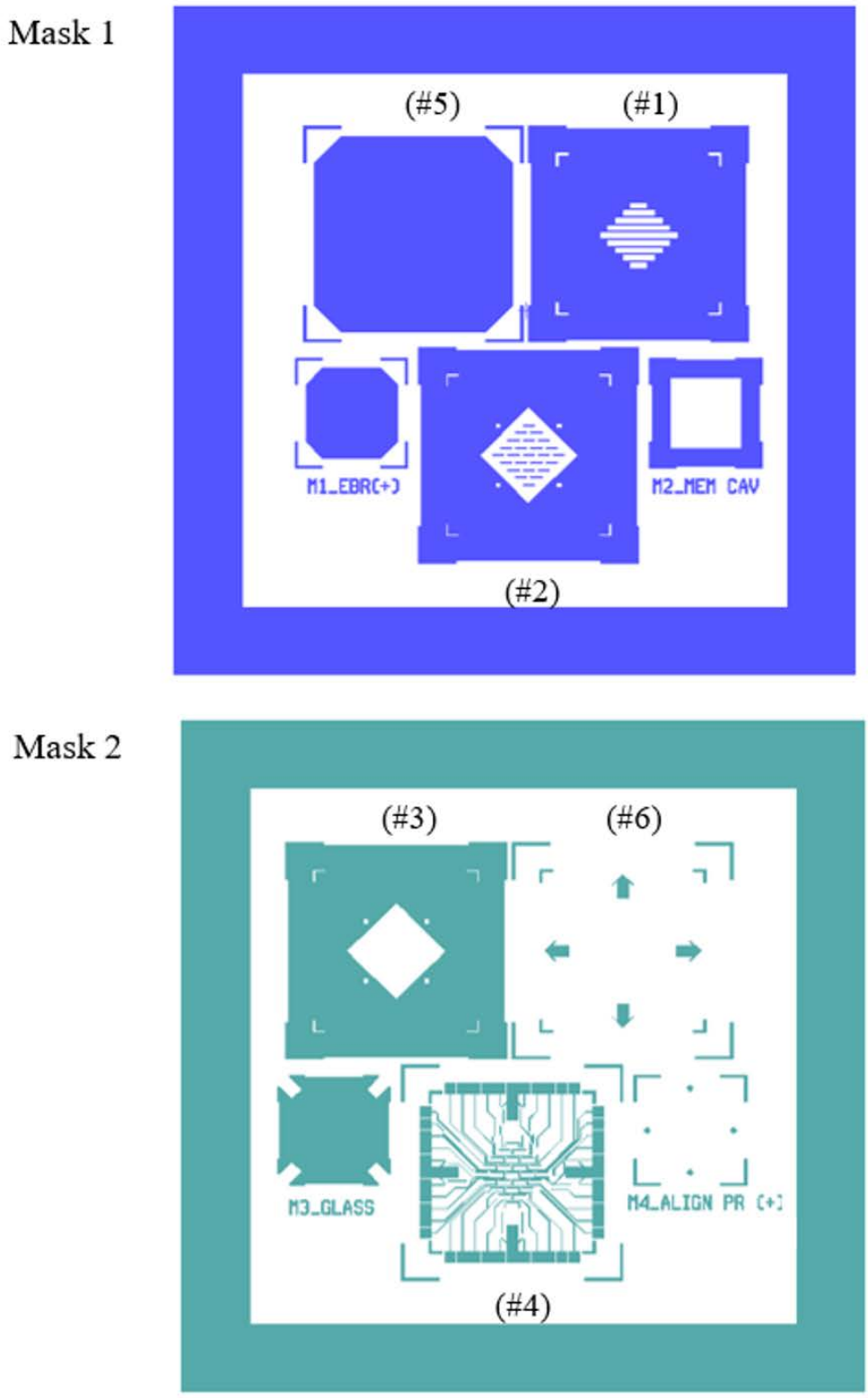

Figure 5.6: Lithography mask design used for actuator fabrication. M-series pattern is prepared for Al/SU-8/Al mirror fabrication.

5.3.2 Fabrication Process

Various techniques were investigated to fabricate the actuators. According to the design in Figure 4.14, the actuator consists of three different thicknesses of the structure such as a pillar, crossbar, and serpentine spring. The total thickness of the crossbar and pillar on the serpentine spring is about 30 µm (8 µm thick pillar and ~ 20 µm thick crossbar). A conformal coating of a conductive film (Al) was therefore required to apply current to the device in order to obtain a Lorentz force. Thus, the most commonly used anisotropic chemical etchants such as potassium hydroxide (KOH), an aqueous solution of ethylenediamine and pyrocatechol (EDP), and tetramethylammonium hydroxide (TMAH) can be used to fabricate the device. These etchants provide a gentle slope of 54.7 degrees on the <100> orientation silicon wafer surface. This facilitates a conformal film coating due to the different etch rate characteristics depending on the crystal orientation.

In this research, one of the most commonly used KOH etchants is used for the bulk-micromachining process. The KOH is much less dangerous, easy to handle, readily available, and etches faster than other etchants. However, the wafer requires proper cleaning after the KOH process because the process leaves K^+ ions on the surface, making it incompatible with other fabrication processes. The etch rate of KOH relative to the crystal orientation of the silicon substrate is approximately <110> : <100> : <111> = 600 : 400 : 1. On the contrary, EDP is not easy to handle due to its toxicity, and the solution degrades upon contact with oxygen. TMAH is not toxic like EDP or inflammable like hydrazine, but it reacts with CO_2 to a certain extent, so etching vessels should not be left open for a long time [65].

The fabrication steps and the mask used for the actuator array are described in Figure 5.7. A 300 µm thick <100> orientation double side polished silicon wafer was sculptured in a bulk micromachining process using a high uniformity KOH etch process.

A 1.5 µm thick wet thermal oxide was grown on both sides of the silicon substrate to be used as the KOH etch mask (Figure 5.7(a)). Openings were made in the backside oxide layer in the actuator locations using a 10:1 buffered oxide etchant (BOE). Exposed silicon was etched in 30 % KOH at 80 °C

with 300 rpm magnetic stirring until a 48 μm silicon membrane remains (Figure 5.7(b)). The uniformity of the etch was evenly controlled within a tolerance of ± 0.25 μm by rotating the substrate regularly during the KOH etch. The oxide on the wafer was then stripped away in a 10:1 BOE solution, and then a new 1 μm wet oxide was grown. Openings in the new oxide on the front side of the wafer in the serpentine spring location were made, followed by a 26 μm deep KOH etch (Figure 5.7(c)). Openings in the new oxide were then made in the crossbar location, but not in the location of the central pillar. This was then followed by an 8 μm KOH etch (Figure 5.7(d)). After this etch, the silicon thickness in the serpentine spring location was 14 μm, 40 μm in the crossbar location, and 48 μm at the pillar.

All oxide was then removed in a 10:1 BOE solution, followed by growing a 100 nm thick wet oxide (Figure 5.7(e)). The front side was then coated with a 25 nm titanium adhesion layer and 1.0 μm thick aluminum, 25 nm thick titanium adhesion by DC sputtering, and 650 nm oxide insulation layer by RF sputtering. The oxide and metal were patterned to form the current carrying wire.

To further thin the actuators, the backside of the wafer was etched 9 μm using a Trion Phantom II ICP-RIE etcher. Process gasses flowed 17 sccm CHF_3, 15 sccm SF_6, and 6 sccm O_2, at 60 mTorr pressure, using 200 W ICP and 140 W RIE powers. The silicon etch rate was 0.13 μm / min. Finally, the actuators were released using a front side isotropic plasma etch. The serpentine springs and crossbar were protected by the photoresist. The etch process used 60 sccm SF_6 flow at 300 mTorr, and 200 W ICP and 60 W RIE powers. The photoresist etch mask was then removed by an O_2 plasma (Figure 5.7(f)). The photograph of the released 5 × 5 arrays of actuators through the KOH bulk-micromachining process is shown in Figure 5.8.

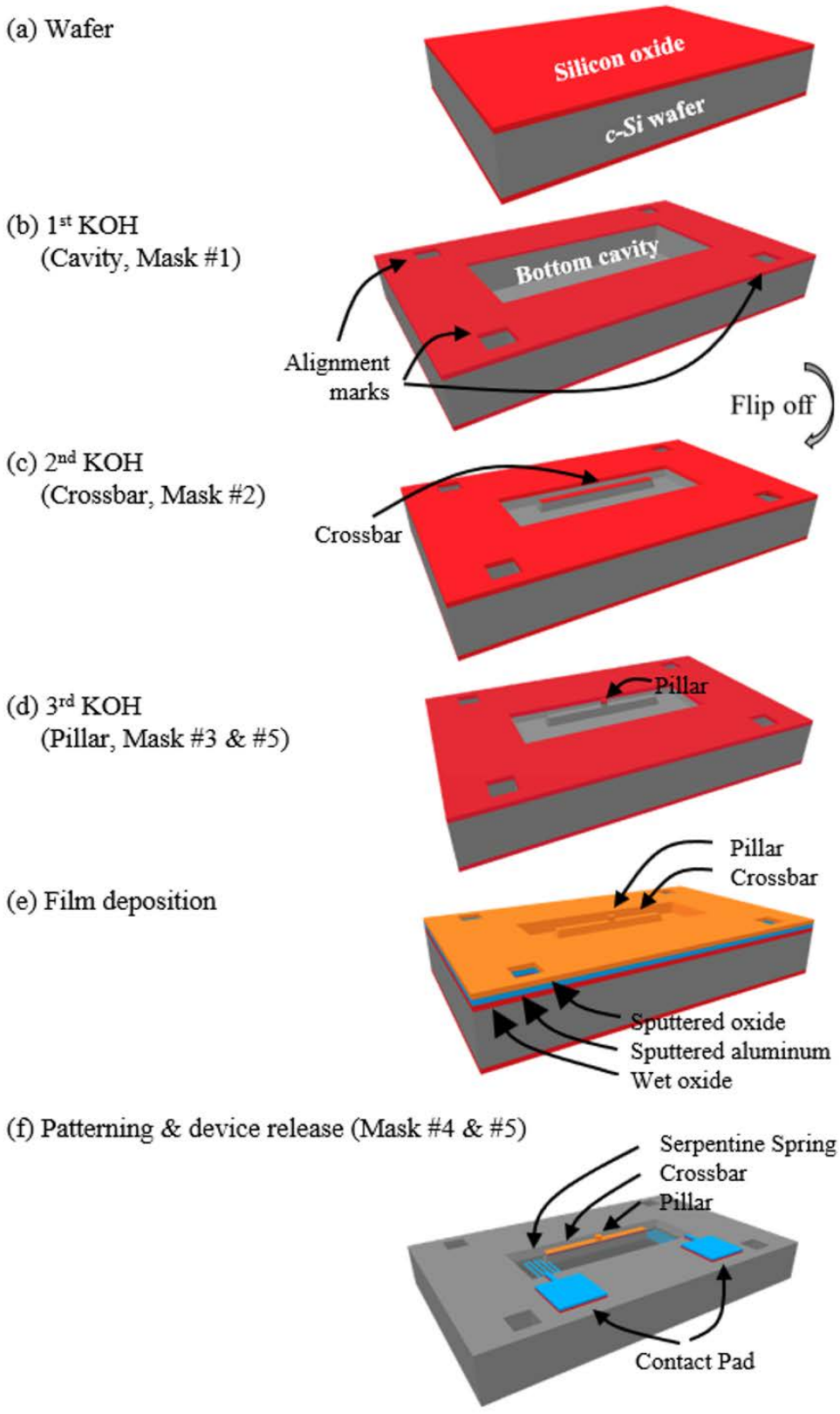

Figure 5.7: Complete fabrication process steps of serpentine spring actuators.

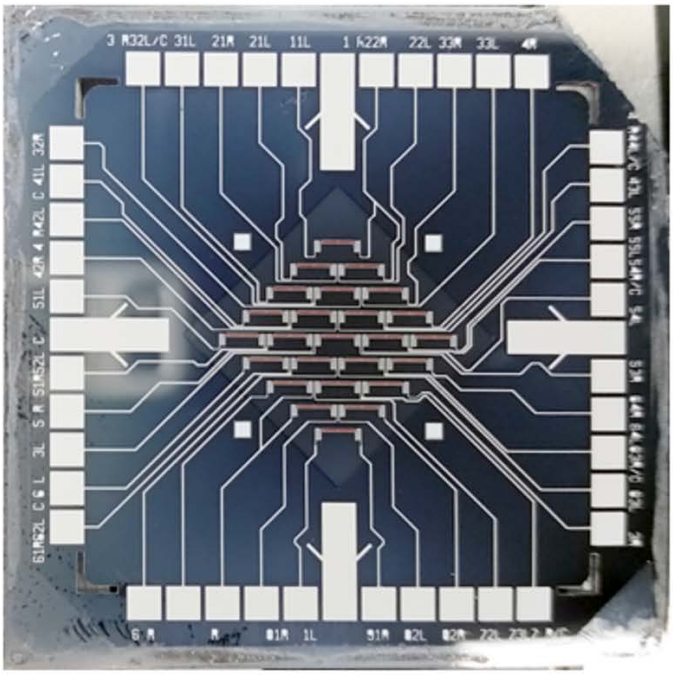

(a) Front side view

(b) Back side view

Figure 5.8: Photograph of fabricated 5 × 5 actuator array. (a) Front side view of actuator substrate and (b) Back side view of actuators.

5.3.3 Fabrication Trials

It should be mentioned, that several trials were performed to develop the actuator fabrication process.

- Trial #1

  Issued process: First KOH etch in Figure 5.7(b).

  Problem: Broken oxide pattern due to damaged photoresist. The photoresist is damaged when opening the oxide for the 1st KOH etch mask due to long 10:1 BOE etch time.

  Cause: When the HPR 504 photoresist is immersed in the 10:1 BOE solution for over 25 min, the photoresist film is swollen, and hydrofluoric acid (HF) penetrates between the photoresist and the silicon wafer. As a result, the photoresist film is delaminated, and the oxide pattern is damaged (see Figure 5.9(a)).

  Solution: A 200 nm Cr layer is deposited by DC sputtering as a 10:1 BOE mask for patterning the oxide. Figure 5.9(b) shows a well-defined oxide pattern.

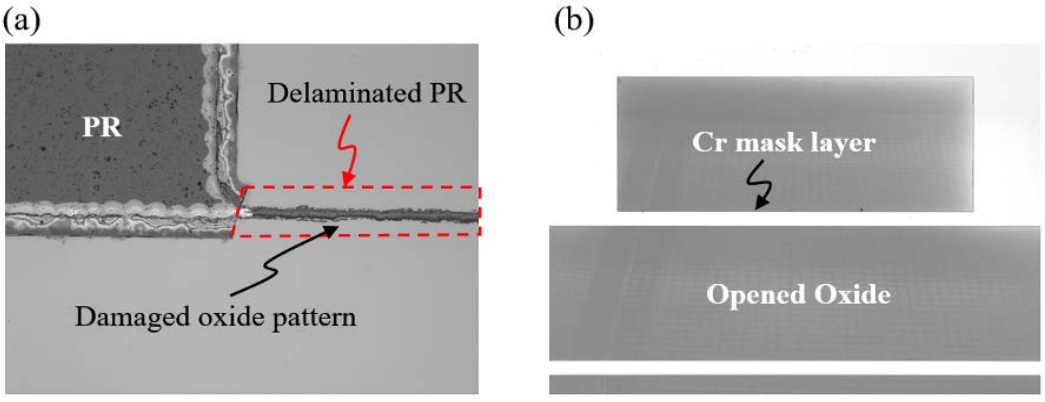

Figure 5.9: Microscope image of (a) the damaged pattern and (b) well-defined oxide pattern with Cr mask after 10:1 BOE etching.

- Trial #2

  Issued process: First KOH etch in Figure 5.7(b).

  Problem: Uneven and rough surface after KOH etch.

Cause: Non-uniform KOH concentration around the etching surface as the etching progressed (see Figure 5.10(a)).

Solution: Regular rotation of the substrate during the process (see Figure 5.10(b & c)).

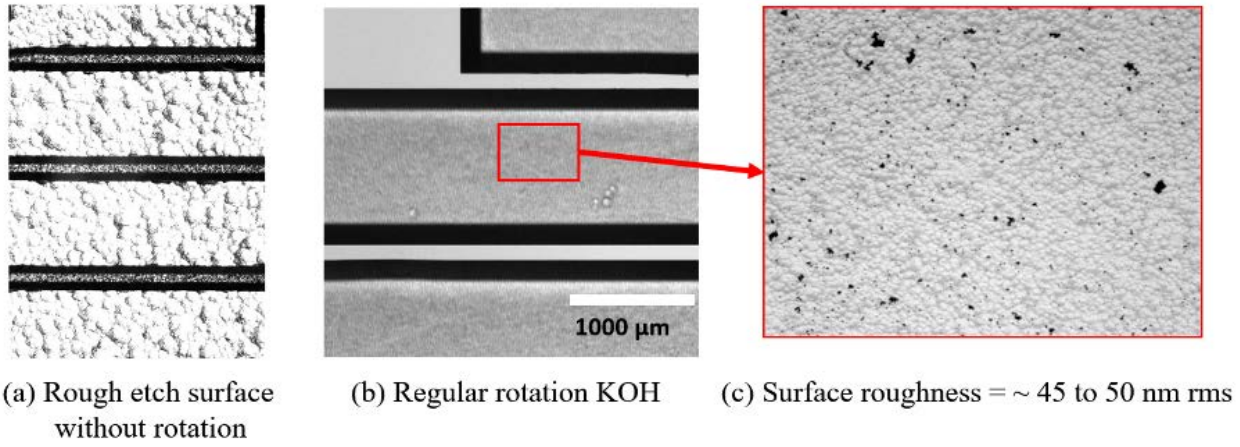

Figure 5.10: Microscope image of (a) rough surface after KOH wet etching, (b) uniformly etched surface with regular substrate rotation, and (c) 50 times magnified microscope image of the etched surface with a surface roughness of 45 to 50 nm RMS measured by an Alpha Step 500 surface profiler.

- Trial #3

Issued process: Second KOH etch in Figure 5.7(c).

Problem: Damaged substrate after KOH process (see Figure 5.11).

Cause: Scratches on the oxide film caused by metal tweezers.

Solution: Replace all metal tweezers with Teflon tweezers.

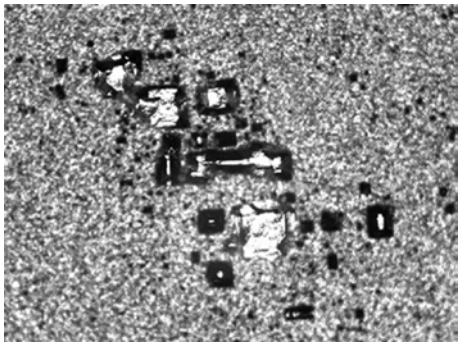

Figure 5.11: Damaged substrate after KOH process by metal tweezers.

- Trial #4

  Issued process: Second KOH etch in Figure 5.7(c).

  Problem: Imperfect alignment between both sides of the silicon substrate.

  Cause: Low infrared transmittance due to the thick residual silicon membrane during the alignment process.

  Solution: Plasma etching of residual silicon around alignment mark using blue tape as an etch mask (see Figure 5.12).

  [Trion plasma etching parameters]

  - ICP power = 100 W
  - RIE power = 60 W
  - Working Pressure = 140 mTorr
  - Gas feeding rate: SF_6 = 40 sccm, O_2 = 6 sccm, and CHF_3 = 17 sccm

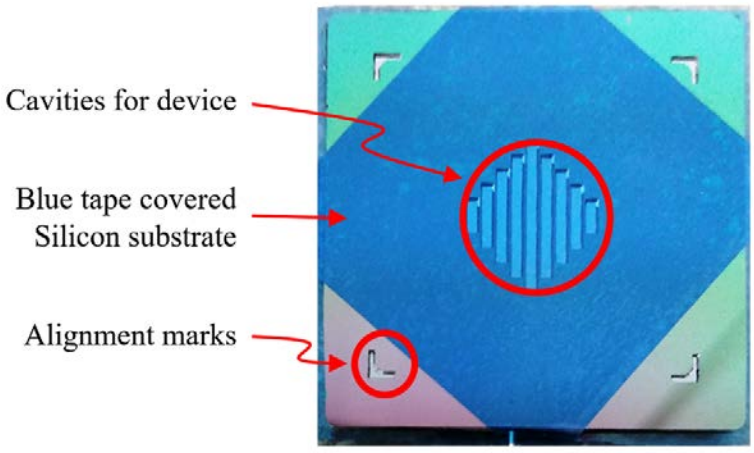

Figure 5.12: Photo of a silicon substrate selectively covered with blue tape for plasma etching process of alignment marks.

- Trial #5

  Issued process: Third KOH etch in Figure 5.7(d).

  Problem: Inhomogeneous or not fully covered photoresist.

Cause: A crossbar structure with a thickness of over 20 µm formed after the second KOH process disturbs an even photoresist coating.

Solution: Development of a uniform and thick SPR 220-7 photoresist coating process. Figure 5.13 shows a developed lithography process. The photoresist is conformally coated on the substrate, and a 5 µm thick circular shape photoresist structure for the pillar is well patterned through UV exposure for 20 seconds. The photoresist is developed for 180 sec.

[Lithography process]

1) Spin coating: SPR 220-7 at 1000 rpm for 40 sec.
2) Soft bake: 90 °C for 1 min. proximity and 6 min. contact.
3) EBR: UV exposure for 200 sec and development for 4 min using a MICROPOSITTM 354 solution. No hard baking was done due to pattern distortion.

UV exposure time (sec.)	10	20	25
Developing time (sec.)	120	120	180
Results			
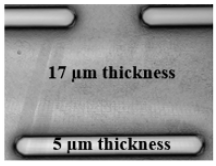	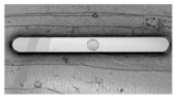	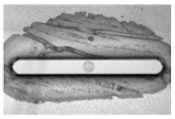	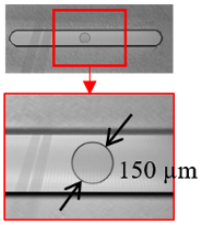
After soft baking	No pattern	PR remains around crossbar	Well developed

Figure 5.13: Developed lithography process with SPR 220-7 photoresist. A 5 µm thickness photoresist is patterned on the crossbar for the pillar after UV exposure for 25 seconds and 180 second development time.

- Trial #6

  Issued process: Third KOH etch in Figure 5.7(d).

  Problem: Cracks on the SPR 220-7 photoresist film (see Figure 5.14(a)).

  Cause: The different thermal expansion coefficients of the photoresist and silicon substrate can lead to stress cracks in the photoresist film, especially in the case of thick photoresist films. The cracking can be suppressed by slow cooling.

  Solution: Thermal shock induced cracks were suppressed by a slow cooling process using a glass with a high heat capacity. Figure 5.14(b) shows that the sample cooled slowly as the thermal mass increases.

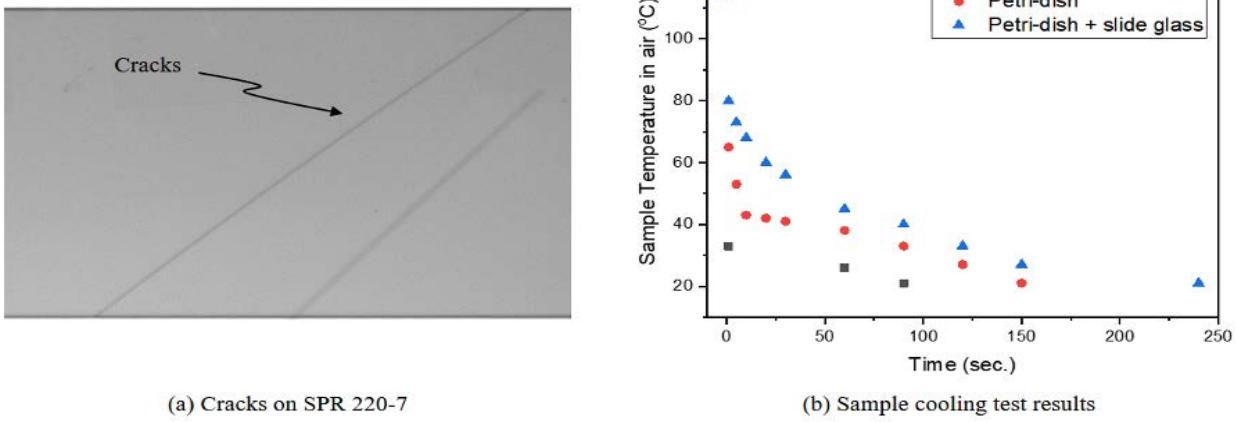

(a) Cracks on SPR 220-7 (b) Sample cooling test results

Figure 5.14: Microscope image of cracks on spin-coated 17 µm thick SPR 220-7 (A) and the temperature profile of the sample in the cooling process as a function of thermal mass.

- Trial #7

  Issued process: Patterning & device release in Figure 5.7(f).

  Problem: Developed photoresist pattern is 30 – 40 % thinner than the mask design.

  Cause: The conductive wire pattern was formed on the bottom surface of the front side cavity that was ~ 30 µm deeper than the substrate surface. Therefore, the developed pattern after lithography using the contact mask alignment method became narrow

due to refraction and/or diffraction of the UV light in the gap between the mask and substrate. This is shown in Figure 5.15.

Solution: The pattern width of the conductive wire was expanded using a mask transfer process in the NSFL. The mask transfer process is illustrated in Appendix D.

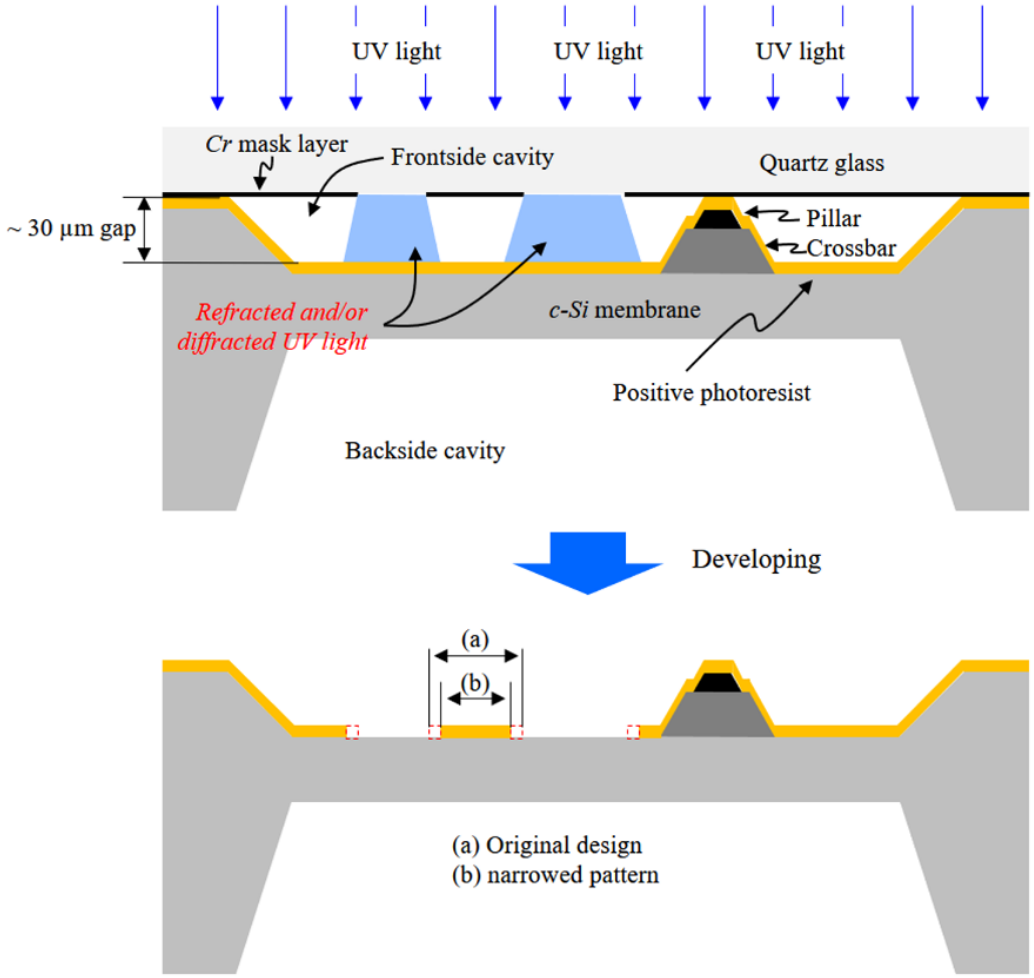

Figure 5.15: Illustration of a narrowed photoresist pattern (bottom image) by refraction and/or diffraction of the UV light due to the gap between mask and substrate (top image).

- Trial #8

Issued process: Patterning & device release in Figure 5.7(f).

Problem: Al_xO_y is left around the serpentine spring formed during the sputtering process (see Figure 5.16(b)).

Cause: Some aluminum oxide may be formed on the substrate during the sequential Al and silicon oxide sputter deposition process at relatively low vacuum (~ 10^{-2} Torr).

Solution: The oxide residues are removed using a 10:1 BOE etch. The oxide removal process is described in Figure 5.16 with a microscope image.

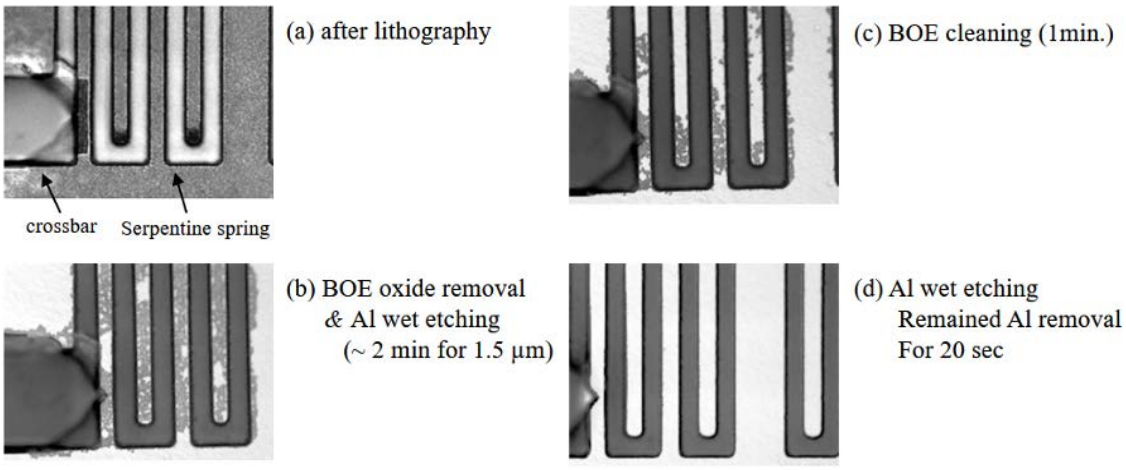

Figure 5.16: Microscope images show the oxide removal process around a serpentine spring.

- Trial #9

Issued process: Patterning & device release in Figure 5.7(g).

Problem: Uneven serpentine spring thickness due to the trenches around the joints of the spring and the anchor rail, and the resulting non-uniformly deflected actuators (see Figure 5.17(a & b)).

Cause: In an RIE plasma etching process, accelerated ions and reactive ions in the plasma erode the substrate mechanically (ion milling in low pressure and high power etching conditions) and/or chemically (reactive ion etching in high pressure and low power etching conditions). However, in process conditions where ion milling is dominant, the erosion rate is increased at the edges of the pattern (trenching, see Figure 5.17(b)). It usually occurs when the side walls of the pattern are tapered at a steep angle

formed after KOH etching. Some of the low-angle ions are reflected from the tapered surface towards the edge of the pattern, where they cause trenches [66].

Solution: The parameters of the reactive ion etching process are chosen to achieve a suitable etch rate and to flat etch the surface. An etch mask is prepared using Oxford's Micro Achining System. The method of fabricating the etch mask is shown in Appendix E. The selected etching parameters are shown in section 5.3.3. No trenches are observed in the newly developed etching process as shown in Figure 5.17(c).

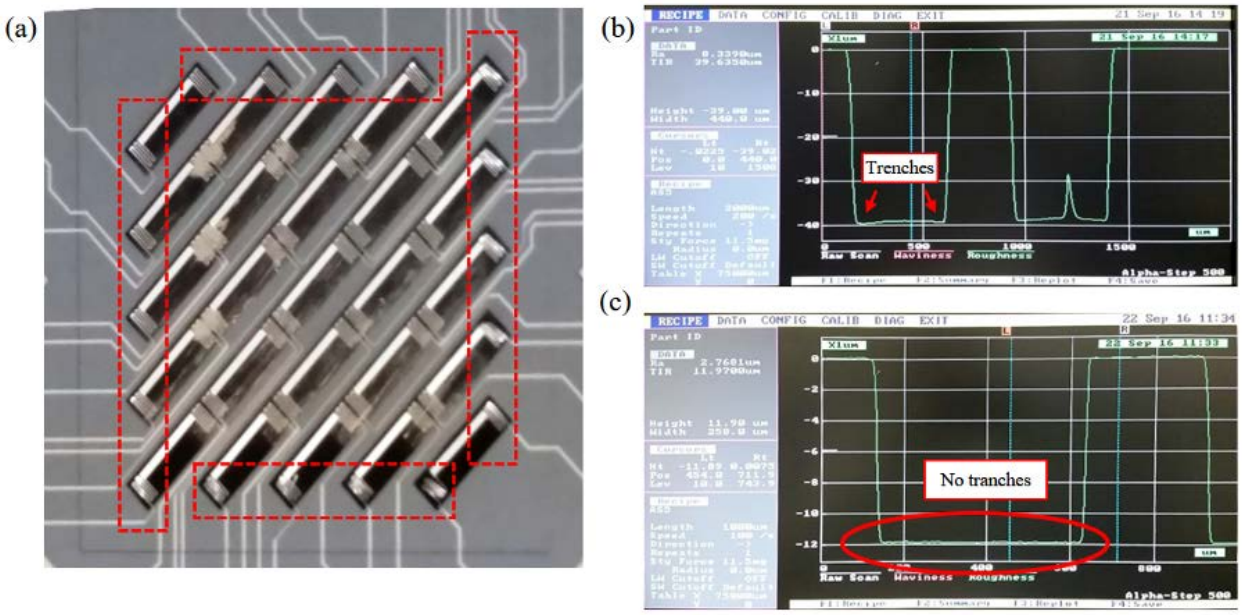

Figure 5.17: (a) Microscope images of distorted serpentine springs at the edge of the cavity. Results of the Alpha-step profiler in (b) and (c) shows trenches and a flat surface after etching (at the backside substrate), respectively.

6

Experiments

Contents

6.1 Introduction

Only the performance of the serpentine spring Lorentz actuator was tested because the cantilever arms of Lorentz actuator failed to fabricate as described in section 5.2.3. The structure and working principle are shown again in Figure 6.1 to assist in explanation of the experimental results. Four different procedures will be discussed in this chapter. First, the magnetic flux of the permanent magnet used to generate a Lorentz force with the applied current on the crossbar was mapped precisely in section 6.2. Second, section 6.3 will discuss how the fabricated serpentine spring actuator was placed on a magnet,

and how the actuator displacement as a function of the applied current was measured. Section 6.4 will discuss how the actuator and mirror substrate are bonded together and examined for the static and dynamic performance of the Lorentz DM system. The measurement results will be compared with the simulation and modeling results. The measurement setup used in each section will also be described. The actuators evaluated in section 6.3 were not reused in the Lorentz DM device due to some damage and contamination by dust during the measurement. Thus, the 5 × 5 serpentine spring Lorentz actuator array was fabricated again. In sections 6.3 and 6.4, the distance between the actuator and magnet were 1.6 mm and 3 mm, respectively. Therefore, the magnetic fields used in both devices were 0.48 Tesla and 0.35 Tesla respectively. In section 6.5, the fabricated Lorentz DM has been compared and discussed with several major actuators and various DM systems reported in the literature.

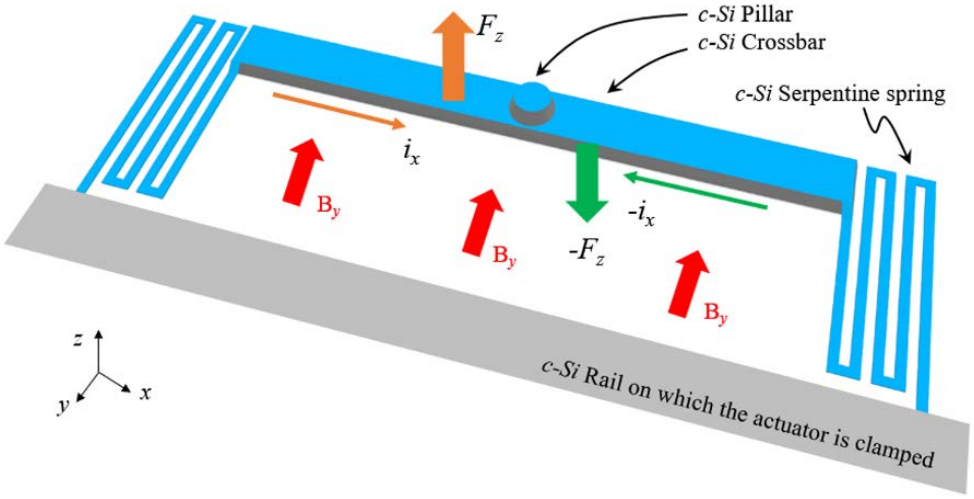

Figure 6.1: Illustration of a c-Si serpentine spring Lorentz actuator design and its working principle.

6.2 Magnetic Field Mapping

A permanent magnet was used in the experiment. The magnetic field to create the Lorentz force on the crossbar was provided by a Neodymium-Iron-Boron based ND-50 permanent magnet with a maximum magnetic field strength of 1.4 Tesla. According to Coulomb's law, the magnetic force is inversely proportional to the distance (d_z) squared ($F \propto 1/d_z^2$). Therefore, the magnetic field at various

distances above the permanent magnet was measured to investigate the precise performance of the actuator. Further, to obtain the maximum magnetic force, the actuator was placed at the centre of the magnet.

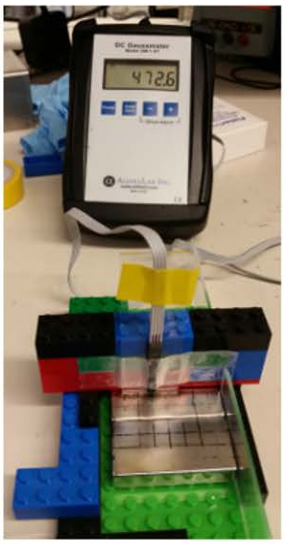

(a) Measurement

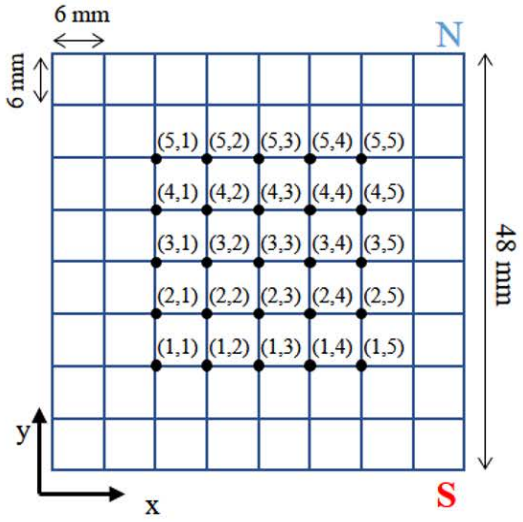

(b) Cartesian coordinate system on the magnet

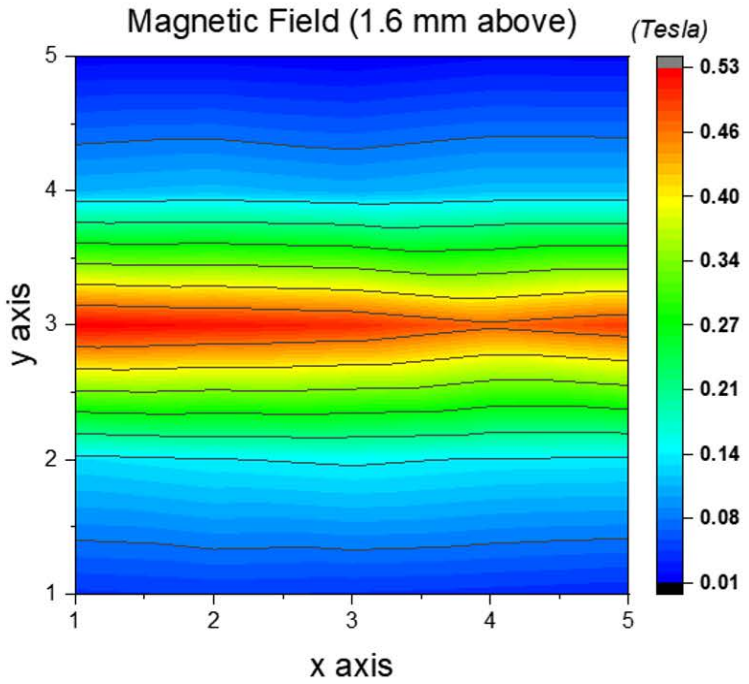

(c) Measured magnetic field strength map at 1.6 mm above the magnet

Figure 6.2: (a) Measurement set-up for mapping of the magnetic field of the ND-50 by using the AlphaLab GM1-ST gauss meter, (b) Cartesian coordinate system on the magnet. (c) The measured magnetic field (1 Tesla =10,000 Gauss) at 1.6 mm above the magnet.

Figure 6.2 shows the measurement set-up and strength of the incident magnetic field of the ND-50 permanent magnet (48 mm width × 10 mm thickness). For consistency between measurements, the receiver part of the gaussmeter (AlphaLab GM1-ST) was adhesively attached to a long and rigid Lego block bridge. The magnetic field was varied by moving the magnet to different coordinates shown in Figure 6.2(b). Also, the height of the sensor receiver was changed from 0.6 mm to 4.6 mm with 1 mm gaps to achieve a 3D magnetic field map. Figure 6.2(c) shows a 2D slice of the magnetic field 1.6 mm above the permanent magnet. The magnetic field strength used in the measurement depends on the distance between the elements and permanent magnet, which is 0.48 Tesla at 1.6 mm height for actuator deflection and 0.35 Tesla at 3 mm height for mirror deformation. The measured magnetic field at all the different distances (heights) are shown in Appendix F. It should be mentioned that a solenoid magnet could also be used to control the magnetic field strength.

6.3 Actuator Displacement

Four versions of the serpentine spring Lorentz actuator were fabricated in Chapter 5, relating to cases A-D. Case A was 4.5 μm (thickness) × 24 μm (width), Case B was 5 μm × 29 μm, Case C was 5.5 μm × 29 μm, and Case D was 6.5 μm × 28 μm. The physical dimensions of the released actuators were measured using an Olympus BX51 microscope with 1000x magnification. The measurement accuracy of this method is ~ 0.5 μm in z axis, as the depth of focus of this lens is 0.42 μm. Figure 6.3 shows the fabricated actuator and its dimensions relative to cases A to D.

The experimental setup used to measure the static movement of the actuator is shown in Figure 6.4. A 0.48 Tesla magnetic field was provided by an ND-50 permanent magnet 1.6 mm above the actuator array. The measurement (dotted line) and the COMSOL simulation (bold line) results for the actuator deflection as a function of current are shown in Figure 6.5. The measured and simulated actuator deflections are in very good agreement. We can see all actuators showing a linear deflection response with actuator current. Large deflection was possible, with the total deflection of the actuator for Case A of

~ 300 µm with an applied current of ± 14.7 mA. The measured spring constant of each actuator was 0.1, 0.16, 0.25, and 0.4 N/m for cases A, B, C, and D, respectively. Mechanical robustness was briefly explored by driving an actuator with a sinusoidal ± 9.2 mA peak-to-peak current at a frequency of 100 Hz for 24 hours and 15 minutes. After these 8.73×10^6 oscillations at ± 90 µm deformation, no visible performance degradation was observed.

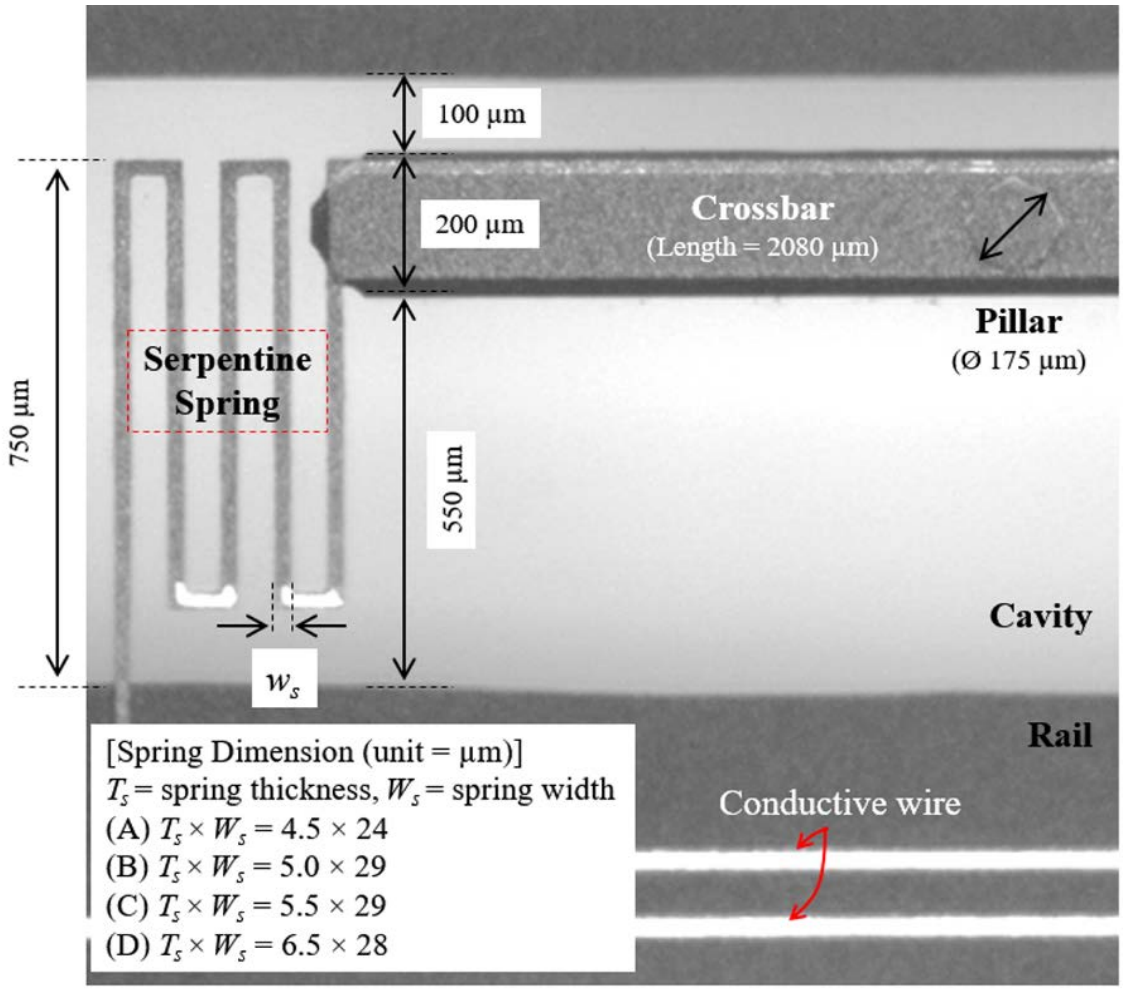

Figure 6.3: Microscope image of the fabricated serpentine spring Lorentz actuator. The dimensions of the serpentine spring are shown in the square box in the bottom left. The crossbar and pillar thicknesses are 25 µm and 8 µm, respectively. T_s and W_s are the thickness and width of the spring, respectively.

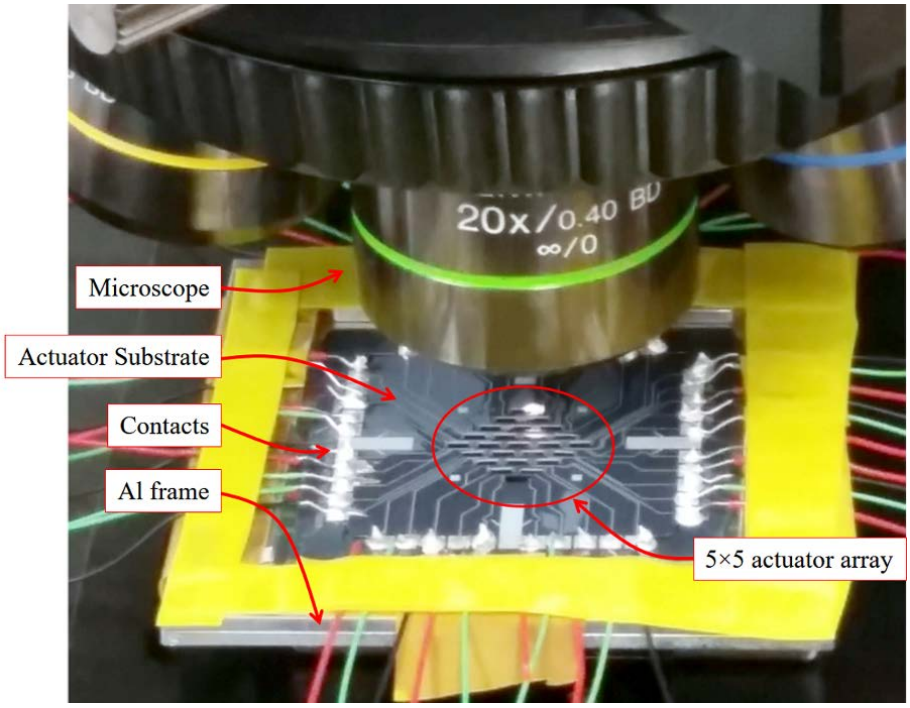

Figure 6.4: Photograph of the optical measurement set-up of a 5 × 5 actuator array with a 0.48 Tesla external magnetic field underneath the actuators. The magnet is hidden by the actuator substrate.

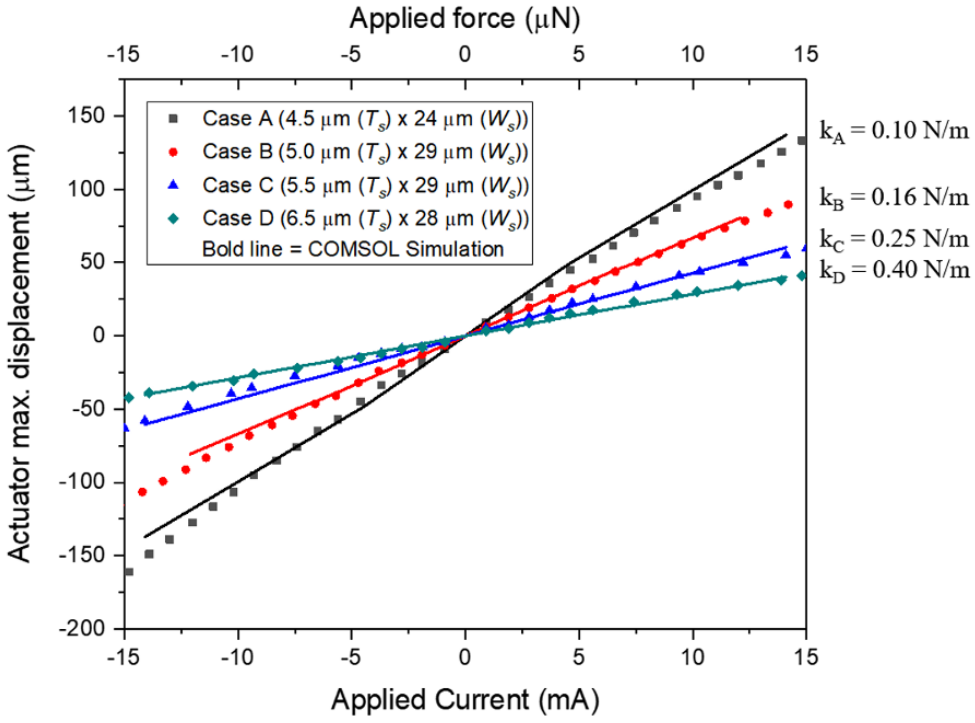

Figure 6.5: Measured (dotted line) and COMSOL simulated (bold line) crossbar deflection as a function of DC actuation current.

6.4 Mirror Deformation

6.4.1 Actuator and Mirror Bonding

The 5 × 5 actuator array was fabricated again to analyze the performance of the Lorentz DM device. The thickness of the silicon serpentine spring on both sides of the thick crossbar was thinned to 3 μm from the thinnest case A of 4.5 μm to improve the deformation stroke (spring constant = 0.06 N/m). The electrical and thermal properties of the serpentine spring were enhanced by using an 1.5 μm Al conductor that was 0.5 μm thicker than the original actuator. The resistance of the actuator coil was ~ 30 Ω, which was decreased from the device fabricated in Chapter 5 (over 80 Ω). The thickness of each actuator structure was 3 μm for each serpentine spring, 25 μm for the crossbar, and 8 μm for the pillar. The fabricated actuator and membrane substrate was bonded by silver epoxy (EPO-TEK® H20E, Epoxy Technology) at 80 °C for 3 hrs. An ABM contact mask aligner was used for aligning the actuator substrate and the Al/SU-8/Al mirror substrate. Finally, the fabricated Lorentz DM was wire-bonded in order to be able to apply current. The substrate bonding process is illustrated in Figure 6.6.

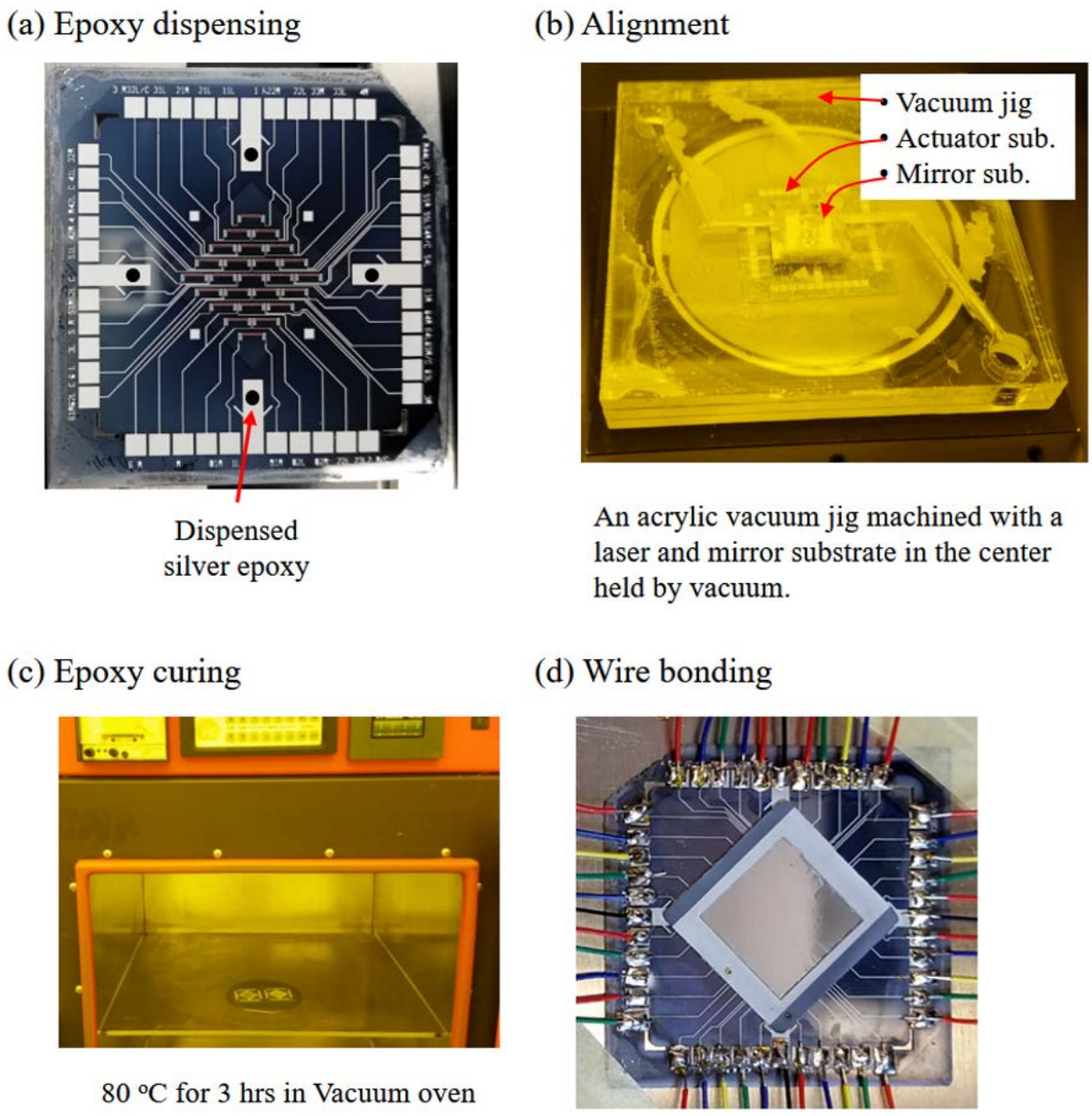

Figure 6.6: Illustration of substrate bonding process between the Al/SU-8/Al mirror substrate and the actuator substrate.

6.4.2 Static Performance of the Lorentz DM

The static performance of the Lorentz DM was characterized using a 1000 times magnification Olympus BX51 microscope with a measurement accuracy of ~ 0.5 μm. The experimental setup is shown in Figure 6.7. The amount of Al/SU-8/Al mirror deformation was obtained by measuring the movement

of the actuator using the microscope. The actuator pushes against the mirror when current flows in the i_x direction as shown in Figure 6.1. An incident magnetic field of 0.35 Tesla is provided by an ND-50 magnet located 3 mm under the actuator array. First, the actuator was brought into contact with the mirror, and this occurs over the initial 10 µm of motion. Then, the actuator was pushed further upwards, thereby deforming the mirror. Finally, the mirror deformation is measured.

The measured mirror deformation (red dotted graph) on the central actuator node as a function of Lorentz force is shown in Figure 6.8, along with the COMSOL Multiphysics simulation results (blue line). The measurement results show close agreement with the simulation. A large deformation of over 17 µm is measured at a 3 mA current.

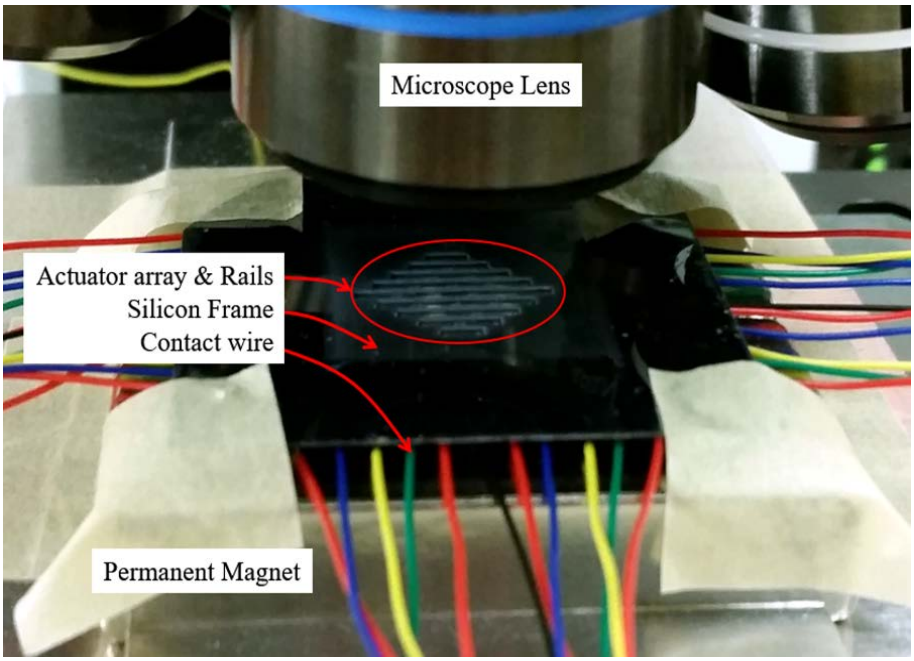

Figure 6.7: Photograph of the optical measurement set-up for deformation of a Al/SU-8/Al mirror actuated by a serpentine spring Lorentz actuator in a 0.35 Tesla external magnetic field. The Al/SU-8/Al mirror substrate is turned over for convenience during measurement.

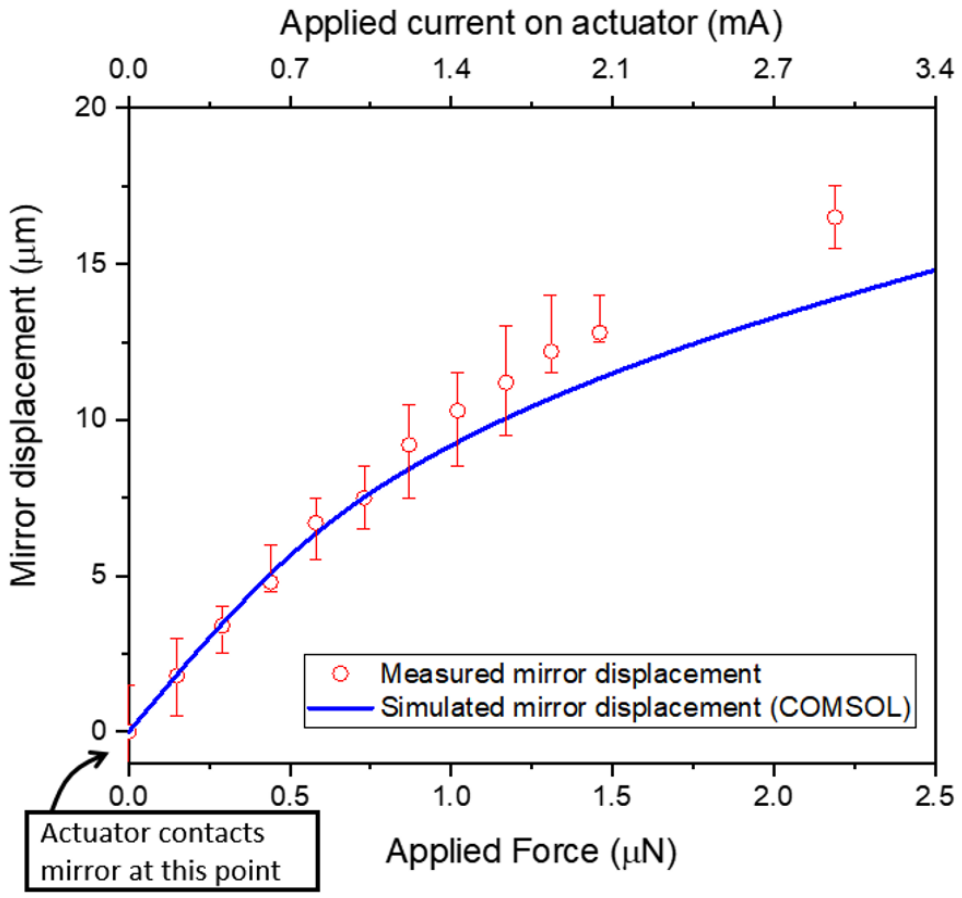

Figure 6.8: Measured and simulated mirror deformation after the actuator touched the mirror as a function of applied Lorentz force. Note that the actuator makes contact to the mirror in the centre of the mirror. Five measurements were performed at each point. The error bars are formed from the maximum, and minimum values, and the remaining three measurements result are averaged for the indicated data point. The standard deviation ranged from 0.7 to 2.5 μm.

6.4.3 Dynamic Performance of the Lorentz DM

The step response was measured using an optical positioning system in order to understand the frequency response of the Lorentz DM. Figure 6.9 shows a block diagram of the response time measurement setup. The Al/SU-8/Al mirror moved vertically as a result of the Lorentz force on the actuator. This force was generated by the current from the function generator and the incident magnetic field along the length of the crossbar. The Lorentz DM was firmly mounted on the base plate with an

adhesive. The incident magnetic field during testing was produced using ND-50 permanent magnet with a 0.35 Tesla magnetic field with dimensions of 5 cm × 5 cm × 1 cm. This magnet was located 3 mm away from the actuator.

The optical positioning system measures the mirror motion using a multicell photodiode. The laser spot is aligned to the centre of the split photodiode, and as the mirror moves, the laser spot scans over the photodiode surface. Therefore, the photodiode outputs a current proportional to the mirror motion, which is sent to a signal processing circuit. The signal processing circuit consists of a I to V (current to voltage) converter and an oscilloscope. The differential amplifier circuit has a gain of 70 dB and includes a first-order low-pass filter with a cut-off frequency of 1.6 kHz (see Figure 6.10). The circuit has a 20 μs time constant.

Figure 6.11(a) shows a photograph of the overall measurement system with a Faraday cage. The Faraday cage is made from Al and is earth grounded. The Faraday cage also ensures that external electric fields and atmospheric flow will not affect the device measurements. Furthermore, the Faraday cage is placed on a vibration isolation table to prevent motion of the mirror from external vibration. The optical positioning system consisting of a ¾-inch Al stock located in a Faraday cage is shown in Figure 6.11(b). The Al stock structure provides sufficient mass and rigidity to hold the photodetector (Advanced Photonics SD380-23-21-051) and a laser diode (PTI Technologies PM01(635-5B)G3).

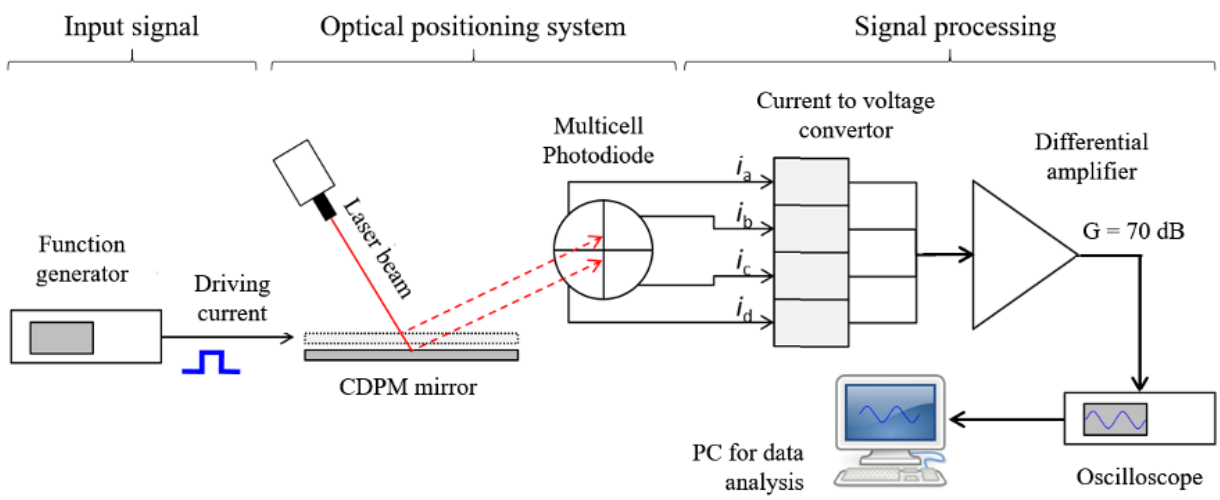

Figure 6.9: Block diagram of the Lorentz DM response time measurement setup.

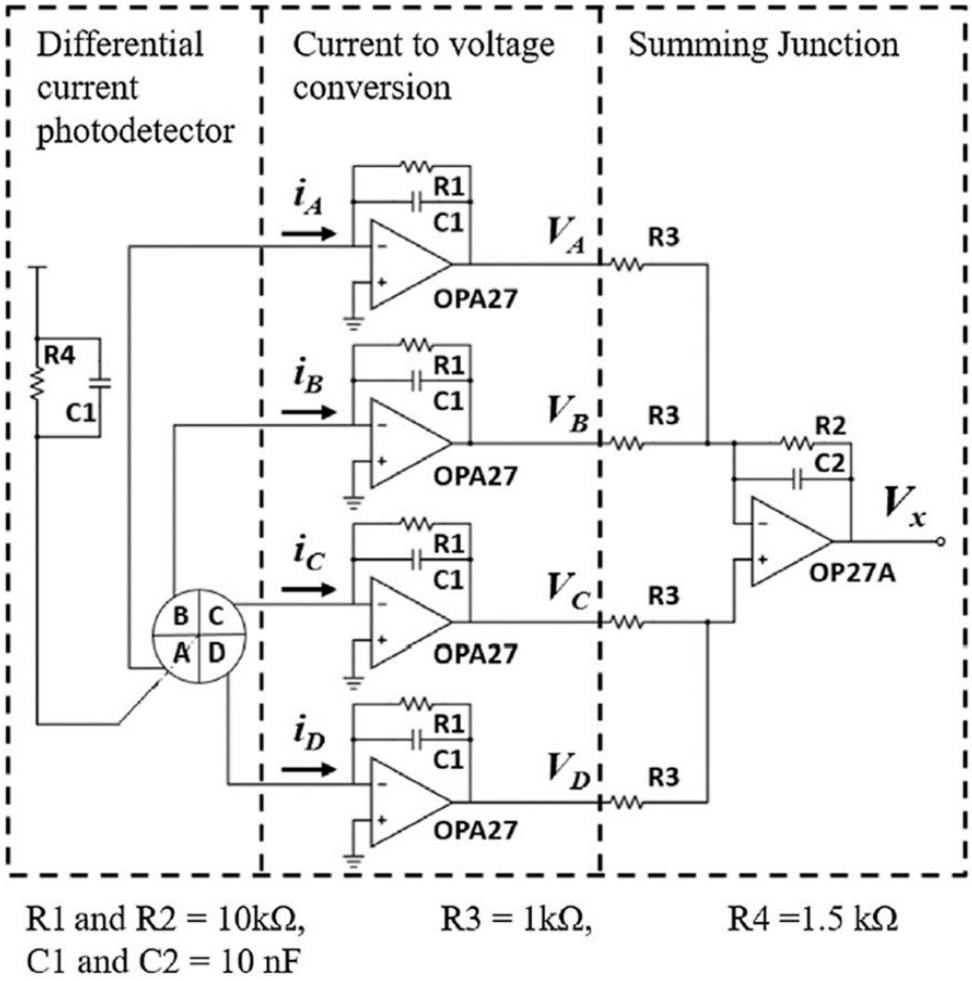

Figure 6.10: Circuit diagram of a photodiode, current to voltage converters, and summing/difference junction.

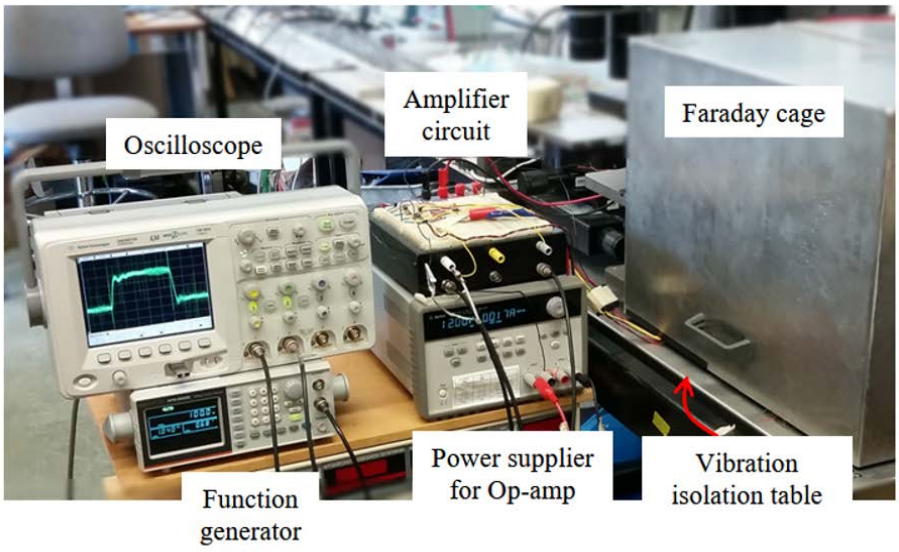

(a) Measurement setup

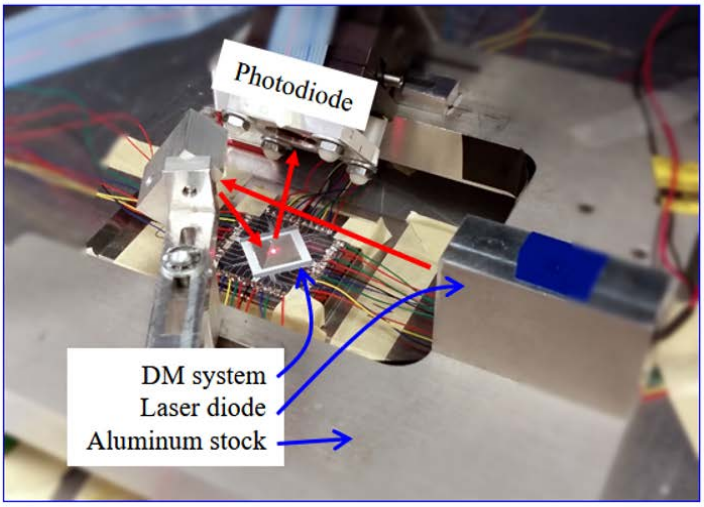

(b) Laser positioning system in the Faraday cage

Figure 6.11: (a) Photograph of the overall measurement set-up and (b) optical positioning system with the DM system and an external static magnetic field beneath the device in a Faraday cage.

Figure 6.12 shows the deformation response of the mirror to an applied step function as a function of time. This was done by having one actuator push upwards against the mirror, with all other actuators not contacting the mirror. A current of 1 mA was used to attach the actuator to the mirror. An additional force of 2 µN (3 mA) was then applied to allow the actuator to sufficiently coupled to the mirror. Further 7 µN (additional 6 mA as a step function) applied to the actuator to displace the mirror a

further 23 µm. According to the Fig. 12, the Lorentz DM has the characteristics of an underdamped 2nd order system. The relationship between natural frequency (w_n) and resonance frequency (w_r) of the mirror can be found in equation (6-1), where ζ is the damping ratio [35]. The ζ of the Lorentz DM was calculated to be 0.7 with measured natural frequency of 1.4 kHz and simulated resonance frequency of 230 Hz.

$$w_r = w_n\sqrt{1-2\zeta^2} \tag{6.1}$$

It can be observed that the membrane rises 23 µm in height in about 500 µs with very low overshoot, thus ensuring a maximum operating frequency of 2 kHz. After the rise, there is one brief 700 µs oscillation period. Therefore, this Lorentz DM can be suitable for a wide range of adaptive optics applications that require large deformation and 2 kHz driving frequency. It should be mentioned that the DM with all actuators mechanically bonded would have an even higher driving frequency because the mirror would be stiffened and mechanically loaded at each actuator contact point.

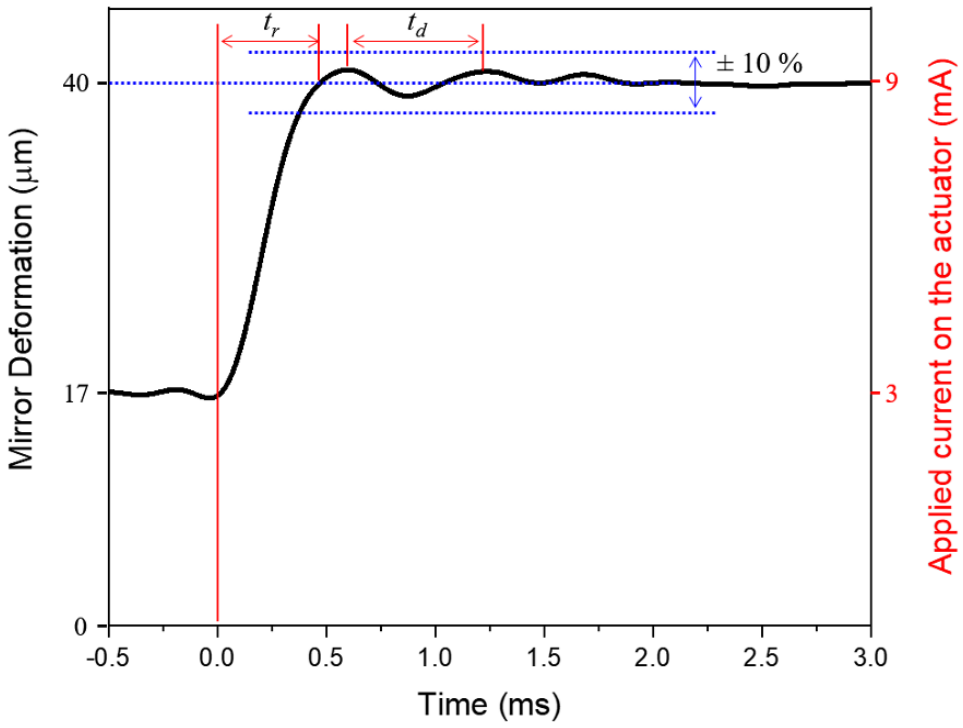

Figure 6.12: Step response of the Lorentz DM with the actuator pushing at its center. Contact is made with the mirror, and the actuator is pulsed with an additional force of 7 µN. We observe that the mirror settling time is around 2 ms, including damping. The mirror rising time (t_r) is 0.5 ms, and the period of the oscillation (t_d) is 0.7 ms.

6.5 Chapter Summary

This chapter showed that the developed serpentine spring Lorentz actuator substrate and Al/SU-8/Al mirror substrate were successfully bonded using a silver-epoxy paste. Figure 6.13 compares the merits of the demonstrated Lorentz DM using a normalized radar plot with other MEMS DMs. For more comparison, table 6.1 shows the detailed performance of various MEMS DMs.

The developed Lorentz DM exhibits overall good performance compared to other MEMS DMs. In particular, the Lorentz DM shows a relatively large stroke (17 μm) at a low voltage (0.09V) due to the low Young's modulus of polymer-based (SU-8) mirror, and larger actuator pitch compared to other MEMS DMs. Another large stroke DM reported by Lin et. Al [28] was polyimide based electrostatic DM with a stroke of 39 μm. But it required a high driving voltage of 195 V. The highest operation frequency in the table was reported 20 kHz on a PZT DM with a c-Si membrane mirror by Ma et al. [30]. However, since most of the AO applications including an earth-based telescope and retinal imaging usually operate at frequencies of less than 1 kHz, the 2 kHz operation frequency of the Lorentz DM is sufficient to be applied to many application fields. The EM-C DM (Cagat et al.) driven by a coil magnet required low voltages, but high currents of 2.5 A [32]. Consequently, the power consumption of each Lorentz DM actuator (0.3 mW for 17 μm stroke) was approximately 8000 times lower than that of the EM-C DM (2.5 W per actuator at EM-C [32]). Therefore, the demonstrated Lorentz DMs in this thesis may contribute to significant improvements in many adaptive optics applications because of their large stroke, low voltage, low operational current, as well as sufficiently high driving frequency.

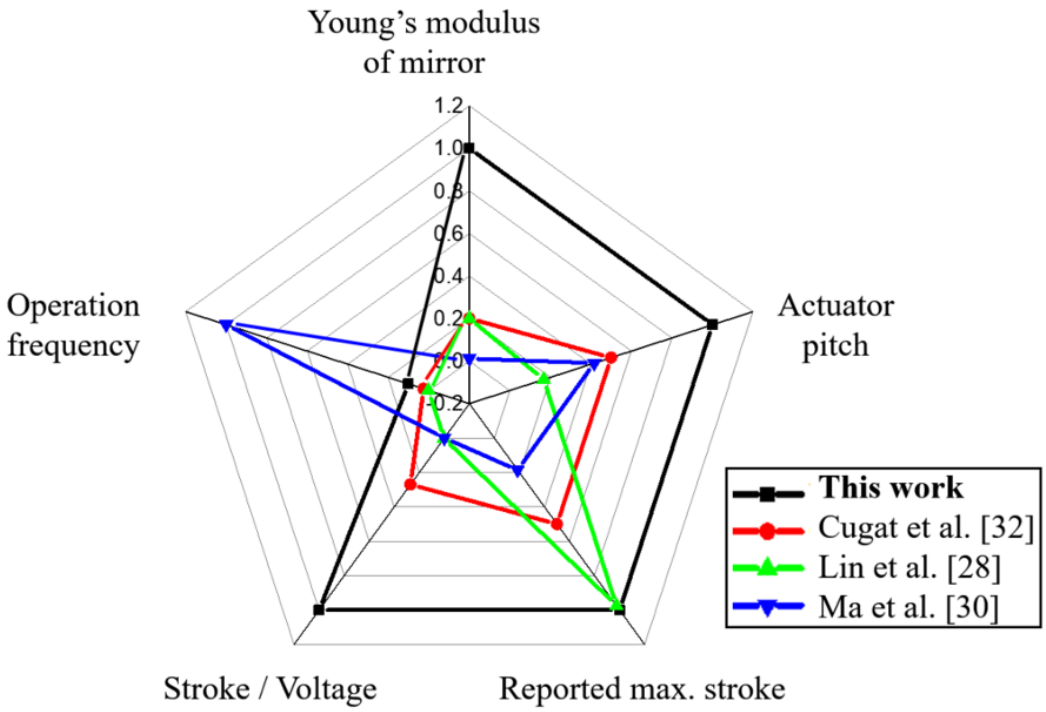

Figure 6.13: Normalized radar plot of MEMS DMs with demonstrated Lorentz DM.

Table 6.1: Summary of various MEMS deformable mirrors.

Publication	Actuation Technique	Membrane width (mm)	Membrane Young's Modulus (GPa)	Stroke (µm)	Actuation Voltage (Current)	Operation frequency (kHz)
This Work	**EM-L**	**12**	**SU-8 (2)**	**17**	**< 0.09V** (3 mA with 30 Ω)	**2**
Cugat et al. [32]	EM-C	6	polyimide (10)	20	0.5 V (2.5 A with 0.2 Ω)	0.5
Friese and Zappee [27]	ES	*	SU-8 (2)	12	220 V	*
Lin et al. [28]	ES	2	polyimide (10)	39	195 V	0.04
Fernandez et al. [26]	ES	1	gold (80)	6.4	380 V	*
Cornelissen et al. [67]	ES	0.34	Polysilicon (~ 150)	2	220 V	7.1
Perreault et al. [5]	ES	0.3	Polysilicon (~ 150)	1.9	241 V	7.1
Ma et al. [30]	PZT	5	c-Silicon (162)	7.4	100 V	20

* Data not available in the literature.
EM-L: Electromagnetic Lorentz bar actuator
EM-C: Electromagnetic coil magnet actuator
ES: Electrostatic actuator
PZT: Piezoelectric actuator

7

Bonding Technology

Contents

7.1 Introduction

This research has not solved the bonding issue between the actuator and the mirror. This can be an interesting research project for future researchers. This chapter will discuss various applicable bonding techniques and present some results from the metal fusion bonding technique performed in this thesis.

In order to enable bi-directional motion of the Lorentz DM, each pillar on the actuator has to be mechanically coupled to the Al/SU-8/Al mirror. Bi-directional mirror deformation allows for correcting high order wavefront distortion. There are a variety of bonding techniques available ranging from a covalent bond between substrates to adhesive bonds such as anodic, metal-fusion and adhesive bonding [68-82]. However, the epoxy-based SU-8 membrane used as a substrate for the Al mirror in this research

can be deformed due to thermal stress at high temperatures (thermal stability = 315 ºC at 5 % weight loss [52]). Therefore, it is necessary to develop a particular bonding technique with a reasonably low bonding temperature and sufficient bond strength. In this section, metal-fusion bonding will be discussed, and additional applicable anodic and adhesive bonding will be introduced.

The proposed and fabricated actuator is beneficial when applying the various bonding techniques listed above because the actuator can provide the heat and pressure required for the bonding process by Joule heating and Lorentz forces, respectively. Figure 7.1 shows the means by which the actuator provides the heat and pressure needed for the bonding process. The pressure to maximize the contact area in the interface between the pillar and the mirror is provided by the Lorentz force (F_L). The heat is generated on the crossbar through Joule heating. Thus, the heat produced during the bonding process is preferably restricted around the crossbar and pillar due to the localized heat source so as not to deform the mirror. An Sn (Tin), Al and adhesive layer can be used as a bonding layer for metal-fusion bonding, anodic bonding, and adhesive bonding. The required bond strength should exceed the force applied to pull the mirror. For example, if the force applied to a 175 µm diameter pillar is a maximum of 100 µN (the actual force required in the device is ~ 10 µN), the necessary bond strength must be at least 4.2 kPa.

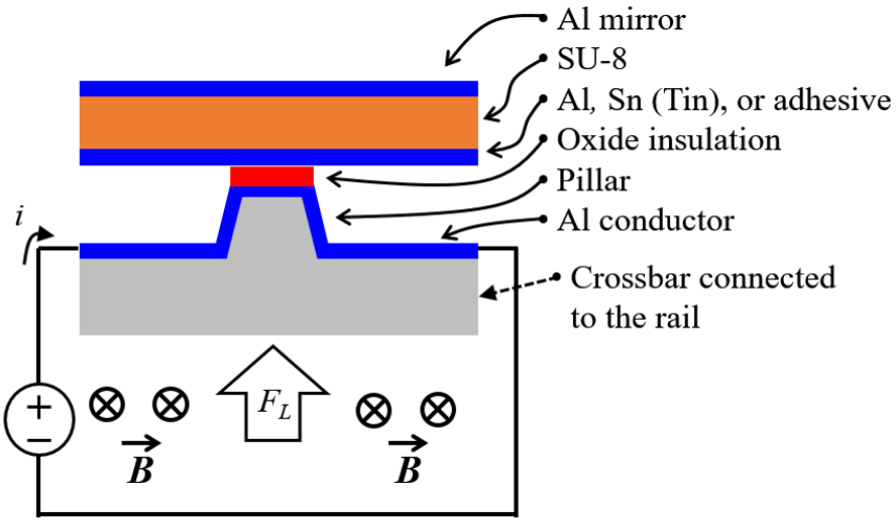

Figure 7.1: Illustration shows the bonding process of the Lorentz actuator and Al/SU-8/Al mirror. The bonding pressure is facilitated by the Lorentz force (F_L), and the heat is provided by Joule heating.

7.2 Metal-Fusion Bonding

Metal-fusion bonding is a key technology in MEMS packaging and heterogeneous integration. Metal-fusion bonding can provide short electrical and mechanical interconnections between two wafers with good thermal conductance. In particular, Al fusion bonding is convenient to apply to the device because of the inherent Al layer between the actuator and the mirror. However, Al fusion bonding requires a high bonding temperature of 450 °C, which is not suitable for the device [68]. So, the Sn (Tin) bonding is demonstrated in this research to achieve a low bonding temperature [69]. The melting point of Sn is 231.9 °C.

The Sn bonding process parameters are estimated experimentally, and a bonding process is proposed at the end of the discussion. A 4" one side polished <100> silicon wafer and a 2.5 cm × 3.7 cm slide glass were used. The wafer and the slide glass were cleaned in a piranha mixture (H_2SO_4:H_2O_2 = 4:1) for 10 minutes followed by a DI water rinse and nitrogen drying. A 340 nm thick Sn film was then evaporated onto the wafer. Afterwards, the slide glass and Sn-coated wafer were loaded into a vacuum bonding chamber with a 20 kg mass (0.2 MPa) on top of the sample. The bonding was carried out at 280 °C in a vacuum chamber at ~ 5×10^{-7} torr with a bonding pressure of 0.2 MPa for 3 minutes. All the samples were handled using only Teflon tweezers to minimize the scratches that could be created by the metal tweezers. Figure 7.2 shows the vacuum bonding system used in this experiment.

Figure 7.3 shows the temperature profile of the hot plate during the bonding process. The ramp-up time of the sample to reach 280 °C from room temperature was 13 minutes. The heater was turned off manually at the 12 min. mark to saturate the bonding temperature at 280 °C. After that, the bonding temperature of 280 °C was maintained for 3 minutes, and the chamber was filled with nitrogen gas to cool down. The cooling time required to cool down to 100 °C was 5 minutes after opening the chamber. Then, the mass and sample were unloaded using heat protector-gloves. The thermal shock to the bonding layer could be minimized through this careful sample unloading process.

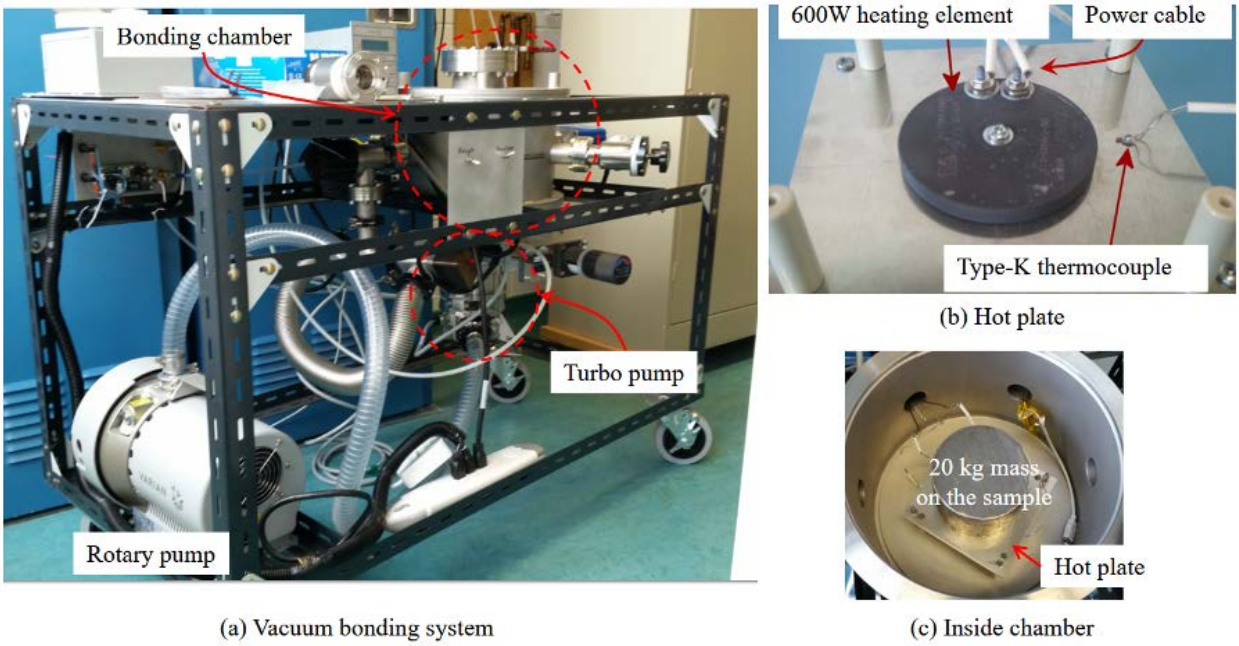

(a) Vacuum bonding system

(b) Hot plate

(c) Inside chamber

Figure 7.2: (a) Photographs of the vacuum bonding system, (b) hot plate and thermocouple, and (c) setup of the bonding chamber.

Figure 7.4 shows a photograph of the bonded sample. Note the visible diffraction rings present on the sample. The thin Al hot plate was bent due to placing a heavy weight of 20 kg on the sample as shown in Figure 7.2(c). Thus, the center area of the sample was not tightly pressurized. However, this issue can be eliminated in the actuator and the Al/SU-8/Al mirror bonding process since the pressure applied to the Al/SU-8/Al mirror surface by the pillar on the actuator is uniform.

According to [69], the bond strength ranges from 3.1 to 5.7 MPa, which is much higher than the required bond strength of 4.2 kPa. In practice, the bonding process can be simplified by removing the hot plate and the 20 kg mass because the heat and pressure can be obtained from Joule heating and the Lorentz force of the actuator, respectively.

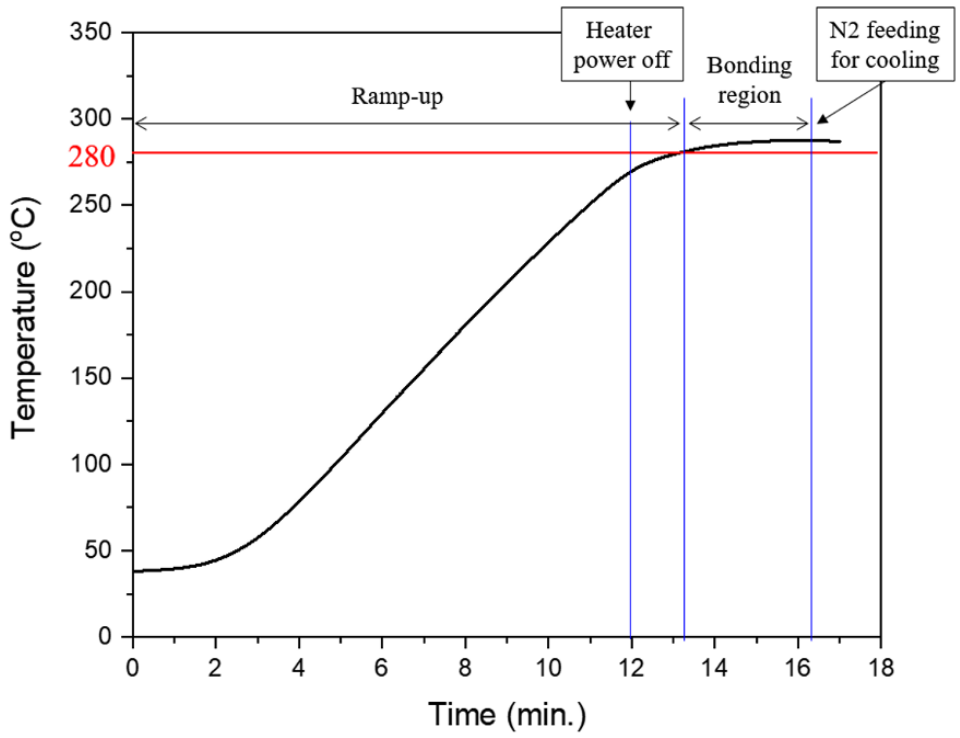

Figure 7.3: Temperature profile of the Sn bonding process obtained from the K-type thermocouple.

Figure 7.4: Photo of bonded Sn coated silicon wafer and 2.5 cm × 3.7 cm slide glass.

7.3 Adhesive Bonding

Organic or inorganic intermediate layers are used for adhesive bonding to form a bond between two surfaces. Adhesive bonding provides hermetic sealing since the adhesive material deforms and flows. The adhesive layer is deposited on one or both of the substrates using spin coating, laminating, inkjet printing or other deposition techniques. Particularly, since the adhesive can be selectively applied to the desired area using an inkjet printer, it can facilitate to combine a complicated MEMS structure. The lateral resolution of the printed line depends on the ink droplet size and the ink spread on a substrate. A high resolution printer is required to apply an adhesive to the tiny pillar surface with a diameter of 175 µm. Typically, a demand-mode print head ejects a smaller droplet (20 µm–100 µm diameter) [70]. After the adhesive is applied, the substrates are brought into close contact, and the intermediate adhesive layer is cured by applying heat and pressure. An enormous number of organic adhesives with different chemistries and material properties are available to use [71].

In the Lorentz DM, the adhesive can be applied to the pillar or mirror surface or both. This adhesive can be used to replace the oxide insulation in Figure 7.1. The heat and pressure required for curing the adhesive can then be provided by the Lorentz actuator.

7.4 Anodic Bonding

Anodic bonding is a method of bonding an alkali-rich glass to any metal. This process is also known as field-assisted thermal bonding. This process was first introduced by Wallis and Pomerantz (1969) and is a cost-effective method for wafer-level packaging [72]. Anodic bonding provides excellent sealing and is widely used in the construction of MEMS devices such as pressure sensors [73], accelerometers [74], and microfluidic devices [75]. Moreover, anodic bonding with glass and various materials such as polysilicon and silicon nitride has been studied extensively to achieve high degrees of

freedom in the device design [76-78]. Aluminum has also been studied as a bonding layer for MEMS devices [79,80].

A glass-aluminum anodic bonding technique can facilitate the bonding process of the Lorentz actuator and the Al/SU-8/Al mirror. The anodic bonding process of the Lorentz DM is proposed in Figure 7.5. In this figure, the oxide insulation layer can be replaced by the sputtered alkali-rich glass for anodic bonding. Two conductive wires have to be placed on the crossbar because the electrical potential for anodic bonding (V_A), the Lorentz force (F_L), and the heat (V_L) should be applied independently.

The type of glasses available are Corning #7740 (Pyrex), soda lime #0080, potash soda lead #0120 and aluminosilicate #1720 [81]. Bonding can be accomplished by placing an Al/SU-8/Al mirror on the actuator substrate. This substrate has sputter deposited glass on its pillar. First, the Lorentz force generated by applying current to the wire causes the actuator to contact and push the Al/SU-8/Al mirror upward, while simultaneously creating the sufficient heat required for the bonding. Next, a DC voltage typically in the range of 100 to 1000 V is applied across the actuator and the mirror stack . At these higher temperatures, the positive ions in the glass become mobile and migrate towards the cathode, creating a space-charge region at the interface. The voltage drop occurs primarily across the small space-charge region causing a very high electrostatic force that further pulls the glass into intimate contact with the mirror surface.

Finally, a covalent bond between the glass and the aluminum surface is formed due to the high temperature. As the positive ions are pulled from the bonding site, it leaves oxygen ions behind. These oxygen ions are then pulled towards the aluminum surface where they form an oxide and become nonconducting, causing a bonding front to expand to the entire pillar surface. This glass-aluminum anodic bonding has been reported to have a bond strength of 12 – 18 MPa depending on the temperature and voltage used, which is much higher than the 4.2 kPa required for the device [82].

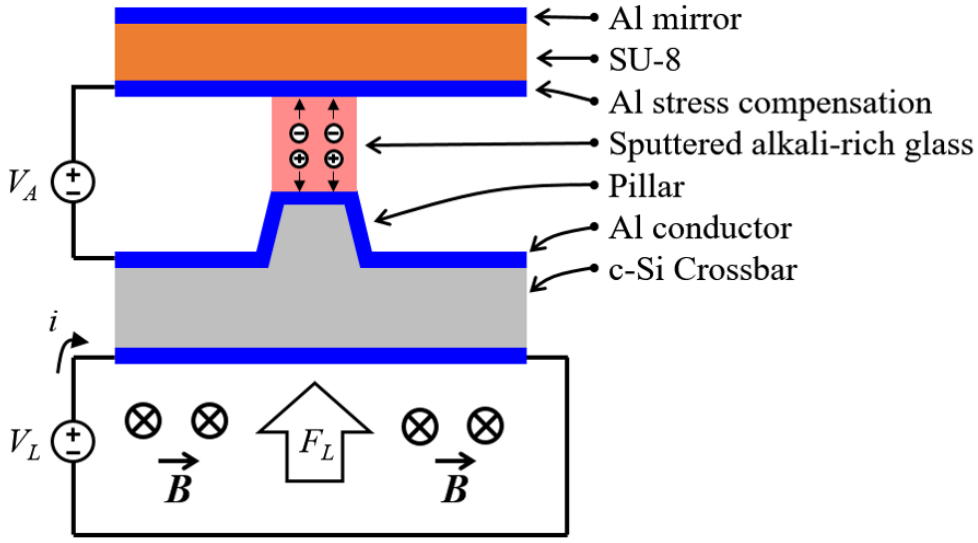

Figure 7.5: Illustration showing the proposed anodic bonding process of the serpentine spring Lorentz actuator and the Al/SU-8/Al mirror. Note that two conductive wires are required on the crossbar to apply an electrical potential for anodic bonding (V_A), a Lorentz force (F_L), and heat generation by applied voltage (V_L) at the same time.

8

Conclusions

Contents

Various MEMS DM devices have been actively researched to enable compensating for image wavefront aberrations in many applications. The MEMS DM has many advantages in terms of cost, space occupancy, and power consumption compared to traditional massive DMs. These MEMS DMs are mainly driven by electrostatic and piezoelectric mechanisms which have small deformations and require a high driving voltage, thus resulting in limited applications. Also, many efforts have been made to mitigate these problems by adopting permanent or electromagnets. Magnetically actuated DMs can be driven at low voltages and currents due to the bi-directional motion of the Lorentz actuators. However, since the device structure is complicated, the fabrication has a high cost and low yield.

This dissertation serves to shed light on the potential benefits of harnessing Lorentz MEMS actuators and polymer-based flexible membranes. The epoxy-based Al/SU-8/Al continuous deformable mirror is successfully demonstrated to provide enough flexibility for a sufficient deformation of ± 5 μm

with low operation voltage and current. In order to deform the Al/SU-8/Al mirror, two different designs of the Lorentz actuator have been proposed and fabricated, which are cantilever arms and serpentine spring Lorentz actuators. However, the cantilever arm design failed to release during the fabrication process. Therefore, the successfully demonstrated serpentine spring Lorentz actuator was tested and bonded to the Al/SU-8/Al mirror. The Al/SU-8/Al mirror substrate was well coupled mechanically to the actuator substrate. This significantly improved the Lorentz DM performance due to its simple geometry and flexible membrane mirror. In this chapter, we will summarize the research contributions and suggest future research directions.

8.1 Summary

The design, modeling, simulation, fabrication, and testing of a micromachined epoxy-based Al/SU-8/Al mirror, a cantilever arms Lorentz actuator, and a serpentine spring Lorentz actuator were discussed. Both Lorentz actuators use the Lorentz force for actuation. The cantilever arms Lorentz actuator, whose fabrication was attempted using electroplating will not be discussed further as it was not successfully fabricated.

The inter-actuator coupling of the Lorentz DM is one of the key elements required for compensating distorted wavefronts in AO technology. However, the inter-actuator coupling is difficult to predict because it changes with the stiffness of the mirror and the actuator simultaneously. The simulation technique proposed in Chapter 3 enables the DM design to be simplified by predicting the inter-actuator coupling, which depends on the stiffness of the mirror and the actuator.

Although previous research has shown that the low stiffness polymer-based membrane is a promising material for DMs, high localized stress and strain have limited its applications due to the non-uniform microstructure of the polymer membrane. As discussed in Chapter 3, the bi-layer technique used in this research allows us to build continuous deformable polymer mirrors with sufficiently flat geometry. Furthermore, the direct topology transfer technique from the very smooth CMP polished silicon surface

onto the mirror enables a mirror roughness of 6.5 nm RMS, which is compatible with a silicon surface roughness of 5.6 nm RMS.

Besides developing technologies to produce a flat and soft mirror, a novel serpentine spring Lorentz actuator array was demonstrated. This actuator array utilizes a large bi-directional vertical motion of the Al/SU-8/Al mirror. A suitable actuator design enables a high yield of such actuators in a massive array structure. As shown in Chapters 4 and 5, the actuator is made of single crystal silicon and is connected to a rigid anchor rail etched from a c-Si wafer. These silicon-based actuators are robust and employ rigid mounting rails that enable easy scalability of the actuator array. Moreover, the demonstrated 5 ×5 Lorentz actuator array has a high-yield monolithic fabrication process. Close agreement between the modeling, simulation and measurement results are observed, and all actuator designs show a linear deflection response as a function of current. A massive displacement of 300 μm at a drive current of ±14.7 mA was demonstrated in the case A actuator (k = 0.1 N/m). This actuator can also be possibly applied to various applications where the surface is manipulated, which include AO, scanning micromirrors, dip pen nanolithography, and more.

The experimental results of the Lorentz DM in Chapter 6 show a large push stroke at very low currents and voltages. The 12 × 12 mm^2 and 4 μm thick Al/SU-8/Al mirror achieved a 17 μm stroke on push mode at an actuation current of 3 mA with < 1V applied to the Lorentz actuator. The response time measured in the dynamic performance section was around 500 μs with a 40 μm stroke at 9 mA current. As a result, the mirror features a comparable large stroke with fast actuation speed. This mechanical response would allow a driving frequency of around 1 kHz. Such miniaturized Lorentz DMs may contribute to significant improvements in adaptive optics technology because of their large stroke and low voltage operation, as well as their potentially high driving frequency of around 1 kHz after actuator bonding.

8.2 Future Work

The final goal of this research is to fabricate DMs with a low operation voltage. The fabrication process for the 5 × 5 serpentine spring Lorentz actuator array and the continuous Al/SU-8/Al mirror has been developed, but the pillar on the actuator and mirror were not yet bonded together. Further research is required to develop the process for bonding the 175 μm diameter pillars and mirrors discussed in Chapter 7. The pillars and the mirror can be bonded together using Sn-fusion bonding, inkjet printed adhesive bonding, or anodic bonding.

In this research, we focused on AO applications to an Earth-based telescope. As mentioned in Chapter 3 and Appendix A, extremely large telescopes such as the TMT require more than 2700 actuators. It is therefore necessary to scale up the design and fabrication process by increasing the number of actuator arrays to a maximum of 64 × 64. In such a massive actuator array structure, a new design and microfabrication process for 8" diameter silicon wafers requires further development. Silicon via technology is necessary for the electrical interconnection between actuators and an external driving circuit. It should also be accompanied by testing on a 13 × 13 cm^2 mirror.

8.3 Concluding Remarks

In conclusion, this dissertation explored methods by which MEMS-based Lorentz actuator arrays made large linear deflections of ± 150 μm at ± 14.7 mA current within a 0.48 Tesla magnetic field possible. This actuator array can be applicable to various 2D surface modification applications due to its large deformation with low current and low temperature of operation. Moreover, the Lorentz DM bonded with a serpentine spring Lorentz actuator provides a large mirror deformation of 17 μm at 3 mA of operation current within a 0.35 Tesla magnetic field. With future research and development, this device shows much promise for enabling low power and inexpensive DMs in a variety of adaptive optics and surface manipulation applications.

Appendices

Appendix A. Deformable mirror specification.

A.1 Strehl Ratio

As is the case for most telescopes, the Strehl ratio (S_R) is used to defined the specification of the AO system. The S_R is defined as the ratio of the peak perturbed image intensity from a point source to the maximum attainable intensity of an ideal optical system limited only by diffraction. The Strehl ratio can be directly replaced by residual phase variance (σ^2_{res}) according to Equation (A.1) in the paper written by P-Y Madec in 2012 [3]:

$$\sigma^2_{res} = \sigma^2_{fitting} + \sigma^2_{temporal} + \sigma^2_{noise} + \sigma^2_{tomo} + \sigma^2_{miscel} \tag{A.1}$$

where $\sigma^2_{fitting}$ is the error due to the finite number of DM actuators, $\sigma^2_{temporal}$ is the error from the finite bandwidth of the DM, σ^2_{noise} is the error from the measurement noise, σ^2_{temo} is the error from the tomographic reconstruction of the turbulent volume above the telescope, and finally σ^2_{miscel} is the error from all the other contributors. Among all the errors, only fitting error and temporal error determine the DM specification. These multiple error budgets can be acquired by the Kolmogorov turbulence model [83], which describes the nature of the wavefront distribution induced by atmospheric turbulence.

A.2 Number of Actuators

The fitting error can be expressed by Equation (A.2) [84]:

$$\sigma^2_{fitting} = k\left(\frac{D}{r_0}\right)^{5/3} N^{-5/6} \tag{A.2}$$

where D is the telescope pupil diameter and r_0 is the Fried parameter, which refers to the size of the air mass with a uniform density and temperature. N is the maximum number of DM actuators, and k is a factor which depends on the shape of the DM influence function, which is usually about 0.274 [34]. The

number of required actuators for the TMT telescope can be calculated using D = 30 m and r_0 = 0.83 m (0.14 at 500 *nm* at Mauna Kea 13N site, and r_0 is proportional to $\lambda^{6/5}$). The calculation result from Equation (A.2) with a fitting error of 0.15 shows about 2,700 useful actuators in the pupil, which corresponds to a 52 × 52 actuator array DM.

A.3 Actuator Mechanical Stroke

The required actuator stroke for the earth-based telescope is defined by the amount of turbulence that needs to be compensated for, and the flatness of the DM reflective surface [2]. Equation (A.3) shows the relationship between the stroke, the pupil diameter, and the Fried parameter. According to Equation (A.3), a smaller size of uniform air mass or a larger pupil diameter requires a larger stroke.

$$d = \frac{3\lambda}{2\pi}\sqrt{l}\left(\frac{D}{r_0}\right)^{5/6} \tag{A.3}$$

The l is 1.03 if the DM compensates for the total amount of aberrations, and l is 0.134 if the DM does not compensate for the tip-tilt. The wavelength λ is 500 nm, which is defined by the measurement wavelength of r_0. The Fried parameter r_0 is 0.1 m for the extremely unstable turbulence case at the TMT site [48,85]. Equation (A.3) shows that the calculated required stroke for the TMT telescope DM is around 10 μm.

A.4 Temporal Response

The temporal error for the DM is given by [2]:

$$\sigma^2_{temporal} = \left(\frac{\tau}{\tau_0}\right)^{5/3} \tag{A.4}$$

where τ is the time lag in the AO loop, and τ_0 represents the atmospheric coherence time and is given by [2]:

$$\tau = 0.314\left(\frac{r_0}{v}\right) \tag{A.5}$$

where v is the mean wind speed weighted by the turbulence profile along the line of sight of the telescope. To determine the DM operation frequency, the worst case for the wind speed and the Fried parameter at the Mauna Kea site [86] is used, which is 15 *m/s* and 0.1 *m* respectively. The atmospheric coherence time (τ_0) is 2 *ms*. Finally, a frequency of 800 *Hz* is chosen to compensate for both atmospheric turbulence and the vibrations of the telescope itself.

Appendix B. Heat loading (ΔT) on serpentine spring Lorentz actuator (Simulation Results).

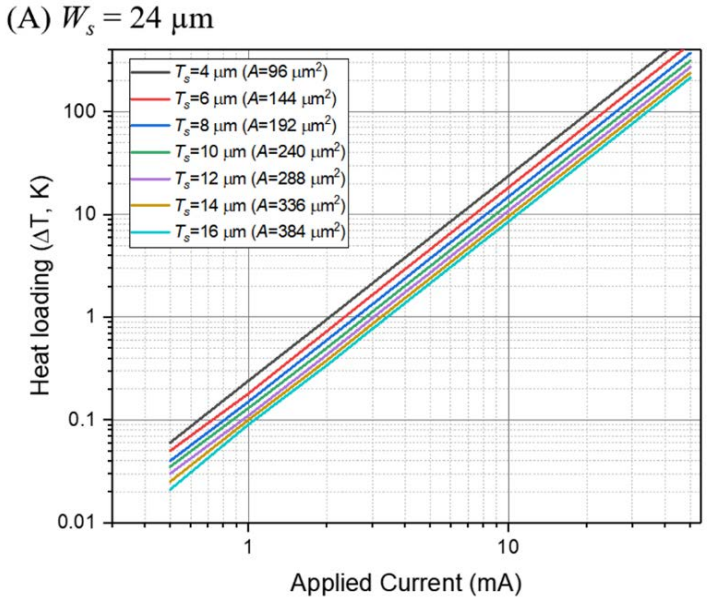

Figure B.1: Heat loading (ΔT) for 24 μm width spring as a function of Joule heating current and thicknesses of the serpentine spring (COMSOL Simulation Result).

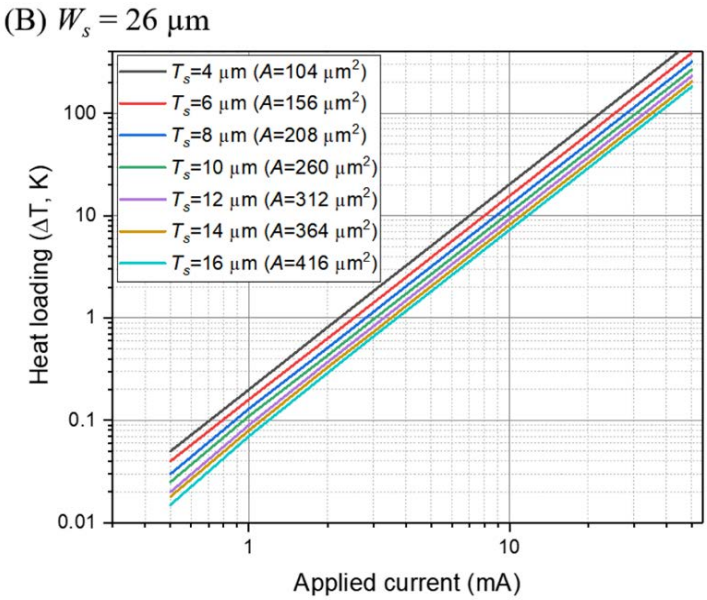

Figure B.2: Heat loading (ΔT) for 26 μm width spring as a function of Joule heating current and thicknesses of the serpentine spring (COMSOL Simulation Result).

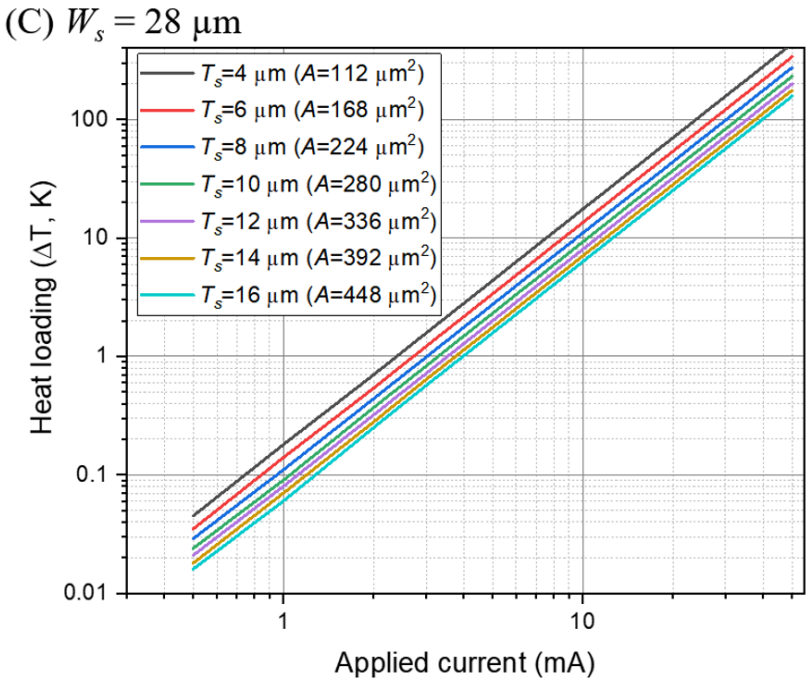

Figure B.3: Heat loading (ΔT) for 28 μm width spring as a function of Joule heating current and thicknesses of the serpentine spring (COMSOL Simulation Result).

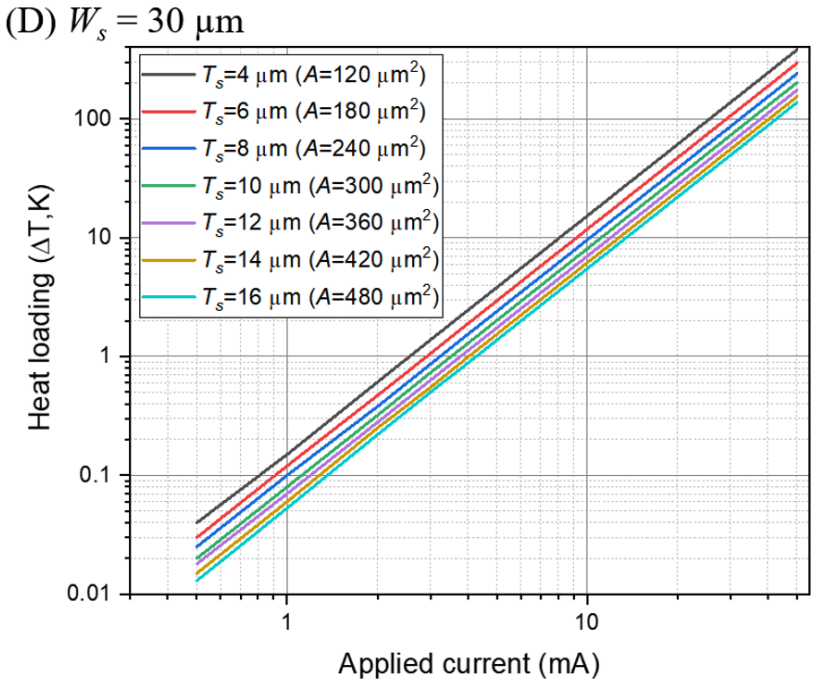

Figure B.4: Heat loading (ΔT) for 30 μm width spring as a function of Joule heating current and thicknesses of the serpentine spring (COMSOL Simulation Result).

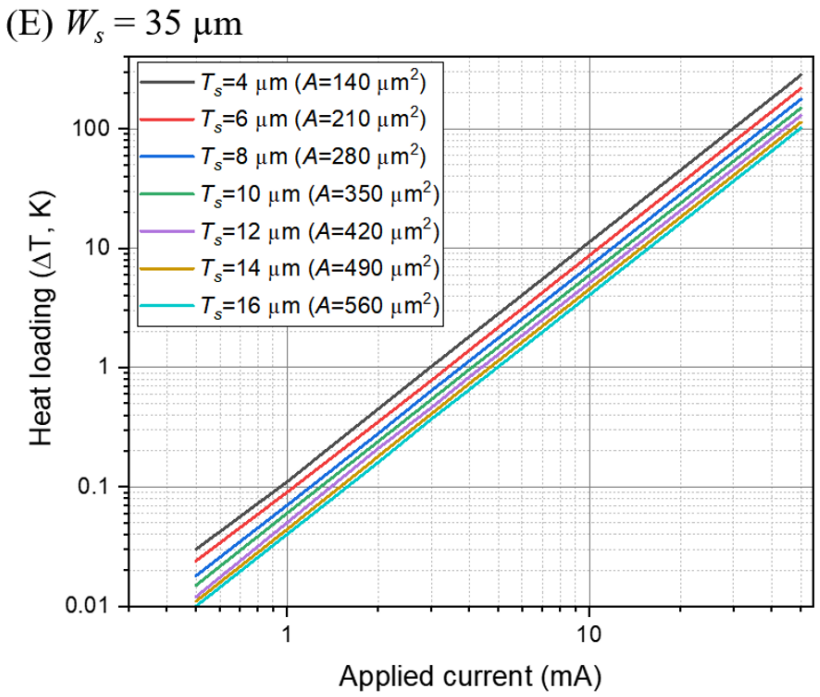

Figure B.5: Heat loading (ΔT) for 35 μm width spring as a function of Joule heating current and thicknesses of the serpentine spring (COMSOL Simulation Result).

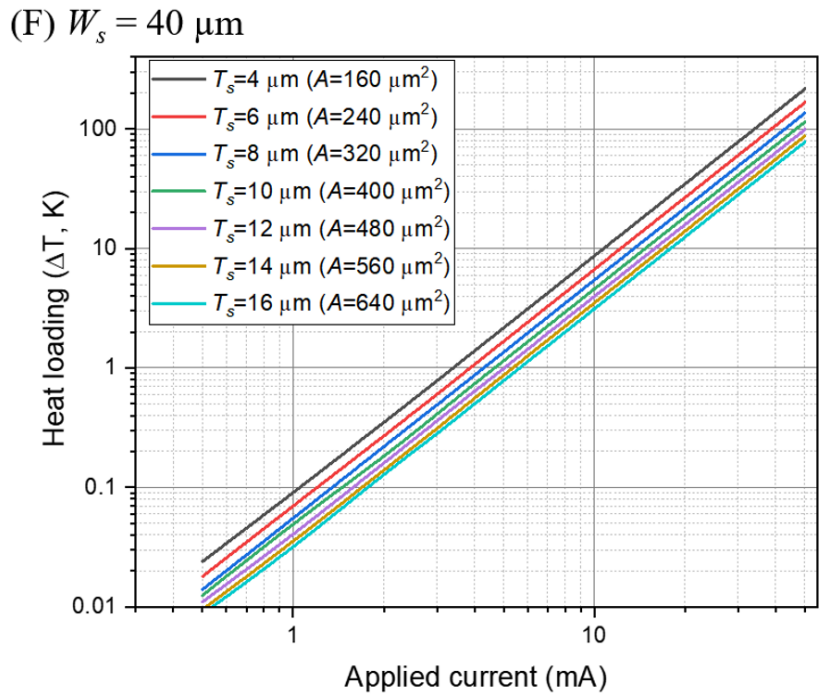

Figure B.6: Heat loading (ΔT) for 40 μm width spring as a function of Joule heating current and thicknesses of the serpentine spring (COMSOL Simulation Result).

Appendix C. Serpentine spring Lorentz actuator comparison table according to the inter-actuator crosstalk.

Table C.1: Comparison between Lorentz DM inter-actuator coupling, spring constant of the actuator, c-Si spring thickness and maximum applicable current for the serpentine spring Lorentz actuator for 24, 26, 28, 30, 35, and 40 μm width serpentine spring.

Spring width	Items	Values				
	The Lorentz DM inter-actuator coupling (%)	30.0	25.0	20.0	15.0	10.0
24 μm	(A) Required force for 5 μm deformation of Al/SU-8/Al mirror (μN)	5.4	6.05	6.75	7.5	8.2
	(B) Required spring constant of actuator (N/m. from COMSOL)	0.8	1.1	1.65	2.8	4.9
	c-Si spring thickness of the serpentine spring actuator	6.4	7.4	8.7	10.6	13.1
	Cross-sectional area of *c-Si* spring (um^2)	153.6	177.6	208.8	254.4	314.4
	(C) Max. allowable current (mA) for $\Delta T \leq 50$ K (From COMSOL)	13.5	15	17.5	20.7	25.1
	*** Required force for 5 μm deformation of the Lorentz DM (μN)**	9.4	11.55	15	21.5	32.7
	* Required current for 5 μm deformation of the Lorentz DM (mA) with 0.4 Tesla magnet	11.3	13.9	18.0	25.8	39.3
	Current margin (%)	16.3	7.5	**-3.0**	**-24.8**	**-56.6**
	* Required current for 5 μm deformation of the Lorentz DM (mA) with 0.7 Tesla magnet	6.5	7.9	10.3	14.8	22.5
	Current margin (%)	52.2	47.1	41.1	28.7	10.5
26 μm	*c-Si* spring thickness of the serpentine spring actuator	6.8	7.8	9.2	11.2	13.8
	Cross-sectional area of *c-Si* spring (um^2)	163.2	187.2	220.8	268.8	331.2
	(C) Max. allowable current (mA) for $\Delta T \leq 50$ K (From COMSOL)	14	15.7	18.5	21.5	26.4
	*** Required force for 5 μm deformation of the Lorentz DM (μN)**	9.4	11.55	15	21.5	32.7
	* Required current for 5 μm deformation of the Lorentz DM (mA) with 0.4 Tesla magnet	11.3	13.9	18.0	25.8	39.3
	Current margin (%)	19.3	11.6	2.5	**-20.2**	**-48.9**
	* Required current for 5 μm deformation of the Lorentz DM (mA) with 0.7 Tesla magnet	6.5	7.9	10.3	14.8	22.5
	Current margin (%)	53.9	49.5	44.3	31.3	14.9
28 μm	*c-Si* spring thickness of the serpentine spring actuator	7.2	8.3	9.7	11.9	14.6
	Cross-sectional area of *c-Si* spring (um^2)	172.8	199.2	232.8	285.6	350.4
	(C) Max. allowable current (mA) for $\Delta T \leq 50$ K (From COMSOL)	14.5	17	19.3	22.8	27.7
	*** Required force for 5 μm deformation of the Lorentz DM (μN)**	9.4	11.55	15	21.5	32.7

	* Required current for 5 µm deformation of the Lorentz DM (mA) with 0.4 Tesla magnet	11.3	13.9	18.0	25.8	39.3
	Current margin (%)	22.1	18.3	6.6	-13.3	-41.9
	* Required current for 5 µm deformation of the Lorentz DM (mA) with 0.7 Tesla magnet	4.5	5.6	7.2	10.3	15.7
	Current margin (%)	68.8	67.3	62.6	54.7	43.2
30 µm	*c-Si* spring thickness of the serpentine spring actuator	7.4	8.5	10	12.2	15
	Cross-sectional area of *c-Si* spring (um^2)	177.6	204	240	292.8	360
	(C) Max. allowable current (mA) for $\Delta T \leq 50$ K (From COMSOL)	15	17.4	19.6	23.5	28.4
	*** Required force for 5 µm deformation of the Lorentz DM (µN)**	9.4	11.55	15	21.5	32.7
	* Required current for 5 µm deformation of the Lorentz DM (mA) with 0.4 Tesla magnet	11.3	13.9	18.0	25.8	39.3
	Current margin (%)	24.7	20.2	8.0	**-10.0**	**-38.4**
	* Required current for 5 µm deformation of the Lorentz DM (mA) with 0.7 Tesla magnet	6.5	7.9	10.3	14.8	22.5
	Current margin (%)	57.0	54.4	47.4	37.2	20.9
35 µm	*c-Si* spring thickness of the serpentine spring actuator	7.7	8.8	10.3	12.6	15.6
	Cross-sectional area of *c-Si* spring (um^2)	184.8	211.2	247.2	302.4	374.4
	(C) Max. allowable current (mA) for $\Delta T \leq 50$ K (From COMSOL)	15.5	17.5	20	24.2	29
	*** Required force for 5 µm deformation of the Lorentz DM (µN)**	9.4	11.55	15	21.5	32.7
	* Required current for 5 µm deformation of the Lorentz DM (mA) with 0.4 Tesla magnet	11.3	13.9	18.0	25.8	39.3
	Current margin (%)	27.1	20.7	9.9	**-6.8**	**-35.5**
	* Required current for 5 µm deformation of the Lorentz DM (mA) with 0.7 Tesla magnet	6.5	7.9	10.3	14.8	22.5
	Current margin (%)	58.3	54.7	48.5	39.0	22.6
40 µm	*c-Si* spring thickness of the serpentine spring actuator	7.9	9.1	10.6	13	16.1
	Cross-sectional area of *c-Si* spring (um^2)	189.6	218.4	254.4	312	386.4
	(C) Max. allowable current (mA) for $\Delta T \leq 50$ K (From COMSOL)	16	18	20.7	25	29.6
	*** Required force for 5 µm deformation of the Lorentz DM (µN)**	9.4	11.55	15	21.5	32.7
	* Required current for 5 µm deformation of the Lorentz DM (mA) with 0.4 Tesla magnet	11.3	13.9	18.0	25.8	39.3
	Current margin (%)	29.4	22.9	12.9	**-3.4**	**-32.8**
	* Required current for 5 µm deformation of the Lorentz DM (mA) with 0.7 Tesla magnet	6.5	7.9	10.3	14.8	22.5
	Current margin (%)	59.6	55.9	50.2	40.9	24.1

* Required force for 5µm deformation of the Lorentz DM = (A) + ((B) × 5 × 10^{-6}m)

** Required current for Lorntz force generated on the crossbar (2080 µm length) within 0.4 and 0.7 Tesla magnetic field.

Appendix D. Mask Pattern Transfer Process.

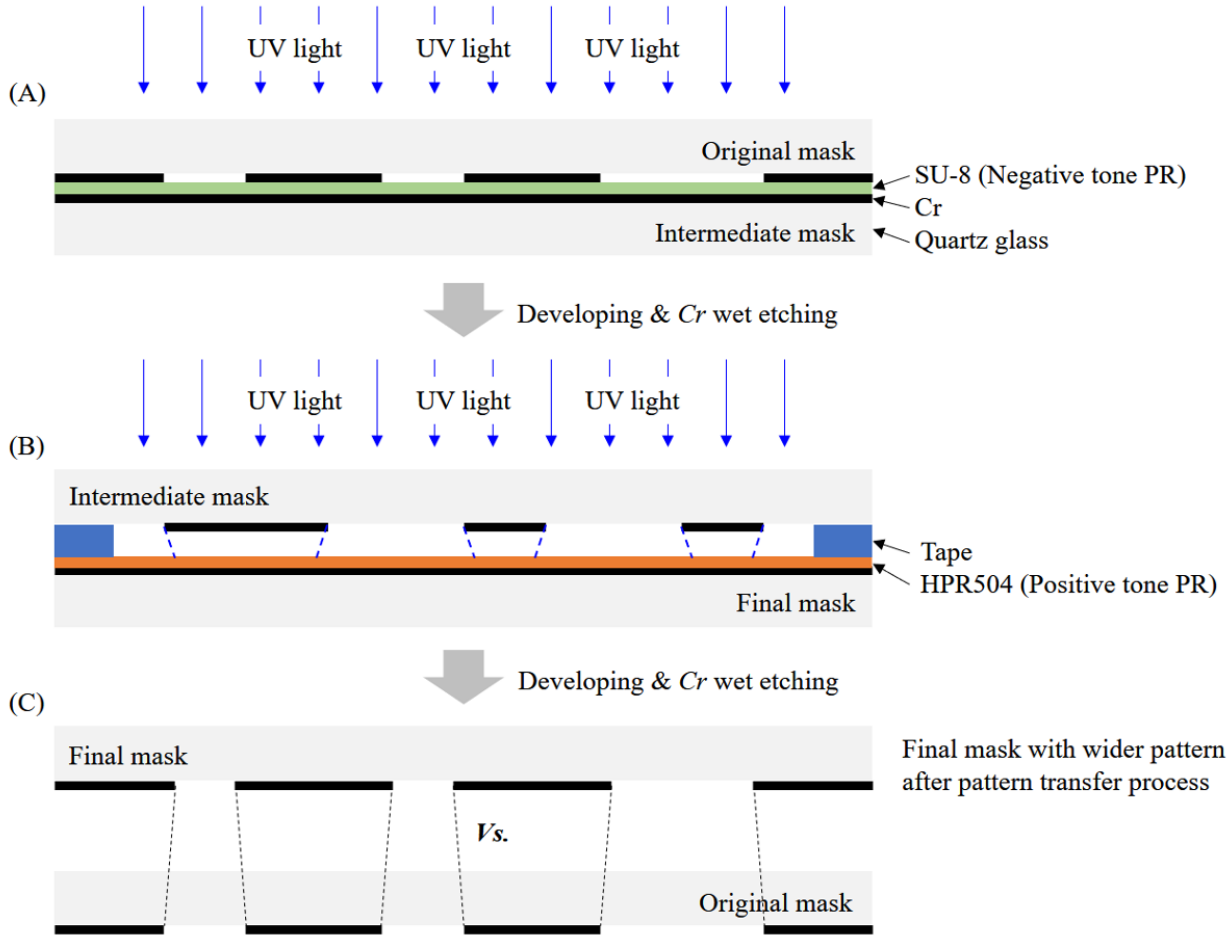

Figure D.1: Illustration of the pattern transfer process. (A) Inversed pattern transferred on intermediate mask using SU-8 negative tone photoresist, (B) A wider pattern is transferred on HPR 504 positive tone photoresist using UV refraction and/or diffraction due to the gap between the two masks, and (C) The result of comparison between a original mask and the wider pattern mask transferred from original mask.

Appendix E. UV Laser Mask Fabrication Provess.

Instrument: Oxford Laser Microachining System

[Process Parameters]

- Laser power: 30 mW
- Pulse frequency: 400 Hz
- Laser spot size after focusing on the sample: 30 μm

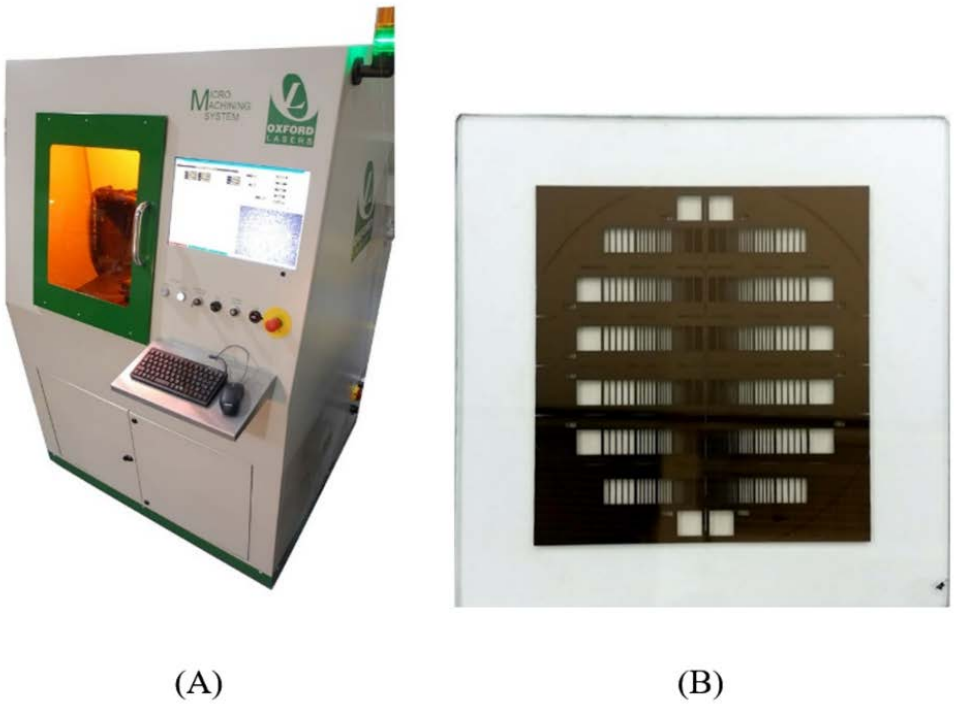

(A) (B)

Figure F.1: The measurement result of the magnetic field at xx mm above the magnet.

Appendix F. Magnetic Field Measurement Results at Various Heights.

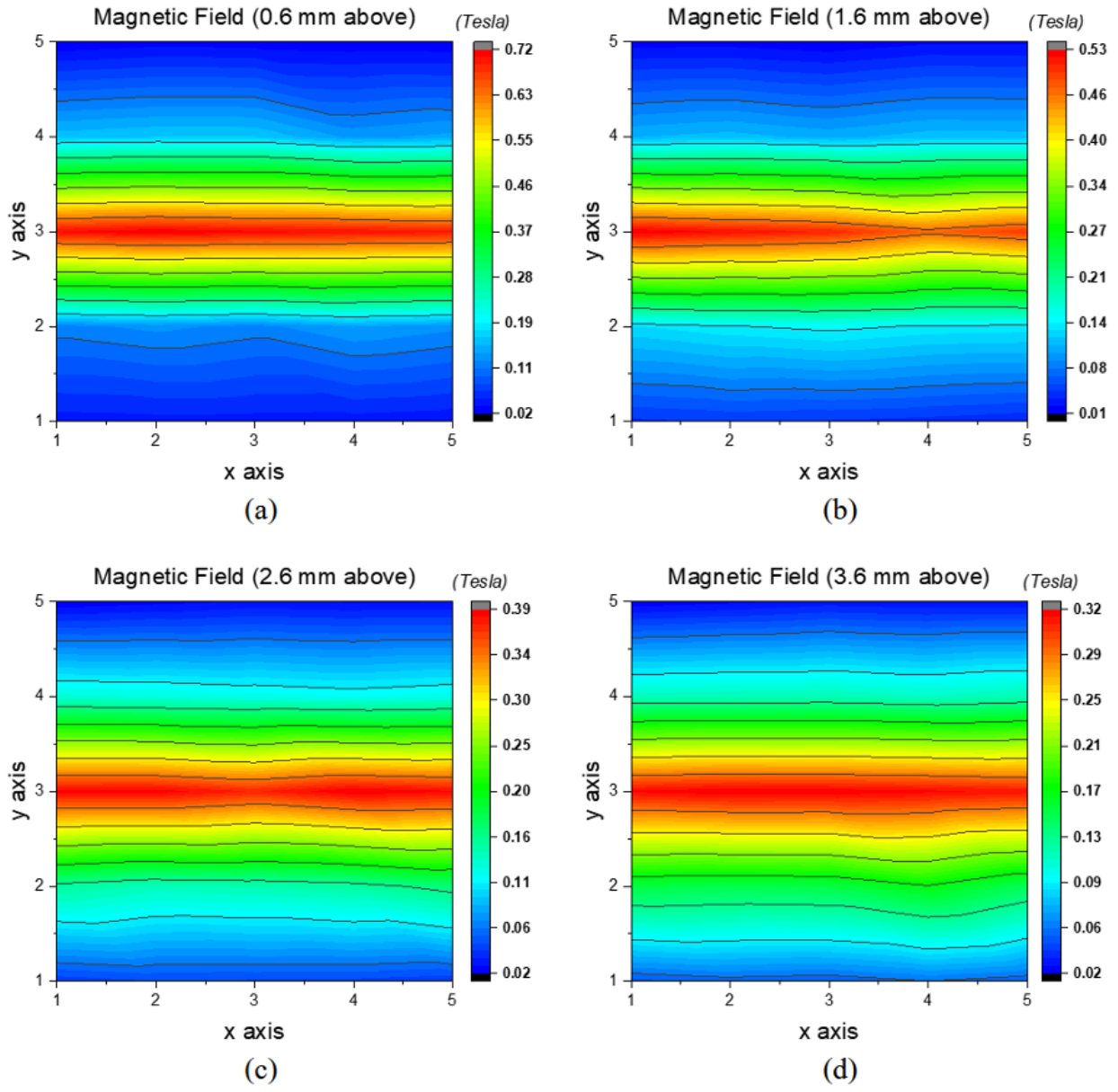

Figure F.1: The measurement results of the magnetic field at (a) 0.6 mm, (b) 1.6 mm, (c) 2.6 mm, and (d) 3.6 mm above the ND-50 permanent magnet.

Bibliography

[1] Babcock, H. W., The possibility of compensating astronomical seeing. *Publications of the Astronomical Society of the Pacific*, pp. 229–236, 1953.

[2] Robert K. Tyson. Principles of Adaptive Optics, Third Edition. CRC Press. 2011. ISBN-13: 978-1439808580

[3] Madec, P.-Y., Overview of deformable mirror technologies for adaptive optics and astronomy. In *SPIE Astronomical Telescopes+ Instrumentation*, International Society for Optics and Photonics, pp. 844705–844705, 2012. Retrieved from http://proceedings.spiedigitallibrary.org/proceeding.aspx?articleid=1358867

[4] Wallace, B. P., Hampton, P. J., Bradley, C. H., & Conan, R., Evaluation of a MEMS deformable mirror for an adaptive optics test bench. *Optics Express*, 14(22), pp. 10132–10138, 2006.

[5] Perreault, J. A., Bifano, T. G., Levine, B. M., & Horenstein, M. N., Adaptive optic correction using microelectromechanical deformable mirrors. *Optical Engineering*, 41(3), 561–566, 2002.

[6] Ealey, M. A., Continuous facesheet low voltage deformable mirrors, *Optical Engineering*, vol. 29, no. 10, p. 1191, 1990.

[7] R. Dekany *et al.*, PALM-3000: Exoplanet Adaptive Optics for the 5-meter Hale Telescope, *The Astrophysical Journal*, vol. 776, no. 2, p. 130, Oct. 2013.

[8] A. H. Bouchez *et al.*, Status of the PALM-3000 high-order adaptive optics system. *Proc. Of SPIE*, vol. 7439, p. 74390H, 2009.

[9] Bifano, T., Shaping light: MOEMS deformable mirrors for microscopes and telescopes. *Proc. Of SPIE*, vol. 7595, pp. 759502-1, 2010. https://doi.org/10.1117/12.848221

[10] Dickensheets, D. L., Requirements of MEMS membrane mirrors for focus adjustment and aberration correction in endoscopic confocal and optical coherence tomography imaging instruments. Journal of Micro/Nanolithography, *MEMS and MOEMS*, 7(2), pp. 021008, 2008. https://doi.org/10.1117/1.2911024

[11] Burns, D. M., & Bright, V. M., Micro-electro-mechanical focusing mirrors. In *Micro Electro Mechanical Systems, 1998. MEMS 98*, IEEE, pp. 460–465, 1998. Retrieved from http://ieeexplore.ieee.org/abstract/document/659801/

[12] Vera-Díaz, F. A., & Doble, N., The Human Eye and Adaptive Optics. *INTECH Open Access Publisher*. 2012. Retrieved from http://cdn.intechopen.com/pdfs-wm/26714.pdf

[13] Daly, E., Dalimier, E., & Dainty, C., Requirements for MEMS mirrors for adaptive optics in the eye. *In MOEMS-MEMS 2006 Micro and Nanofabrication*, International Society for Optics and Photonics, pp. 611309–611309, 2006. Retrieved from http://proceedings.spiedigitallibrary.org/proceeding.aspx?articleid=1274856

[14] Zhang, Y., & Roorda, A., MEMS Deformable Mirror for Ophthalmic Imaging. *In Proc. of SPIE* vol. 6113, pp. 61130A–1–8, 2006.

[15] Liang, J., Williams, D. R., & Miller, D. T., Supernormal vision and high-resolution retinal imaging through adaptive optics. *Journal of the Optical Society of America A*, 14(11), 2884–2892. 1997.

[16] Wilson, K. E., Wright, M. W., Lee, S., & Troy, M., Adaptive optics for daytime deep space laser communications to Mars. *Presented at the Digest of the LEOS Summer Topical Meetings*, Citeseer, 2005. Retrieved from http://citeseerx.ist.psu.edu/viewdoc/download?doi=10.1.1.586.351&rep=rep1&type=pdf

[17] Fugate, R. Q., Laser beacon adaptive optics for power beaming applications. *Presented at the SPIE*, Los Angeles, CA, vol. 2121, pp. 68–76, 1994. https://doi.org/10.1117/12.174170

[18] Gemini Captures Close Encounter of Jupiter's Red Spots. (2006, July 20). Retrieved February 20, 2018, from https://www.gemini.edu/node/196

[19] Biasi, R., Gallieni, D., Salinari, P., Riccardi, A., & Mantegazza, P., Contactless thin adaptive mirror technology: past, present, and future. *Proceedings of SPIE In Adaptive Optics Systems II*, International Society for Optics and Photonics, vol. 7736, p. 77362B, 2010. doi: 10.1117/12.858816

[20] Bell, D. J., Lu, T. J., Fleck, N. A., & Spearing, S. M., MEMS actuators and sensors: observations on their performance and selection for purpose. *Journal of Micromechanics and Microengineering*, 15(7), pp. S153–S164, 2005. https://doi.org/10.1088/0960-1317/15/7/022

[21] Hsu, T.-R., MEMS & Microsystems: Design, Manufacture, and Nanoscale Engineering. *John Wiley & Sons*, 2008.

[22] Lv, X., Wei, W., Mao, X., Chen, Y., Yang, J., & Yang, F., A novel MEMS electromagnetic actuator with large displacement. *Sensors and Actuators A: Physical*, 221, 22–28, 2015. https://doi.org/10.1016/j.sna.2014.10.028

[23] Yellin, M., Using Membrane Mirrors In Adaptive Optics, *Proceedings of SPIE*, vol. 0075, pp. 97–102, 1976. https://doi.org/10.1117/12.954743

[24] Cornelissen, S. A., 4096-element continuous face-sheet MEMS deformable mirror for high-contrast imaging. Journal of Micro/Nanolithography, MEMS, and MOEMS, 8(3), pp. 031308, 2009. https://doi.org/10.1117/1.3158067

[25] Zhang, W.-M., Yan, H., Peng, Z.-K., & Meng, G., Electrostatic pull-in instability in MEMS/NEMS: A review. *Sensors and Actuators A: Physical*, vol. 214, pp. 187–218. 2014. https://doi.org/10.1016/j.sna.2014.04.025

[26] Fernandez, B. R., Bouchti, M. A., & Kubby, J., High-stroke, high-order MEMS deformable mirrors. *Journal of Micro/Nanolithography*, MEMS, and MOEMS, 12(3), 2013.

[27] Friese, C., & Zappe, H., Deformable Polymer Adaptive Optical Mirrors. *Journal of Microelectromechanical Systems*, 17(1), pp. 11–19. 2008. https://doi.org/10.1109/JMEMS.2007.913075

[28] Lin, P.-Y., Hsieh, H.-T., & Su, G.-D. J., Design and fabrication of a large-stroke MEMS deformable mirror for wavefront control. *Journal of Optics*, vol. 13(5), pp. 055404, 2011. https://doi.org/10.1088/2040-8978/13/5/055404

[29] Helmbrecht, M. A., He, M., Kempf, C., & Rhodes, P., Scaling up of the Iris AO segmented DM technology for atmospheric correction. *In Proceedings of of the Advanced Maui Optical and Space Surveillance Technologies Conference,* pp. E72, 2009.

[30] Ma, J., Liu, Y., Chen, C., Li, B., & Chu, J., Deformable mirrors based on piezoelectric unimorph microactuator array for adaptive optics correction. *Optics Communications*, vol. 284(21), pp. 5062–5066, 2011. https://doi.org/10.1016/j.optcom.2011.07.021

[31] Divoux, C., Cugat, O., Reyne, G., Boussey-Said, J., & Basrour, S., Deformable mirror using magnetic membranes: application to adaptive optics in astrophysics. *IEEE Transactions on Magnetics*, vol. 34(5), pp. 3564–3567, 1998.

[32] Cugat, O., Basrour, S., Divoux, C., Mounaix, C., & Reyne, G., Deformable magnetic mirror for adaptive optics-Technical aspects. *Sensors and Actuators A: Physical*, (89), pp. 1–9, 2001.

[33] Roopashree, M. B., Vyas, A., Prasad, B. R., Predeep, P., Thakur, M., & Varma, M. K. R., Influence Function Measurement of Continuous Membrane Deformable Mirror Actuators Using Shack Hartmann Sensor, *AIP Conf. Proc*. vol. 1391, pp. 453–455, 2011. https://doi.org/10.1063/1.3643577

[34] Tyson, R., Adaptive Optics Engineering Handbook. *CRC Press*, 1999.

[35] Kovacs, G. T. A., Micromachined Transducers Sourcebook. *WCB/McGraw-Hill*, 1998.

[36] Petersen, K. E., Silicon as a mechanical material.pdf. *In Proceedings of the IEEE,* pp. 420–457, 1982. https://doi.org/10.1109/PROC.1982.12331

[37] Rashidian, B., & Allen, M. G., Electrothermal microactuators based on dielectric loss heating. In Micro Electro Mechanical Systems, *MEMS'93, Proceedings An Investigation of Micro Structures, Sensors, Actuators, Machines and Systems*. IEEE, pp. 24–29, 1993.

[38] Bolz, R. E., CRC Handbook of Tables for Applied Engineering Science. (Second Edition) *CRC Press*, Cleveland, Ohio, 1973.

[39] Sharpe, W. N., Yuan, B., Vaidyanathan, R., & Edwards, R. L., Measurements of Young's modulus, Poisson's ratio, and tensile strength of polysilicon. *In Micro Electro Mechanical Systems, MEMS'97, Proceedings, IEEE.*, pp. 424–429, 1997.

[40] Shackelford, J. F., & Alexander, W., CRC Materials Science and Engineering Handbook (Third Edition) *CRC Press*, 2000.

[41] SU-87 2000 Specification, *MICROCHEM*,2007. Retrieved from http://christophe.yamahata.fr/projects/pdf/51.pdf

[42] Keller, S., Blagoi, G., Lillemose, M., Haefliger, D., & Boisen, A., Processing of thin SU-8 films. *Journal of Micromechanics and Microengineering*, vol. 18(12), pp. 125020, 2008. https://doi.org/10.1088/0960-1317/18/12/125020

[43] Shaw, J. M., Gelorme, J. D., LaBianca N. C., Conley W. E, Holmes S. J., Negative photoresists for optical lithography. *IBM Journal of Research and Development, (1.2)*, pp. 81–94, 1997. https://doi.org/10.1147/rd.411.0081

[44] Hartley, A., Miles, R., Dimitrakopoulos, N., & Pollard, R. D., SU-8 beams and membranes. *In 1st EMRS DTC Technical conference*, Edinburgh, 2004.

[45] Telescopes and Instrumentation. Retrieved January 10, 2018, from http://www.eso.org/public/teles-instr/

[46] The GMT Science Case flows from the Decadal Survey's report "Astronomy and Astrophysics in the New Millennium." Retrieved January 10, 2018, from https://www.gmto.org/

[47] TMT Science Brochure. Retrieved January 10, 2018, from https://www.tmt.org/system/media_files/binaries/60/original/tmt_Scientific_Brochure.pdf?1500939532

[48] Herriot, G., Hickson, P., Ellerbroek, B. L., Andersen, D. A., Davidge, T., Erickson, D. A., Véran, J.-P., NFIRAOS: TMT narrow field near-infrared facility adaptive optics, *Presented at the Advances in Adaptive Optics II, International Society for Optics and Photonics*, vol. 6272, pp. 62720Q, 2006. https://doi.org/10.1117/12.672337

[49] Hass, G., & Waylonis, J. E., Optical constants and reflectance and transmittance of evaporated aluminum in the visible and ultraviolet. *Journal of the Optical Society of America*, vol. 51(7), pp. 719–722, 1961. Retrived from https://www-osapublishing-org.uml.idm.oclc.org/josa/home.cfm

[50] Bennett, J. M., & Ashley, E. J., Infrared Reflectance and Emittance of Silver and Gold Evaporated in Ultrahigh Vacuum. *Applied Optics*, 4(2), pp. 221–224, 1965. https://doi.org/10.1364/AO.4.000221

[51] COMSOL Multiphysics® Modeling Software., (Version 5.2). *COMSOL, Inc*. 100 District Avenue Burlington, MA 01803 USA: COMSOL Inc., 2017. Retrieved from https://www.comsol.com/

[52] Ishiyama, C., Sone, M., & Higo, Y., Effects of heat curing on adhesive strength between microsized SU-8 and Si substrate. *Proceedings of SPIE - The International Society for Optical Engineering*, art. no. 65331F. 6533, 2007. https://doi.org/10.1117/12.736535

[53] Timoshenko, S., & Woinowsky-Krieger, S., Theory of Plates and Shells (2nd ed.). Mineola, New York: *Dover publications, Inc.*, 1936.

[54] Ulaby, F. T., Electromagnetics for Engineers (1 edition). *Upper Saddle River*, NJ: Pearson, 2004.

[55] Ko, J. S., Lee, M. L., Lee, D.-S., Choi, C. A., & Tae Kim, Y., Development and application of a laterally driven electromagnetic microactuator. *Applied Physics Letters*, 81(3), pp. 547–549, 2002. https://doi.org/10.1063/1.1494462

[56] Halg, B., On a nonvolatile memory cell based on micro-electro-mechanics. In Micro electro mechanical systems, proceedings, an investigation of micro structures, sensors, actuators, machines and robots. IEEE, pp. 172–176, 1990.

[57] Park, B., Residual Stress Control of Sputter Deposited Cu, Cr, and Cu/Cr/Cu multilayered film, *NSFL internal research report*, University of Manitoba, pp. 1–12, 2017.

[58] Hanabusa, T., Kusaka, K., & Sakata, O., Residual stress and thermal stress observation in thin copper films. *Thin Solid Films*, vol. 459(1–2), pp. 245–248, 2004. https://doi.org/10.1016/j.tsf.2003.12.102

[59] Grachev, S. Y., Tichelaar, F. D., & Janssen, G. C. A. M., Stress in sputter-deposited Cr films: Influence of Ar pressure. *Journal of Applied Physics*, vol. 97(7), pp. 073508, 2005. https://doi.org/10.1063/1.1876579

[60] Janssen, G. C. A. M., Abdalla, M. M., van Keulen, F., Pujada, B. R., & van Venrooy, B., Celebrating the 100th anniversary of the Stoney equation for film stress: Developments from polycrystalline steel strips to single crystal silicon wafers. *Thin Solid Films*, vol. 517(6), pp. 1858–1867, 2009. https://doi.org/10.1016/j.tsf.2008.07.014

[61] Park, B., & Afsharipour, E., Development of Reverse-pulse Current Electrodeposition of Copper film with SPR 220-7 thick mold, *NSFL internal research report*, University of Manitoba, pp. 1–15. 2017.

[62] Ledbetter, H. M., & Naimon, E. R., Elastic Properties of Metals and Alloys Copper, *Journal of Physical and Chemical Reference Data*, 3(4), pp. 897–935. 1974.

[63] Cho, C.-H., Characterization of Young's modulus of silicon versus temperature using a "beam deflection" method with a four-point bending fixture. *Current Applied Physics*, 9(2), 538–545, 2009. https://doi.org/10.1016/j.cap.2008.03.024

[64] Milman, Y. V., Gridneva, I. V., & Golubenko, A. A., Construction of stess-strain curves for brittle materials by indentation in a wide temperature range. *Science of Sintering*, vol. 39(1), pp. 67–75, 2007. https://doi.org/10.2298/SOS0701067M

[65] Elwenspoek, M., & Jansen, H., Silicon Micromachining. The Edinburgh Building, Cambridge CB2 2RU, UK: *Cambridge University Press*, 1998. Retrieved from https://www.chapters.indigo.ca/en-ca/books/silicon-micromachining-silicon-micromachining/9780521607674-item.html

[66] Campbell, S., The Science and Engineering of Microelectronic Fabrication. (2nd ed.), New York: *Oxford University Press*, 2001. Retrieved from https://www.amazon.ca/Science-Engineering-Microelectronic-Fabrication/dp/0195136055

[67] Cornelissen, S. A., Bierden, P. A., Bifano, T. G., & Stewart, J. B., MEMS Deformable Mirrors for Adaptive Optics in Astronomical Imaging. Presented at *the SPIE 7736*, Adaptive Optics Systems II,

California, USA, 2010. Retrieved from http://www.amostech.com/TechnicalPapers/2006/Adaptive_Optics/Cornelissen.pdf

[68] Yun, C. H., Martin, J. R., Tarvin, E. B., & Winbigler, J. T., AL to AL wafer bonding for MEMS encapsulation and 3-D interconnect. In *Micro Electro Mechanical Systems, MEMS 2008*. IEEE, pp. 810–813, 2008.

[69] Zhu, Z., Yu, M., Zhu, Y., Wang, P., Liu, C., Wang, W., … Jin, Y., Low temperature Al based wafer bonding using Sn as intermediate layer. In *13th International Conference on Electronic Packaging Technology High Density Packaging*, pp. 127–130, 2012. https://doi.org/10.1109/ICEPT-HDP.2012.6474584

[70] Lau, G.-K., & Shrestha, M., Ink-Jet Printing of Micro-Electro-Mechanical Systems (MEMS). Micromachines, 8(7), pp. 194, 2017. https://doi.org/10.3390/mi8060194

[71] Alvino, W. M., Plastics for electronics: Materials, properties and design applications. *McGraw-Hill*, New York, 1995. Retrieved from http://onlinelibrary-wiley-com.uml.idm.oclc.org/doi/10.1002/aic.690420835/full

[72] Wallis, G., & Pomerantz, D. I., Field Assisted Glass-Metal Sealing. *Journal of Applied Physics*, 40(10), pp. 3946–3949, 1969. https://doi.org/10.1063/1.1657121

[73] Hanneborg, A., & Ohlckers, P., A., Capacitive silicon pressure sensor with low TC0 and high long term stability. *Sensors and Actuators* A, 21–23, pp. 151–154, 1990.

[74] Lapadatu, D., Habibi, S., Reppen, B., Salomonsen, G., & Kvisteroy, T., Dual-axes capacitive inclinometer/low-g accelerometer for automotive applications. In *Micro Electro Mechanical Systems (MEMS 2001)*, pp. 34–37, 2001.

[75] Acero, M. C., Plaza, J. A., Esteve, J., Carmona, M., Marco, S., & Samitier, J., Design of a modular micropump based on anodic bonding. *Journal of Micromechanics and Microengineering*, 7(3), 179, 1997.

[76] Arx, J. V., Ziaie, B., Dokmeci, M., & Najafi, K., Hermeticity testing of glass-silicon packages with on chip feed throughs. In *Solid-State Sensors and Actuators, 1995 and Eurosensors IX.. Transducers' 95*, vol. 1, pp. 244–247, 1995

[77] Plaza, J. A., Esteve, J., & Lora-Tamayo, E., Effect of silicon oxide, silicon nitride and polysilicon layers on the electrostatic pressure during anodic bonding. *Sensors and Actuators A*, 67, pp. 181–184, 1998.

[78] Weichel, S., de Reus, R., Bouaidat, S., Rasmussen, P. A., Hansen, O., Birkelund, K., & Dirac, H., Low-temperature anodic bonding to silicon nitride. *Sensors and Actuators A*, 82, pp. 249–253, 2000.

[79] Nese, M., & Hanneborg, A., Anodic bonding of silicon to silicon wafers coated with aluminium, silicon oxide, polysilicon or silicon nitride. *Sensors and Actuators A*, 37–38, pp. 61–67, 1993.

[80] Veenstra, T. T., Berenschot, J. W., Gardeniers, J. G. E., Sanders, R. G. P., Elwenspoek, M. C., & Berg, A. van den., Use of Selective Anodic Bonding to Create Micropump Chambers with Virtually No Dead Volume. *Journal of The Electrochemical Society*, 148(2), pp. G68–G72, 2001. https://doi.org/10.1149/1.1339873

[81] Madou, M. J., Fundamentals of Microfabrication: The Science of Miniaturization, Second Edition (2 edition). Boca Raton: CRC Press, 2002.

[82] Schjølberg-Henriksen, K., Poppe, E., Moe, S., Storås, P., Taklo, M. M. V., Wang, D. T., & Jakobsen, H., Anodic bonding of glass to aluminium. *Microsystem Technologies*, 12(5), pp. 441–449, 2006. https://doi.org/10.1007/s00542-005-0040-8

[83] Kolmogorov, A. N., The local structure of turbulence in incompressible viscous fluid for very large Reynolds numbers. *In Dokl. Akad. Nauk SSSR*, vol. 30, pp. 299–303, 1941.

[84] Noll, R. J., Zernike polynomials and atmospheric turbulence. *SPIE MILESTONE SERIES MS*, vol. 92, pp. 145–145, 1994.

[85] Flicker, R., Mauna Kea turbulence statistics from the TMT MASS/DIMM and we ather station at the 13 North site. (No. KAON 415). *W.M. Keck Observatory*, 2006. Retrieved from http://www.oir.caltech.edu/twiki_oir/pub/Keck/NGAO/NewKAONs/KAON415.pdf

[86] MacMynowski, D. G., Blaurock, C., & Angeli, G. Z., Dynamic analysis of TMT, Presented at the Modeling, *Systems Engineering, and Project Management for Astronomy III, International Society for Optics and Photonics*, vol. 7017, pp. 70170W, 2008. https://doi.org/10.1117/12.786935

[87] Chang Liu, *Foundations of MEMS,* Second Edition. England: Pearson Education Limited, 2012.

[88] P. Y. Bruice, *Organic Chemistry*, 2 edition. New Jersey, US, Pearson, 1998.